Semiclassical Transition State Theory for Chemical Reactions



Samuel M. Greene
Magdalen College
University of Oxford

A thesis submitted for the degree of
Master of Science by Research

Trinity Term, 2016

To my family and friends, for their continued support and encouragement

Semiclassical Transition State Theory for Chemical Reactions

Samuel M. Greene, Magdalen College

A thesis submitted in partial fulfillment of the requirements for the degree of Master of Science by Research of the University of Oxford

Trinity Term, 2016

Abstract

First-principles calculations of chemical reaction rate constants have useful applications in a variety of areas. Quantum reactive scattering approaches are the most accurate, but their computational costs scale significantly with system size. Semiclassical Transition State Theory (SCTST) constitutes a more efficient approach. In SCTST, rate constants are calculated from frequencies and anharmonic constants, which depend on the second, third, and fourth derivatives of the reaction's potential energy surface (PES) at the transition state. Further gains in efficiency can be achieved by calculating anharmonic constants for only a subset of degrees of freedom. SCTST can be improved by imposing more realistic behaviour of the reactant and product asymptotes of the potential barrier used in calculations.

This thesis investigates the accuracy of one- and two-dimensional SCTST in relation to accurate quantum scatteirng calculations performed on the same PESs. Calculations are performed for four H atom abstraction and exchange reactions: $H + CH_4$, $H + C_2H_6$, $H + cyc{-}C_3H_6$, and $CH_3 + CH_4$. Two methods are presented for calculating frequencies and anharmonic constants from PESs developed previously for these reactions, which are defined in Jacobi coordinates. 2-D SCTST rate constants exhibit acceptable agreement with results from previous quantum scattering calculations. 1-D SCTST rate constants agree very well with 2-D results, although barrier corrections must be applied in the case of the $CH_3 + CH_4$ reaction. These corrections did not significantly improve the accuracy of other calculations. Agreement between 2-D and 1-D results suggests the validity of reducing the number of degrees of freedom considered in an SCTST calculation.

A practical *ab initio* approach is presented to facilitate evaluation of the accuracy of 1-D SCTST in relation to FD SCTST. Richardson extrapolation is discussed as an approach to improving the accuracy of purely numerical calculations of third and fourth derivatives. FD calculations for the $H + CH_4$ and $H + C_2H_6$ reactions exhibit good agreement with previous results and with results from two different 1-D methods. The second of these methods requires only 4 single-point energy calculations in addition to those required for TST. The agreement of 1-D and FD results suggests the potential applicability of 1-D SCTST to larger systems.

Acknowledgements

Firstly, I thank my supervisor, Professor David Clary, for his mentorship, advice and guidance, and for meeting consistently with me during the course of my degree. This work also would not have been possible without the mentorship of Dr. Xiao Shan, to whom I am grateful for his advice, constructive criticism of my writing, and help with executing *ab initio* calculations. I thank Professor William Miller for useful discussions on Semiclassical Transition State Theory and the WKB approximation and Professor Todd Martinez for useful discussions on numerical differentiation techniques. I am grateful to Yee Ching Kwan for the questions she asked that helped shape and clarify my thinking about my project, and to Dr. Eyad Al-Samra for his companionship in our office. I acknowledge financial support from the Rhodes Trust through a Rhodes Scholarship for graduate study.

Contents

1 Introduction **1**

1.1 Publications 9

2 Semiclassical Transition State Theory (SCTST) **11**

2.1 Introduction 11

2.2 Normal Mode Analysis 12

2.3 Second-Order Vibrational Perturbation Theory 15

2.4 Cumulative Reaction Probability 28

2.5 Thermal Rate Constants 33

2.6 Deep Tunnelling Corrections 33

2.7 The Reduced-Dimensionality Framework 35

3 SCTST Calculations on Analytical Potential Energy Surfaces **39**

3.1 Introduction 39

3.2 Methods 40

3.2.1 Potential Energy Surface Construction 40

3.2.2 Frequency and Anharmonic Constant Calculations 45

3.2.3 Minimum-Energy Path Calculations 48

3.2.4 Barrier Height Calculations 49

3.2.5 Rate Constant Calculations 50

3.3 Results 51

3.3.1 Energetics 51
3.3.2 2-D Rate Constants 54
3.3.2.1 $H + CH_4 \longrightarrow H_2 + CH_3$ (reaction (1.1)) 54
3.3.2.2 $H + C_2H_6 \longrightarrow H_2 + C_2H_5$ (reaction (1.2)) 60
3.3.2.3 $H + cyc-C_3H_6 \longrightarrow H_2 + cyc-C_3H_5$ (reaction (1.3)) 63
3.3.2.4 $CH_3 + CH_4 \longrightarrow CH_4 + CH_3$ (reaction (1.4)) 66
3.3.3 1-D Rate Constants 69
3.3.3.1 $H + CH_4 \longrightarrow H_2 + CH_3$ (reaction (1.1)) 69
3.3.3.2 $H + C_2H_6 \longrightarrow H_2 + C_2H_5$ (reaction (1.2)) 73
3.3.3.3 $H + cyc-C_3H_6 \longrightarrow H_2 + cyc-C_3H_5$ (reaction (1.3)) 75
3.3.3.4 $CH_3 + CH_4 \longrightarrow CH_4 + CH_3$ (reaction (1.4)) 77
3.4 Conclusions 82

4 SCTST Rate Constants from *Ab Initio* Calculations 85
4.1 Introduction 85
4.2 Methods 87
4.2.1 *Ab Initio* Calculations 87
4.2.2 Numerical Differentiation by Richardson Extrapolation 90
4.2.3 Force Constants 93
4.2.4 Coriolis Coupling 96
4.2.5 Density of States 96
4.2.6 Rate Constants 98
4.3 Results 99
4.3.1 Vibrational Frequencies 99
4.3.2 Full-Dimensional SCTST Calculations 102
4.3.2.1 $H + CH_4 \longrightarrow H_2 + CH_3$ (reaction (1.1)) 102
4.3.2.2 $H + C_2H_6 \longrightarrow H_2 + C_2H_5$ (reaction (1.2)) 106

4.3.2.3 Sensitivity to Wang-Landau Parameters 109
4.3.3 One-Dimensional SCTST Calculations 110
4.4 Conclusions 113

5 Conclusions **115**

A Definitions of Abbreviations **119**

References **121**

Chapter 1

Introduction

Molecular reaction dynamics is the study of chemical reactions at a molecular scale [1]. There exist a number of theoretical methods that enable the first-principles calculation of quantities relevant to reaction dynamics and measurable by experiment, such as integral and differential cross-sections and state-specific quantities [2–4]. However, the most important of these are arguably the thermal reaction rate constants and quantities derivable from them (kinetic isotope effects, branching ratios, etc.). Knowledge of reaction rate constants is useful in a variety of areas of contemporary interest, including atmospheric chemistry [5–8], hydrocarbon combustion [9], biological chemistry [10], and materials science [11–13], among others. Accurate theoretical methods that enable the prediction of rate constants without experimental data are of fundamental importance in these areas.

Most methods for calculating rate constants rely upon the Born-Oppenheimer approximation, in which the motion of the electrons in a chemical species is assumed to be separable from the motion of its nuclei [1, 14, 15]. This approximation is often justified, as nuclei are generally significantly more massive than electrons. Electrons therefore respond to changes in nuclear configuration on a significantly shorter time scale than that of nuclear motion. Under this approximation, the wavefunction for a molecule can be expressed as a product of its nuclear and electronic wavefunctions.

Most problems in reaction dynamics can be solved by considering motion of the nuclei in a potential arising from electrostatic interactions between the nuclei and from the configuration of the electrons. This potential can be calculated using electronic structure theory. As a function, it depends only upon the nuclear geometries and is known as the potential energy surface (PES).

There are several approaches to generating a PES for use in dynamics calculations [16–19]. The potential at individual geometries can be calculated as needed by standard *ab initio* electronic structure methods ("direct dynamics"), or a PES can be constructed by fitting an analytical function to *ab initio* energies [17, 20–22]. The expense of constructing a PES for all internal degrees of freedom (DOFs) of a system scales approximately exponentially with the size of the system. This makes it very computationally expensive to construct a complete PES suitable for accurate reaction dynamics calculations on systems of more than four or five atoms [23–27].

The most accurate approaches to calculating rate constants involve performing quantum reactive scattering (QRS) calculations on a complete PES, treating all DOFs of the system explicitly. This involves solving either the time-independent (TI) or time-dependent (TD) nuclear Schrödinger equation. In TD methods, the nuclear wavefunction is initialised as existing only in the region of the PES corresponding to the reactants and then propagated in a particular basis set according to the Hamiltonian [4, 28]. A number of methods for propagating the wavefunction have been developed [29–43]. For example, the Multiconfigurational Time-Dependent Hartree (MCTDH) method has useful applicability to many-dimensional systems [44–48]. It has been applied to the reactions $H + H_2 \longrightarrow H_2 + H$, $H + CH_4 \longrightarrow H_2 + CH_3$, and their isotopologues [27, 49–60].

TI QRS methods involve calculating the S-matrix, which relates the probability amplitudes of eigenstates of the Hamiltonian in the reactant and product regions of

the PES [3]. State-to-state reaction probabilities are calculated from the S-matrix, and rate constants are calculated from the sum of all state-to-state probabilities, the cumulative reaction probability (CRP). TI QRS methods have also been applied to calculate rate constants for a variety of three- and four-atom reactions [2, 4, 61–64].

PES construction often constitutes a major portion of the computational expense of a TD or TI QRS calculation, although the expense associated with solving the nuclear Schrödinger equation ("dynamics calculations") is also significant. Approximate rate constant theories that depend on a smaller region of the PES therefore have useful applications to reactions involving more atoms. Transition State Theory (TST) is among the first of these approximate methods developed [65–69]. This theory introduces the concept of the "activated complex," later renamed the "transition state" (TS), as the geometry of maximum energy along the reaction-path connecting the reactant and product geometries in coordinate space. TST depends only on the PES at the reactant and TS geometries. The key assumptions of this theory are (1) that quantum effects such as tunnelling do not contribute to the reaction rate and (2) that a dividing surface exists in coordinate space at the TS that is not recrossed as molecules follow trajectories from reactants to products [70, 71]. Because TST allows for the calculation of rate constants from a minimal number of electronic structure calculations, it serves as a basis of comparison for more advanced rate constant theories. Such comparisons indicate the extent to which quantum and recrossing effects contribute to the reaction rate.

In recent decades, a number of methods for incorporating these effects into TST in an approximate manner have been developed. These are intermediate in accuracy and efficiency between TST and QRS and use more of the PES than TST but less than QRS. Variational transition state theory with multidimensional tunneling contributions (VTST/MT) is a class of such methods [72–76]. In these approaches, the CRP is

calculated along a one-dimensional path between the reactant and product channels using the WKB approximation [77], and the effects of vibrational motion orthogonal to this path are included. These differ in their applicability to different reactions, depending on the curvature of the reaction-path in mass-weighted coordinates.

The VTST/SCT method (abbreviations defined in Appendix A) is generally most applicable to reactions with small to intermediate reaction-path curvature, as it considers tunnelling only along the zero-point energy turning points of vibrational modes along the concave side of the reaction path in between the reactant and product channels [75, 78]. It therefore depends only on the PES along the reaction-path. In reactions with large reaction-path curvature, tunnelling along straight "corner-cutting" paths between the reactant and product channels contribute more to the reaction rate than tunnelling along the reaction-path [74, 79–83]. The VTST/LCG4 method considers tunnelling along such paths and is often more appropriate for such reactions [84]. It utilizes a larger region of the PES than VTST/SCT. In the VTST/μOMT method, the greater of the VTST/SCT and VTST/LCG4 reaction probabilities at each energy is used to calculate the rate constant. This method can therefore be applied to any reaction without *a priori* knowledge of its reaction-path curvature. The VTST/LAG4 method is the most computationally intensive in terms of dynamics calculations, as it involves calculating the tunnelling path that maximises the tunnelling probability at each energy. These methods have been applied to a variety of reactions [85–97]. VTST/LAG4 generally yields the best agreement to results from QRS, although VTST/μOMT yields results in good agreement with significantly less computational expense.

Other approximate methods include the ring polymer molecular dynamics (RPMD) method, which was adapted for rate constant calculations by Craig and Manolopoulos [98, 99]. This theory relies upon the isomorphism between a classical treatment

of an infinite number of copies of the system coupled via harmonic potentials and a quantum mechanical treatment of a single copy of the system. Their method has yielded results in good agreement with those from benchmark quantum mechanical calculations [85, 86, 89, 100, 101]. Other theories include centroid molecular dynamics and related quantum mechanical improvements to TST [102–106]. Recently, Althorpe and Hele showed that their formulation of quantum TST is identical to RPMD TST if the dividing surface between reactants and products is invariant to imaginary time translation [107, 108]. Instanton methods are semiclassical approximations to these more accurate theories [109–111].

Unlike these other approximate methods, Semiclassical Transition State Theory (SCTST), developed by Miller *et al.* [112–114], depends only on the PES at the reactant and TS geometries. It therefore offers potentially substantial improvements in efficiency through a reduced need for PES calculations. The CRP is calculated semiclassically from an expression for the energy at the TS. In its original form, SCTST was derived from second-order vibrational perturbation theory (VPT2) [115] and therefore depends on the harmonic frequencies and anharmonic constants of the TS [116–119].

SCTST has been applied previously to several reactions with considerable success and agreement with other results [120–124]. Recently, Wagner [125] developed an improved method for calculating the reaction probability in SCTST, in which a one-dimensional barrier is constructed to match the second, third, and fourth derivatives of the potential at the transition state along the reaction path and to match the reaction's forward and reverse barrier heights. The probability of tunnelling through the barrier is calculated using the WKB approximation. This method thereby enables more accurate calculation of tunnelling probabilities, particularly at low energies ("deep tunnelling"), with minimal additional computational expense in dynamics cal-

culations. The only additional PES calculations required for this method are those required for the vibrationally adiabatic reverse barrier height.

SCTST calculations can prove challenging for reactions involving many atoms. Calculating the CRP in SCTST can be computationally expensive for reactions involving more than three or four atoms, as the number of vibrational states of the system scales exponentially with the number of DOFs. Approximate methods for sampling these states (Multidimensional Monte Carlo Integration and the Wang-Landau Algorithm) can potentially be used to address these issues [126]. However, calculating the requisite anharmonic constants requires on the order of F frequency calculations, where F is the number of internal (vibrational) DOFs of the system. This remains the primary obstacle to applying SCTST to larger systems using accurate quantum chemistry calculations.

In this thesis, a reduced-dimensionality (RD) approach to SCTST is presented as a more efficient and simpler approach. RD methods were first developed and applied in the context of QRS calculations in order to improve their efficiency. Explicit quantum dynamics calculations are performed for a subset of the system's internal DOFs, while the remaining DOFs are treated using more approximate methods [4, 24, 63, 127–132]. Several different approaches to choosing which DOFs to treat explicitly have been tested and discussed previously [60, 133–143]. Recent RD QRS calculations have involved treating explicitly only the DOFs corresponding to vibration of the bonds being formed and broken [144–158]. The system of reacting atoms is treated as a three-body system, and the zero-point energies of the "spectator" vibrational modes not treated explicitly are added to the PES. This allows for solution of the Schrödinger equation using the Bending-Corrected Rotating Linear Model, within which the three-body system is assumed to be collinear for the purpose of dynamics calculations [159]. This has allowed for calculations on reactions involving molecules

as large as butane.

In RD SCTST, anharmonic constants are calculated for a reduced number of DOFs, and the remaining DOFs are treated harmonically. This thesis seeks to evaluate the accuracy and efficiency of this approach by applying SCTST to four bimolecular gas-phase chemical reactions:

$$H + CH_4 \longrightarrow H_2 + CH_3 \tag{1.1}$$

$$H + C_2H_6 \longrightarrow H_2 + C_2H_5 \tag{1.2}$$

$$H + \text{cyc-}C_3H_6 \longrightarrow H_2 + \text{cyc-}C_3H_5 \tag{1.3}$$

$$CH_3 + CH_4 \longrightarrow CH_4 + CH_3. \tag{1.4}$$

These prototypical reactions are often used as rigorous tests of rate constant theories [141, 145–147, 150, 154, 158, 160–162]. They involve the abstraction or exchange of a light H atom, so quantum mechanical effects contribute to the rate constants for these reactions, particularly at low temperatures. A comparison with results from TST allows for evaluation of the accuracy with which different methods recover these effects. Reactions (1.1) and (1.3) are the simplest H abstraction reactions involving an alkane and a cyclic alkane, respectively. Reactions (1.1)–(1.3) have significance in combustion processes [9, 145, 158]. All reactions involve cleavage of a strong C–H bond [163]. Reaction (1.4) involves the exchange of a light H atom between two heavier CH_3 species (a "heavy-light-heavy" reaction). It therefore has relatively significant reaction-path curvature, which suggests the importance of corner-cutting effects. As the concave region of the PES in between the reactant and product channels of the PES is not used explicitly in SCTST, this reaction serves as a rigorous test of the ability of SCTST to recover these effects. 2-D PESs have been constructed previously for these reactions, and QRS calculations performed [145, 150, 158]. These

RD QRS results serve as a benchmark to which RD SCTST can be compared, thereby enabling a rigorous evaluation of the applicability of RD SCTST to these systems.

The remainder of this thesis is organised as follows. Chapter 2 presents a derivation of the formulas used to calculate the CRP in SCTST, including a derivation of the expression for the VPT2 energy. A physical interpretation is given of each of the terms in the expression for the CRP, facilitated by the isomorphism among this expression and those for the probabilities of tunnelling through Eckart and Morse potentials within the WKB approximation. An overview of the methods for constructing the potential barrier in the "deep tunneling" framework is also discussed. Finally, the modifications to SCTST required to apply it in an RD framework are discussed.

Chapter 3 discusses the calculation of RD SCTST rate constants for reactions (1.1)–(1.4) from the existing 2-D PESs. These are defined in terms of the Jacobi coordinates of the system. Two methods for calculating the frequencies and anharmonic constants in this coordinate system are discussed. 2-D SCTST results for all reactions are presented and compared to those from the previous 2-D QRS calculations, thereby enabling evaluation of the accuracy of the 2-D SCTST method. 1-D SCTST rate constants are also compared to those from 2-D SCTST, which provides insight into the mechanisms by which SCTST accounts for coupling between the vibrational modes of the system.

Chapter 4 discusses the application of full-dimensional (FD) and 1-D SCTST to reactions (1.1) and (1.2). A practical procedure for calculating anharmonic constants from *ab initio* quantum chemistry calculations is discussed, and Richardson extrapolation is presented as a method for improving the accuracy of the numerical derivatives required in these calculations. Results for both reactions are presented and compared to those from previous studies, and the effect of Richardson extrapolation on the

accuracy of these results is discussed. The computational efficiency of two different 1-D methods relative to the FD method is also evaluated.

1.1 Publications

The following publications are based on the work discussed in this thesis:

Greene, S. M.; Shan, X.; and Clary, D. C. *J. Phys. Chem. A* 119, **2015**, 12015–12027.

Greene, S. M.; Shan, X.; and Clary, D. C. *J. Chem. Phys.* 144, **2016**, 084113.

Greene, S. M.; Shan, X.; and Clary, D. C. *J. Chem. Phys.* in press.

Chapter 2

Semiclassical Transition State Theory (SCTST)

2.1 Introduction

Several key insights led to the development of SCTST as applied in this thesis. First, Miller [167] noted that, in some cases, results from conventional TST exhibit poor agreement with those from QRS calculations even when certain tunnelling corrections are included. He attributed this primarily to the recrossing effects not included in TST, as discussed in Chapter 1. The assumption that trajectories do not recross the dividing surface between reactants and products follows from assuming that motion along the reaction-path is separable from other DOFs in the Hamiltonian at the TS [75]. Exact quantum mechanical calculations indicate that recrossing does not occur at sufficiently low energies, but assuming separability of the Hamiltonian also does not enable the recovery of corner-cutting effects at these energies [167]. Miller therefore derived formulas for an exact quantum mechanical formulation of TST that does not rely upon this separability assumption.

Miller [112] then derived a semiclassical approximation to this formulation of TST using a classical path approximation to the Boltzmann operator $e^{-\beta\hat{H}}$ [168] and the stationary phase approximation [169]. He later [113] used this to derive a semiclassical expression for the cumulative reaction probability (CRP) in terms of the "good"

action variables of the system (i.e., those that are conserved in time), noting that such action variables exist at the TS. Miller *et al.* [114] considered an expression for the energy at the TS in terms of "good" action variables from second-order vibrational perturbation theory (VPT2) applied to a fourth-order Taylor expansion of the potential at the TS [115]. In this analysis, the Hamiltonian is nonseparable. This energy expression was used in the semiclassical framework to calculate the CRP and rate constants for the $D_2CO \longrightarrow D_2 + CO$ reaction. All applications of SCTST to other reactions since have used this VPT2 approach, although other expressions for the energy can, in theory, also be used [170].

In this chapter, a brief overview of normal mode analysis of a molecule to obtain harmonic frequencies is presented. Following from this, the expression for the VPT2 energy in terms of harmonic frequencies and anharmonic constants is derived. This model is applied to a reaction TS, for which one frequency is imaginary, thereby enabling the derivation of formulas for the CRP and rate constants from SCTST. A summary of Wagner's [125] improved method for calculating the CRP is then presented. The chapter concludes with a discussion of the modifications required to apply SCTST within a reduced-dimensionality framework.

2.2 Normal Mode Analysis

Normal mode analysis is often used to simplify problems involving motion of nuclei about a stationary point on a PES. It is based on the assumption that the PES, $V(\mathbf{r})$, about the stationary point can adequately be described by a second-order Taylor expansion, $V^{(2)}(\mathbf{r})$:

$$V^{(2)}(\mathbf{r}) = \frac{1}{2}\sum_{i=1}^{3N}\sum_{j=1}^{3N}\frac{\partial^2 V(\mathbf{r})}{\partial r_i \partial r_j} r_i r_j, \tag{2.1}$$

where N denotes the number of nuclei in the species considered, the coordinates r_i correspond to the individual DOFs of the nuclei in three orthogonal dimensions, and

all partial derivatives are evaluated at the stationary point. Note that no other terms are included in this second-order Taylor series, as the first derivatives of $V(\mathbf{r})$ are 0 at the stationary point, and the zero of energy is considered to be the potential at the stationary point. The expression for the kinetic energy, T, of the nuclei is also considered:

$$T = \frac{1}{2}\sum_{i=1}^{3N} m_i v_i^2, \tag{2.2}$$

where v_i and m_i are the mass and velocity, respectively, associated with motion along the coordinate r_i.

It is useful to analyse the system using Lagrange's equations of motion:

$$\frac{\partial L}{\partial r_k} = \frac{\partial}{\partial t}\frac{\partial L}{\partial v_k}, \tag{2.3}$$

where

$$L = T - V^{(2)}(\mathbf{r}). \tag{2.4}$$

Substituting equations (2.2) and (2.1) into equations (2.3) and (2.4) yields:

$$-\sum_{j=1}^{3N} \frac{\partial^2 V(\mathbf{r})}{\partial r_k \partial r_j} r_j = m_k \frac{\partial v_k}{\partial t}. \tag{2.5}$$

Next, the motion of the nuclei is assumed to be harmonic with some angular frequency ω:

$$r_k(t) = a_1 \sin(\omega t) + a_2 \cos(\omega t), \tag{2.6}$$

where a_1 and a_2 represent arbitrary phase factors. This assumption is justified because the nuclei are considered to move in a harmonic force field. Following from this assumption:

$$\frac{\partial^2 r_k}{\partial t^2} = \frac{\partial v_k}{\partial t} = -\omega^2 r_k. \tag{2.7}$$

Substituting equation (2.7) into equation (2.5) gives:

$$\sum_{j=1}^{3N} \frac{\partial^2 V(\mathbf{r})}{\partial r_k \partial r_j} r_j = m_k \omega^2 r_k. \tag{2.8}$$

It is useful to use mass-weighted coordinates x_i, defined as follows:

$$x_i = m_i^{1/2} r_i. \tag{2.9}$$

Substituting equation (2.9) into equation (2.8) yields:

$$\sum_{j=1}^{3N} m_k^{-1/2} m_j^{-1/2} \frac{\partial^2 V(\mathbf{r})}{\partial r_k \partial r_j} x_j = \omega^2 x_k. \tag{2.10}$$

The normal modes of a species are defined as those in which all nuclei move with the same frequency. Thus, the system of equations for all coordinates x_k constitutes an eigenvalue problem, with eigenvalues equal to the squares of the normal mode frequencies of the system. These eigenvalues can be obtained by diagonalising the mass-weighted Hessian matrix $\mathbf{H}$, where:

$$H_{kj} = m_k^{-1/2} m_j^{-1/2} \frac{\partial^2 V}{\partial r_k \partial r_j}. \tag{2.11}$$

This yields a set of $3N$ eigenvalues. Modern quantum chemistry software packages project the translational and rotational modes out of the mass-weighted hessian before outputting it [171–173]. Diagonalising this post-projection matrix also yields $3N$ eigenvalues, 6 of which (or 5 for a linear molecule) are essentially zero, corresponding to translational and rotational modes. The remaining $F = 3N - 6$ eigenvalues (or $F = 3N - 5$ for a linear molecule) can be used to calculate F frequencies ω_i and F corresponding eigenvectors. Displacements along each of these eigenvectors in normal mode coordinates, with units of (mass$^{1/2}$ length), will be denoted as q_i, such that assigning all q_i the value 0 corresponds to the geometry at the stationary point.

The approximate harmonic force field $V^{(2)}(\mathbf{r})$ considered in this analysis can be expressed as follows:

$$V^{(2)}(\mathbf{r}) = \sum_{i=1}^{F} \frac{1}{2} \frac{\partial^2 V(\mathbf{r})}{\partial q_i^2} q_i^2 = \sum_{i=1}^{F} \frac{1}{2} \omega_i^2 q_i^2. \tag{2.12}$$

By definition, the off-diagonal second derivatives $\frac{\partial^2 V(\mathbf{r})}{\partial q_i \partial q_j}, i \neq j$, are 0. The Hamiltonian $\hat{H}^{(0)}$ or the vibrational (internal) DOFs of this system is therefore:

$$\hat{H}^{(0)} = \sum_{i=1}^{F} \left(\frac{\hbar^2}{2} \frac{\partial^2}{\partial q_i^2} + \frac{1}{2} \omega_i^2 q_i^2 \right). \tag{2.13}$$

Because this Hamiltonian is separable, its eigenfunctions $\psi_{\{n\}}^{(0)}$ are products of one-dimensional harmonic oscillator wavefunctions, $\phi(q_i, n_i)$:

$$\psi_{\{n\}}^{(0)} = \prod_{i=1}^{F} \phi(q_i, n_i), \tag{2.14}$$

where each number n_i in the set $\{n\}$ of quantum states can assume any nonnegative integer value. The one-dimensional harmonic oscillator wavefunctions are given as follows [174]:

$$\phi(q, n) = \frac{1}{(2^n n!)^{1/2}} \left(\frac{\omega}{\hbar \pi} \right)^{1/4} H_n(\omega^{1/2} \hbar^{-1/2} q) \exp\left(\frac{-\omega q^2}{2\hbar} \right), \tag{2.15}$$

where H_n is the n^{th} Hermite polynomial. For a specific configuration $\{n\}$ of quantum states, the energy is:

$$E_{\{n\}}^{(0)} = \sum_{i=1}^{F} \hbar \omega_i (n_i + 1/2). \tag{2.16}$$

2.3 Second-Order Vibrational Perturbation Theory

One can improve this analysis by including higher-order terms in the Taylor expansion for $V(\mathbf{r})$. For convenience, the Taylor expansion is expressed in normal mode coordinates in the following analysis, in which third- and fourth-order terms will be considered. Because the contribution of these terms to the system's energy is often significantly less than the harmonic terms, these terms are considered a perturbation $\hat{H}^{(1)}$ to the zeroth-order Hamiltonian $\hat{H}^{(0)}$ [115, 120]:

$$\hat{H}^{(1)} = \frac{1}{3!} \sum_{i=1}^{F} \sum_{j=1}^{F} \sum_{k=1}^{F} f_{ijk} q_i q_j q_k + \frac{1}{4!} \sum_{i=1}^{F} \sum_{j=1}^{F} \sum_{k=1}^{F} \sum_{l=1}^{F} f_{ijkl} q_i q_j q_k q_l, \tag{2.17}$$

where, following the notation of Miller *et al.* [114]:

$$f_{ijk} = \frac{\partial^3 V(\mathbf{r})}{\partial q_i \partial q_j \partial q_k} \tag{2.18}$$

and

$$f_{ijkl} = \frac{\partial^4 V(\mathbf{r})}{\partial q_i \partial q_j \partial q_k \partial q_l}. \tag{2.19}$$

As above, these derivatives are evaluated at the stationary point of the PES.

In second-order nondegenerate perturbation theory, the system's energy is expressed as a sum of zeroth-, first-, and second-order terms [77, 174]:

$$E_{\{n\}} = E^{(0)}_{\{n\}} + E^{(1)}_{\{n\}} + E^{(2)}_{\{n\}}, \tag{2.20}$$

where

$$E^{(1)}_{\{n\}} = \left\langle \psi^{(0)}_{\{n\}} \middle| \hat{H}^{(1)} \middle| \psi^{(0)}_{\{n\}} \right\rangle \tag{2.21}$$

and

$$E^{(2)}_{\{n\}} = \sum_{\{m\}\neq\{n\}} \frac{\left| \left\langle \psi^{(0)}_{\{m\}} \middle| \hat{H}^{(1)} \middle| \psi^{(0)}_{\{n\}} \right\rangle \right|^2}{E^{(0)}_{\{n\}} - E^{(0)}_{\{m\}}}, \tag{2.22}$$

where the sum in equation (2.22) is over all possible sets of quantum numbers not equal to $\{n\}$. Typically, the energy in VPT2 is expressed as follows [114, 115, 120]:

$$E_{\{n\}} = \sum_{i=1}^{F} \hbar\omega_i (n_i + 1/2) + \sum_{i=1}^{F} \sum_{k=i}^{F} x_{ik} (n_i + 1/2)(n_k + 1/2) + G_0, \tag{2.23}$$

where the x_{ik} terms are referred to as anharmonic constants. Anharmonic constants for which $i = k$ and $i \neq k$ are referred to as diagonal and off-diagonal, respectively. It now remains to derive expressions for the anharmonic constants and G_0 from equations (2.21) and (2.22).

The integrals required to derive these expressions can be simplified by noting the following relations involving the wavefunctions of a one-dimensional harmonic oscillator, which arise from the recursion formula for Hermite polynomials [174]:

$$q\phi(q,n) = \frac{\hbar^{1/2}}{\omega^{1/2}} \left(\frac{n^{1/2}}{2^{1/2}} \phi(q, n-1) + \frac{(n+1)^{1/2}}{2^{1/2}} \phi(q, n+1) \right) \tag{2.24}$$

$$q^2\phi(q,n) = \frac{\hbar}{\omega}\left(\frac{[n(n-1)]^{1/2}}{2}\phi(q,n-2) + (n+1/2)\phi(q,n) + \frac{[(n+2)(n+1)]^{1/2}}{2}\phi(q,n+2)\right) \quad (2.25)$$

$$q^3\phi(q,n) = \frac{\hbar^{3/2}}{\omega^{3/2}}\left(\frac{[n(n-1)(n-2)]^{1/2}}{2^{3/2}}\phi(q,n-3) + \frac{3n^{3/2}}{2^{3/2}}\phi(q,n-1) + \frac{3(n+1)^{3/2}}{2^{3/2}}\phi(q,n+1) + \frac{[(n+3)(n+2)(n+1)]^{1/2}}{2^{3/2}}\phi(q,n+3)\right) \quad (2.26)$$

$$q^4\phi(q,n) = \frac{\hbar^2}{\omega^2}\left(\frac{[n(n-1)(n-2)(n-3)]^{1/2}}{4}\phi(q,n-4) + \frac{n^{1/2}(2n-1)(n-1)^{1/2}}{2}\phi(q,n-2) + \frac{3(2n^2+2n+1)}{4}\phi(q,n) + \frac{(2n+3)[(n+2)(n+1)]^{1/2}}{2}\phi(q,n+2) + \frac{[(n+4)(n+3)(n+2)(n+1)]^{1/2}}{4}\phi(q,n+4)\right). \quad (2.27)$$

The first-order correction to the energy, $E^{(1)}_{\{n\}}$, will be considered first. Because $\hat{H}^{(1)}$ is a sum (equation (2.17)), the integral in equation (2.21) can be separated into a sum of integrals, one for each term in $\hat{H}^{(1)}$. Multiplying the function $\phi(q_i,n)$ by only even powers of q_i yields expressions involving the function $\phi(q_i,n)$ if the relations in equations (2.24)–(2.27) are applied to simplify the result. Due to the orthogonality of the one-dimensional harmonic oscillator wavefunctions, it follows that only integrals with fourth-order terms involving only even powers of q_i contribute to $E^{(1)}_{\{n\}}$. Thus, the integral can be simplified as follows:

$$\left\langle \psi^{(0)}\middle|\frac{1}{4!}\hat{H}^{(1)}\middle|\psi^{(0)}\right\rangle = \sum_{i=1}^{F}\left\langle \phi(q_i,n_i)\middle|\frac{1}{4!}f_{iiii}q_i^4\middle|\phi(q_i,n_i)\right\rangle + \sum_{i<k}\left\langle \phi(q_i,n_i)\phi(q_k,n_k)\middle|\frac{6}{4!}f_{iikk}q_i^2q_k^2\middle|\phi(q_i,n_i)\phi(q_k,n_k)\right\rangle. \quad (2.28)$$

The factor of 6 in the second term above arises from the fact that, for each particular choice of i and k such that $i < k$, there are 6 equivalent terms in $\hat{H}^{(1)}$: $f_{iikk}q_i^2q_k^2$,

$f_{kkii}q_i^2q_k^2$, $f_{ikik}q_i^2q_k^2$, $f_{kiki}q_i^2q_k^2$, $f_{ikki}q_i^2q_k^2$, and $f_{kiik}q_i^2q_k^2$. Evaluating the above integrals using equations (2.25) and (2.27) and simplifying gives:

$$\begin{aligned}\left\langle \psi^{(0)} \middle| \frac{1}{4!}\hat{H}^{(1)} \middle| \psi^{(0)} \right\rangle &= \sum_{i=1}^{F} \frac{1}{24} f_{iiii} \frac{\hbar^2}{\omega_i^2} \frac{3}{4} 2(n_i^2 + n_i + 1/4 + 1/4) \\ &\quad + \sum_{i<k} \frac{6}{24} f_{iikk} \frac{\hbar^2}{\omega_i \omega_k} (n_i + 1/2)(n_k + 1/2) \\ &= \sum_{i=1}^{F} \frac{\hbar^2}{16\omega_i^2} f_{iiii}(n_i + 1/2)^2 + \sum_{i<k} \frac{\hbar^2}{4\omega_i\omega_k} f_{iikk}(n_i + 1/2)(n_k + 1/2) \\ &\quad + \sum_{i=1}^{F} \frac{\hbar^2}{64} \frac{f_{iiii}}{\omega_i^2}. \end{aligned} \tag{2.29}$$

Comparing this expression to equation (2.23) suggests that these terms contribute as follows to the diagonal anharmonic constants:

$$x_{ii} = \frac{\hbar^2}{16\omega_i^2} f_{iiii} + ..., \tag{2.30}$$

and as follows to the off-diagonal anharmonic constants:

$$x_{ik} = \frac{\hbar^2}{4\omega_i\omega_k} f_{iikk} + ..., i < k, \tag{2.31}$$

and as follows to G_0:

$$G_0 = \frac{\hbar^2}{64} \sum_{i=1}^{F} \frac{f_{iiii}}{\omega_i^2} + ... \tag{2.32}$$

The ellipses in the above expressions indicate that further terms will be added to these expressions in later analysis.

It remains to evaluate the second-order corrections to the energy from $E^{(2)}_{\{n\}}$. This is done by identifying the wavefunctions $\psi^{(0)}_{\{m\}}$ with nonzero contributions to the sum in equation (2.22). First considering terms in which the i^{th} quantum number in $\{m\}$, m_i, is three less than the i^{th} quantum number in $\{n\}$, n_i, yields:

$$\begin{aligned}\left\langle \psi^{(0)}_{\{m\}} \middle| \hat{H}^{(1)} \middle| \psi^{(0)}_{\{n\}} \right\rangle \Big|_{m_i = n_i - 3} &= \left\langle \psi^{(0)}_{\{m\}} \middle| \frac{1}{6} f_{iii} q_i^3 \middle| \psi^{(0)}_{\{n\}} \right\rangle \Big|_{m_i = n_i - 3} \\ &= \frac{\hbar^{3/2}}{\omega_i^{3/2}} \frac{f_{iii}}{6} \frac{[(n_i(n_i-1)(n_i-2)]^{1/2}}{2^{3/2}}. \end{aligned} \tag{2.33}$$

There are F such terms, and their contribution to $E^{(2)}_{\{n\}}$ is:

$$\sum_{i=1}^{F}\left(\frac{\hbar^{3/2}}{\omega_i^{3/2}}\frac{f_{iii}}{6}\frac{[(n_i(n_i-1)(n_i-2)]^{1/2}}{2^{3/2}}\right)^2\frac{1}{3\hbar\omega_i}. \tag{2.34}$$

No other terms contribute because there are no other powers of q_i that couple the wavefunction $\phi(q_i, n_i)$ to $\phi(q_i, n_i-3)$. Similarly, there are F terms from wavefunctions in which $m_i = n_i + 3$:

$$\sum_{i=1}^{F}\left.\frac{\left|\left\langle\psi^{(0)}_{\{m\}}\middle|\hat{H}^{(1)}\middle|\psi^{(0)}_{\{n\}}\right\rangle\right|^2}{E^{(0)}_{\{n\}}-E^{(0)}_{\{m\}}}\right|_{m_i=n_i+3} = \sum_{i=1}^{F}\frac{1}{-3\omega_i}\left(\frac{\hbar^{3/2}}{\omega_i^{3/2}}\frac{f_{iii}}{6}\frac{(n_i+3)!^{1/2}}{2^{3/2}n_i!^{1/2}}\right)^2. \tag{2.35}$$

These expressions will be further simplified. First, wavefunctions $\psi^{(0)}_{\{m\}}$ for which $m_i = n_i - 1$ are considered:

$$\left\langle\psi^{(0)}_{\{m\}}\middle|\hat{H}^{(1)}\middle|\psi^{(0)}_{\{n\}}\right\rangle\Big|_{m_i=n_i-1} = \frac{f_{iii}}{2}\frac{\hbar^{3/2}}{\omega_i^{3/2}}\frac{n_i^{3/2}}{2^{3/2}} + \sum_{j\neq i}\frac{3f_{ijj}}{6}\frac{\hbar^{3/2}}{\omega_j\omega_i^{1/2}}(n_j+1/2)\frac{n_i^{1/2}}{2^{1/2}}. \tag{2.36}$$

The factor of 3 before f_{ijj} arises from the fact that there are 3 equivalent terms in $\hat{H}^{(1)}$ for a particular choice of $j \neq i$: $f_{ijj}q_j^2q_i$, $f_{jij}q_j^2q_i$, and $f_{jji}q_j^2q_i$. Note that for each choice of the index i, the sum above is only over one index, j. For clarity in the following analysis, the first term on the right side of equation (2.36) is defined as A_i, and the second term as B_{ij}, such that:

$$\left\langle\psi^{(0)}_{\{m\}}\middle|\hat{H}^{(1)}\middle|\psi^{(0)}_{\{n\}}\right\rangle\Big|_{m_i=n_i-1} = A_i + \sum_{j\neq i}B_{ij}. \tag{2.37}$$

The square modulus of this expression is:

$$\left|\left\langle\psi^{(0)}_{\{m\}}\middle|\hat{H}^{(1)}\middle|\psi^{(0)}_{\{n\}}\right\rangle\Big|_{m_i=n_i-1}\right|^2 = A_i^2 + \sum_{j\neq i}B_{ij}^2 + 2A_i\sum_{j\neq i}B_{ij} + \sum_{j\neq i}\sum_{k\neq j}B_{ij}B_{ik}. \tag{2.38}$$

Here the sum in the fourth term is over two indices, j and k. There are F possible wavefunctions $\psi_{\{m\}}$ for which $m_i = n_i - 1$, so there are F expressions of the above form that contribute to $E^{(2)}_{\{n\}}$. Considering their sum and rearranging indices gives:

$$\sum_{i=1}^{F}\frac{A_i^2}{\hbar\omega_i} + \sum_{i\neq k}\frac{1}{\hbar\omega_i}B_{ik}^2 + \sum_{i\neq k}\frac{2A_iB_{ik}}{\hbar\omega_i} + \sum_{i\neq j\neq k}\frac{B_{ij}B_{ik}}{\hbar\omega_i}. \tag{2.39}$$

The sums in the second and third terms are over two indices, i and k, and the sum in the fourth term is over three indices, i, j, and k. Each of the 4 terms in the above expression will be considered separately below.

It is useful to first consider wavefunctions $\psi^{(0)}_{\{m\}}$ for which $m_i = n_i + 1$:

$$\left\langle \psi^{(0)}_{\{m\}} \middle| \hat{H}^{(1)} \middle| \psi^{(0)}_{\{n\}} \right\rangle \Big|_{m_i=n_i+1} = \frac{f_{iii}}{2} \frac{\hbar^{3/2}}{\omega_i^{3/2}} \frac{(n_i+1)^{3/2}}{2^{3/2}} + \sum_{j\neq i} \frac{3f_{ijj}}{6} \frac{\hbar^{3/2}}{\omega_j \omega_i^{1/2}} (n_j + 1/2) \frac{(n_i+1)^{1/2}}{2^{1/2}}. \quad (2.40)$$

Proceeding as above suggests definitions of terms C_i and D_{ij}:

$$\left\langle \psi^{(0)}_{\{m\}} \middle| \hat{H}^{(1)} \middle| \psi^{(0)}_{\{n\}} \right\rangle \Big|_{m_i=n_i+1} = C_i + \sum_{j\neq i} D_{ij}. \quad (2.41)$$

The contribution of these terms to the energy is as follows:

$$-\sum_{i=1}^{F} \frac{C_i^2}{\hbar\omega_i} - \sum_{i\neq k} \frac{D_{ik}^2}{\hbar\omega_i} - \sum_{i\neq k} \frac{2C_i D_{ik}}{\hbar\omega_i} - \sum_{i\neq j\neq k} \frac{D_{ij} D_{ik}}{\hbar\omega_i}. \quad (2.42)$$

Each of these 4 terms will also be considered separately in the following discussion.

As equations (2.34) and (2.35), and the first terms in equations (2.39) and (2.42), only involve sums over one index, they constitute part of the expression for the diagonal anharmonic constants. Taking their sum and simplifying gives:

$$\sum_{i=1}^{F} -\frac{\hbar^2}{16\omega_i^2} \frac{f_{iii}^2}{\omega_i^2} \frac{5}{3} (n_i + 1/2)^2 - \sum_{i=1}^{F} \frac{7\hbar^2}{576} \frac{f_{iii}^2}{\omega_i^4}. \quad (2.43)$$

Thus the expression for x_{ii} becomes:

$$x_{ii} = \frac{\hbar^2}{16\omega_i^2} \left[f_{iiii} - \frac{f_{iii}^2}{\omega_i^2} \left(\frac{8\omega_i^2 - 3\omega_i^2}{4\omega_i^2 - \omega_i^2} \right) + ... \right]. \quad (2.44)$$

The second term in the expression for x_{ii} was rewritten to simplify later analysis. The expression for G_0 becomes:

$$G_0 = \frac{\hbar^2}{64} \sum_{i=1}^{F} \frac{f_{iiii}}{\omega_i^2} - \frac{7\hbar^2}{576} \sum_{i=1}^{F} \frac{f_{iii}^2}{\omega_i^4} + ... \quad (2.45)$$

The sum of the fourth terms in equations (2.39) and (2.42) is:

$$\sum_{i\neq k} -\frac{\hbar^2}{4\omega_i\omega_k}\sum_{j\neq k}\frac{f_{iij}f_{jkk}}{2\omega_j^2}(n_i+1/2)(n_k+1/2)$$
$$=\sum_{i<k} -\frac{\hbar^2}{4\omega_i\omega_k}\sum_{j\neq k}\frac{f_{iij}f_{jkk}}{\omega_j^2}(n_i+1/2)(n_k+1/2), \quad (2.46)$$

suggesting the following addition to the expression for the off-diagonal anharmonic constants:

$$x_{ik}=\frac{\hbar^2}{4\omega_i\omega_k}\left(f_{iikk}-\sum_{j\neq k}\frac{f_{iij}f_{jkk}}{\omega_j^2}+...\right), i<k \quad (2.47)$$

Next, integrals will be considered that involve wavefunctions $\psi^{(0)}_{\{m\}}$ in which two quantum numbers differ from those in $\psi^{(0)}_{\{n\}}$: $m_i = n_i \pm 2$ and $m_k = n_k \pm 1$. The values of the contributions to $E^{(2)}_{\{n\}}$ from each of these four integrals are presented below:

$$\left.\frac{\left|\left\langle\psi^{(0)}_{\{m\}}\middle|\hat{H}^{(1)}\middle|\psi^{(0)}_{\{n\}}\right\rangle\right|^2}{E^{(0)}_{\{n\}}-E^{(0)}_{\{m\}}}\right|^{m_k=n_k-1}_{m_i=n_i-2}=\left(\frac{3f_{iik}}{6}\frac{\hbar^{3/2}}{\omega_i\omega_k^{1/2}}\frac{[n_i(n_i-1)]^{1/2}}{2}\frac{n_k^{1/2}}{2^{1/2}}\right)^2\frac{1}{2\hbar\omega_i+\hbar\omega_k} \quad (2.48)$$

$$\left.\frac{\left|\left\langle\psi^{(0)}_{\{m\}}\middle|\hat{H}^{(1)}\middle|\psi^{(0)}_{\{n\}}\right\rangle\right|^2}{E^{(0)}_{\{n\}}-E^{(0)}_{\{m\}}}\right|^{m_k=n_k+1}_{m_i=n_i-2}=$$
$$\left(\frac{3f_{iik}}{6}\frac{\hbar^{3/2}}{\omega_i\omega_k^{1/2}}\frac{[n_i(n_i-1)]^{1/2}}{2}\frac{(n_k+1)^{1/2}}{2^{1/2}}\right)^2\frac{1}{2\hbar\omega_i-\hbar\omega_k} \quad (2.49)$$

$$\left.\frac{\left|\left\langle\psi^{(0)}_{\{m\}}\middle|\hat{H}^{(1)}\middle|\psi^{(0)}_{\{n\}}\right\rangle\right|^2}{E^{(0)}_{\{n\}}-E^{(0)}_{\{m\}}}\right|^{m_k=n_k-1}_{m_i=n_i+2}=$$
$$\left(\frac{3f_{iik}}{6}\frac{\hbar^{3/2}}{\omega_i\omega_k^{1/2}}\frac{[(n_i+2)(n_i+1)]^{1/2}}{2}\frac{n_k^{1/2}}{2^{1/2}}\right)^2\frac{1}{-2\hbar\omega_i+\hbar\omega_k} \quad (2.50)$$

$$\left.\frac{\left|\left\langle\psi^{(0)}_{\{m\}}\middle|\hat{H}^{(1)}\middle|\psi^{(0)}_{\{n\}}\right\rangle\right|^2}{E^{(0)}_{\{n\}}-E^{(0)}_{\{m\}}}\right|^{m_k=n_k+1}_{m_i=n_i+2}=$$
$$\left(\frac{3f_{iik}}{6}\frac{\hbar^{3/2}}{\omega_i\omega_k^{1/2}}\frac{[(n_i+2)(n_i+1)]^{1/2}}{2}\frac{(n_k+1)^{1/2}}{2^{1/2}}\right)^2\frac{1}{-2\hbar\omega_i-\hbar\omega_k}. \quad (2.51)$$

There are $F(F-1)$ of each of these terms because $i \neq k$. The sum of all terms from equations (2.48) to (2.51) and the second terms from equations (2.39) and (2.42) is:

$$\sum_{i\neq k} \frac{\hbar^2 f_{iik}^2}{64\omega_i^2\omega_k^2(4\omega_i^2-\omega_k^2)} \left[-32\omega_i^2(n_i+1/2)^2 - 32\omega_i\omega_k(n_i+1/2)(n_k+1/2) \right. \\ \left. +12\omega_k^2(n_i+1/2)^2 + 3\omega_k^2\right]. \quad (2.52)$$

Considering only the terms that include a factor of $(n_i+1/2)^2$ gives the following:

$$\sum_{i\neq k} \frac{\hbar^2}{16\omega_i^2} \frac{-f_{iik}^2}{\omega_k^2} \left(\frac{8\omega_i^2-3\omega_k^2}{4\omega_i^2-\omega_k^2}\right)(n_i+1/2)^2. \quad (2.53)$$

This term is therefore added to the expression for the diagonal anharmonic constants:

$$x_{ii} = \frac{\hbar^2}{16\omega_i^2}\left[f_{iiii} - \sum_{k=1}^{F} \frac{f_{iik}^2}{\omega_k^2}\left(\frac{8\omega_i^2-3\omega_k^2}{4\omega_i^2-\omega_k^2}\right)\right]. \quad (2.54)$$

Now simplifying the term in equation (2.52) that includes a factor of $(n_i+1/2)(n_k+1/2)$ gives the following:

$$\frac{\hbar^2 f_{iik}^2}{2\omega_i\omega_k}\left(\frac{1}{4\omega_i^2-\omega_k^2}\right)(n_i+1/2)(n_k+1/2). \quad (2.55)$$

It will later be useful to rewrite this expression as follows:

$$\frac{\hbar^2}{4\omega_i\omega_k}\frac{2f_{iik}^2(\omega_i^2+\omega_k^2-\omega_i^2)}{[(\omega_i+\omega_k)^2-\omega_i^2][(\omega_i-\omega_k)^2-\omega_i^2]}(n_i+1/2)(n_k+1/2). \quad (2.56)$$

This term therefore constitutes an additional part of the expression for x_{ik}:

$$x_{ik} = \frac{\hbar^2}{4\omega_i\omega_k}\left(f_{iikk} - \sum_{j\neq k}\frac{f_{iij}f_{jkk}}{\omega_j^2} + \frac{2f_{iik}^2(\omega_i^2+\omega_k^2-\omega_i^2)}{[(\omega_i+\omega_k)^2-\omega_i^2][(\omega_i-\omega_k)^2-\omega_i^2]} + ...\right), i<k. \quad (2.57)$$

An additional term in which i and k are interchanged must be added to the expression for x_{ik} because, in the analysis above, it was only assumed that $i \neq k$, whereas the expression for x_{ik} specifies that $i < k$:

$$x_{ik} = \frac{\hbar^2}{4\omega_i\omega_k}\left(f_{iikk} - \sum_{j\neq k}\frac{f_{iij}f_{jkk}}{\omega_j^2} + \frac{2f_{iik}^2(\omega_i^2+\omega_k^2-\omega_i^2)}{[(\omega_i+\omega_k)^2-\omega_i^2][(\omega_i-\omega_k)^2-\omega_i^2]}\right.$$

$$+\frac{2f_{ikk}^2(\omega_i^2+\omega_k^2-\omega_k^2)}{[(\omega_i+\omega_k)^2-\omega_k^2][(\omega_i-\omega_k)^2-\omega_k^2]}+...\Bigg), i<k. \quad (2.58)$$

The condition on the sum in the second term of x_{ik} can be rewritten as $j \neq i$ because of the symmetry of the expression. This gives:

$$x_{ik}=\frac{\hbar^2}{4\omega_i\omega_k}\Bigg(f_{iikk}-\sum_{j\neq i}\frac{f_{iij}f_{jkk}}{\omega_j^2}+\frac{2f_{iik}^2(\omega_i^2+\omega_k^2-\omega_i^2)}{[(\omega_i+\omega_k)^2-\omega_i^2][(\omega_i-\omega_k)^2-\omega_i^2]}$$
$$+\frac{2f_{ikk}^2(\omega_i^2+\omega_k^2-\omega_k^2)}{[(\omega_i+\omega_k)^2-\omega_k^2][(\omega_i-\omega_k)^2-\omega_k^2]}+...\Bigg), i<k. \quad (2.59)$$

The remaining term in equation (2.52) is added to the expression for G_0, as it does not depend on any quantum numbers:

$$G_0=\frac{\hbar^2}{64}\sum_{i=1}^{F}\frac{f_{iiii}}{\omega_i^2}-\frac{7\hbar^2}{576}\sum_{i=1}^{F}\frac{f_{iii}^2}{\omega_i^4}+\frac{3\hbar^2}{64}\sum_{i\neq k}\frac{f_{iik}^2}{(4\omega_i^2-\omega_k^2)\omega_i^2}+... \quad (2.60)$$

The sum of the third terms in equations (2.34) and (2.35) is:

$$\sum_{i\neq k}-\frac{1}{4\omega_i\omega_k}\frac{f_{iii}f_{ikk}}{\omega_i^2}(n_i+1/2)(n_k+1/2), \quad (2.61)$$

suggesting that this term can be added to the expression for the off-diagonal anharmonic constants:

$$x_{ik}=\frac{\hbar^2}{4\omega_i\omega_k}\Bigg(f_{iikk}-\sum_{j=1}^{F}\frac{f_{iij}f_{jkk}}{\omega_j^2}+\frac{2f_{iik}^2(\omega_i^2+\omega_k^2-\omega_i^2)}{[(\omega_i+\omega_k)^2-\omega_i^2][(\omega_i-\omega_k)^2-\omega_i^2]}$$
$$+\frac{2f_{ikk}^2(\omega_i^2+\omega_k^2-\omega_k^2)}{[(\omega_i+\omega_k)^2-\omega_k^2][(\omega_i-\omega_k)^2-\omega_k^2]}+...\Bigg), i<k, \quad (2.62)$$

as it is the term for the case in the sum in which $j=i$.

Lastly, we consider integrals involving wavefunctions $\psi_{\{m\}}^{(0)}$ in which three unique quantum numbers differ from their counterparts in $\psi_{\{n\}}^{(0)}$: $m_i=n_i\pm1$, $m_j=n_i\pm1$, and $m_k=n_k\pm1$, for $i\neq j\neq k$. There are 8 such terms; their total contribution to $E_{\{n\}}^{(2)}$ is presented here:

$$\frac{1}{6}\sum_{i\neq j\neq k}\Bigg[\left(\frac{\hbar^{3/2}f_{ijk}}{\omega_i^{1/2}\omega_j^{1/2}\omega_k^{1/2}}\frac{n_i^{1/2}n_j^{1/2}n_k^{1/2}}{8^{1/2}}\right)^2\frac{1}{\hbar\omega_i+\hbar\omega_j+\hbar\omega_k}+$$

$$\left(\frac{\hbar^{3/2}f_{ijk}}{\omega_i^{1/2}\omega_j^{1/2}\omega_k^{1/2}}\frac{n_i^{1/2}n_j^{1/2}(n_k+1)^{1/2}}{8^{1/2}}\right)^2\frac{1}{\hbar\omega_i+\hbar\omega_j-\hbar\omega_k}+$$
$$\left(\frac{\hbar^{3/2}f_{ijk}}{\omega_i^{1/2}\omega_j^{1/2}\omega_k^{1/2}}\frac{n_i^{1/2}(n_j+1)^{1/2}n_k^{1/2}}{8^{1/2}}\right)^2\frac{1}{\hbar\omega_i-\hbar\omega_j+\hbar\omega_k}+$$
$$\left(\frac{\hbar^{3/2}f_{ijk}}{\omega_i^{1/2}\omega_j^{1/2}\omega_k^{1/2}}\frac{n_i^{1/2}(n_j+1)^{1/2}(n_k+1)^{1/2}}{8^{1/2}}\right)^2\frac{1}{\hbar\omega_i-\hbar\omega_j-\hbar\omega_k}+$$
$$\left(\frac{\hbar^{3/2}f_{ijk}}{\omega_i^{1/2}\omega_j^{1/2}\omega_k^{1/2}}\frac{(n_i+1)^{1/2}n_j^{1/2}n_k^{1/2}}{8^{1/2}}\right)^2\frac{1}{-\hbar\omega_i+\hbar\omega_j+\hbar\omega_k}+$$
$$\left(\frac{\hbar^{3/2}f_{ijk}}{\omega_i^{1/2}\omega_j^{1/2}\omega_k^{1/2}}\frac{(n_i+1)^{1/2}n_j^{1/2}(n_k+1)^{1/2}}{8^{1/2}}\right)^2\frac{1}{-\hbar\omega_i+\hbar\omega_j-\hbar\omega_k}+$$
$$\left(\frac{\hbar^{3/2}f_{ijk}}{\omega_i^{1/2}\omega_j^{1/2}\omega_k^{1/2}}\frac{(n_i+1)^{1/2}(n_j+1)^{1/2}n_k^{1/2}}{8^{1/2}}\right)^2\frac{1}{-\hbar\omega_i-\hbar\omega_j+\hbar\omega_k}+$$
$$\left(\frac{\hbar^{3/2}f_{ijk}}{\omega_i^{1/2}\omega_j^{1/2}\omega_k^{1/2}}\frac{(n_i+1)^{1/2}(n_j+1)^{1/2}(n_k+1)^{1/2}}{8^{1/2}}\right)^2\frac{1}{-\hbar\omega_i-\hbar\omega_j-\hbar\omega_k}\Bigg]. \quad (2.63)$$

Note that any permutation of the indices i, j, and k in any of the terms does not change the value of the above expression because it is summed over all three of these indices. This facilitates elimination of terms involving n_j and simplification to the following expression:

$$\sum_{i\neq j\neq k}\Bigg[\frac{\hbar^2}{4\omega_i\omega_j}\left(\frac{f_{ijk}^2(\omega_i^2+\omega_k^2-\omega_j^2)}{[(\omega_i+\omega_k)^2-\omega_j^2][(\omega_i-\omega_k)^2-\omega_j^2]}\right)(n_i+1/2)(n_k+1/2)$$
$$-\frac{\hbar^2}{24}\frac{f_{ijk}^2}{[(\omega_i+\omega_k)^2-\omega_j^2][(\omega_i-\omega_k)^2-\omega_j^2]}\Bigg]. \quad (2.64)$$

In this form, these terms can now be added to the expressions for the off-diagonal anharmonic constants and G_0:

$$x_{ik}=\frac{\hbar^2}{4\omega_i\omega_k}\left(f_{iikk}-\sum_{j=1}^{F}\frac{f_{iij}f_{jkk}}{\omega_j^2}+\sum_{j=1}^{F}\frac{2f_{ijk}^2(\omega_i^2+\omega_k^2-\omega_j^2)}{[(\omega_i+\omega_k)^2-\omega_j^2][(\omega_i-\omega_k)^2-\omega_j^2]}\right), i<k \quad (2.65)$$

$$G_0=\frac{\hbar^2}{64}\sum_{i=1}^{F}\frac{f_{iiii}}{\omega_i^2}-\frac{7\hbar^2}{576}\sum_{i=1}^{F}\frac{f_{iii}^2}{\omega_i^4}+\frac{3\hbar^2}{64}\sum_{i\neq k}\frac{f_{iik}^2}{(4\omega_i^2-\omega_k^2)\omega_i^2}$$

$$-\frac{\hbar^2}{4}\sum_{i<j<k}\frac{f_{ijk}^2}{[(\omega_i+\omega_k)^2-\omega_j^2][(\omega_i-\omega_k)^2-\omega_j^2]}. \quad (2.66)$$

Other fourth derivatives in $\hat{H}^{(1)}$ do not contribute significantly to the second-order energy $E_{\{n\}}^{(2)}$ because the energy term in the denominator $E_{\{n\}}^{(0)}-E_{\{m\}}^{(0)}$ associated with integrals involving these terms is significantly greater than for other terms. These terms are therefore neglected. The remaining expressions for the VPT2 energy, $E_{\{n\}}$ are repeated below, for convenience.

$$E_{\{n\}}=\sum_{i=1}^{F}\hbar\omega_i(n_i+1/2)+\sum_{i=1}^{F}\sum_{k=i}^{F}x_{ik}(n_i+1/2)(n_k+1/2)+G_0, \quad (2.67)$$

$$x_{ii}=\frac{\hbar^2}{16\omega_i^2}\left[f_{iiii}-\sum_{k=1}^{F}\frac{f_{iik}^2}{\omega_k^2}\left(\frac{8\omega_i^2-3\omega_k^2}{4\omega_i^2-\omega_k^2}\right)\right]. \quad (2.68)$$

These expressions for the anharmonic constants differ from those given in previous studies in that they do not include rovibrational terms [114, 120]. In neglecting these terms from the above analysis, vibrational motion is assumed to be separable from rotational motion. This assumption is justified at moderate temperatures and has therefore been employed previously in SCTST calculations on systems of comparable size to those considered in this study [122, 123].

It was also assumed that all unperturbed states considered in the analysis above are nondegenerate. If there are states at the same zeroth-order energy as the zeroth-order state $\Psi_{\{n\}}^{(0)}$, and if those states are coupled to $\Psi_{\{n\}}^{(0)}$ via the perturbation $H^{(1)}$, degenerate perturbation theory must be applied in a strictly rigorous treatment of the system [77].

If, for example, the frequencies ω_i and ω_j are equal, then the states $\Psi_{\{m\}}$ for which $m_i=n_i\pm 2$ and $m_j=n_j\mp 2$ are degenerate with the zeroth-order state $\Psi_{\{n\}}$ and coupled to it via the $f_{iijj}q_i^2q_j^2$ term in the perturbation. Treating these effects in degenerate perturbation theory involves diagonalising the coupling matrix $\mathbf{W}$, defined

as follows [77]:

$$W_{ij} = \left\langle \Psi_i^0 \middle| \hat{H}^{(1)} \middle| \Psi_j^0 \right\rangle, \tag{2.69}$$

where Ψ_i^0 and Ψ_j^0 denote unperturbed degenerate states. Expressions for the VPT2 energy and anharmonic constants have been derived previously for species with degenerate vibrational frequencies (i.e., spherical top and symmetric top molecules) using degenerate perturbation theory [120, 175, 176]. However, it is often undesirable to apply these formulas in the context of SCTST calculations due to their complexity, and it is usually uneccessary. Instead, the symmetry of molecules is broken by changing the coordinates or masses of one or two atoms slightly, in which case the VPT2 formulas derived above for an asymmetric top molecule can be applied, thereby yielding results of sufficient accuracy for SCTST calculations [116].

There are two additional cases, both known as Fermi resonances [177], that give rise to nearly degenerate states and render the application of nondegenerate perturbation theory potentially problematic. In the first case, one frequency is approximately equal to twice another ($2\omega_i \approx \omega_k$). The two states $\Psi_{\{m\}}^{(0)}$ for which $m_i = n_i \pm 2$ and $m_k = n_k \mp 1$ are nearly degenerate with respect to the zeroth-order state $\Psi_{\{n\}}^{(0)}$, and the denominators in equations (2.49) and (2.50) are approximately zero. This gives rise to terms in the expressions for the anharmonic constants and for G_0 with denominators that are close to zero. The terms in the diagonal anharmonic constant expression can be factored as follows [178]:

$$\frac{f_{iik}^2}{\omega_k^2}\left(\frac{8\omega_i^2 - 3\omega_k^2}{4\omega_i^2 - \omega_k^2}\right) = \frac{f_{iik}^2}{2\omega_k}\left(\frac{1}{2\omega_i + \omega_k} + \frac{4}{\omega_k} - \frac{1}{2\omega_i - \omega_k}\right). \tag{2.70}$$

The last term in the above expression is divergent unless f_{iik} is sufficiently small. The following condition is applied to determine whether it is divergent [116]:

$$\left|\frac{\hbar^3 f_{iik}^4}{256\omega_i^4\omega_k^2(2\omega_i - \omega_k)^3}\right| > 30 \text{ cm}^{-1}. \tag{2.71}$$

If this condition is satisfied, the divergent term is not included when calculating the diagonal anharmonic constants, and the following term is not included when calculating G_0:

$$\frac{3\hbar^2}{64}\frac{f_{iik}^2}{(4\omega_i^2-\omega_k^2)\omega_i^2}. \tag{2.72}$$

The following terms in the expression for the off-diagonal anharmonic constants can be factored as follows [178]:

$$\frac{2f_{iik}^2(\omega_i^2+\omega_k^2-\omega_i^2)}{[(\omega_i+\omega_i)^2-\omega_k^2][(\omega_i-\omega_i)^2-\omega_k^2]} = \frac{f_{iik}^2}{2\omega_k}\left(-\frac{2}{\omega_k}-\frac{1}{2\omega_i+\omega_k}+\frac{1}{2\omega_i-\omega_k}\right). \tag{2.73}$$

If the following condition is satisfied:

$$\left|\frac{\hbar^3 f_{iik}^4}{64\omega_i^4\omega_k^2(2\omega_i-\omega_k)^3}\right| > 30\ \mathrm{cm}^{-1}, \tag{2.74}$$

then the last term in equation (2.73) is not included in the off-diagonal anharmonic constants, and the following term is not included in G_0:

$$\frac{\hbar^2}{4}\frac{f_{iik}^2}{[(\omega_i+\omega_i)^2-\omega_k^2][(\omega_i-\omega_i)^2-\omega_k^2]}. \tag{2.75}$$

In the second type of Fermi resonance, the sum of two frequencies is approximately equal to a third ($\omega_i+\omega_k \approx \omega_j$). The two states $\Psi_{\{m\}}^{(0)}$ for which $m_i = n_i \pm 1$, $m_k = n_k \pm 1$, and $m_j = n_j \mp 1$ are nearly degenerate with respect to $\Psi_{\{n\}}^{(0)}$, giving rise to terms with near-zero denominators in equation (2.63). The corresponding terms in the off-diagonal anharmonic constants are factored as follows [178]:

$$\frac{2f_{ijk}^2(\omega_i^2+\omega_k^2-\omega_j^2)}{[(\omega_i+\omega_k)^2-\omega_j^2][(\omega_i-\omega_k)^2-\omega_j^2]} = \frac{f_{ijk}^2}{2\omega_j}\left(\frac{1}{\omega_i-\omega_k-\omega_j}-\frac{1}{\omega_i+\omega_k+\omega_j}\right.$$
$$\left.-\frac{1}{\omega_i-\omega_k+\omega_j}+\frac{1}{\omega_i+\omega_k-\omega_j}\right). \tag{2.76}$$

The last term in the above expression is not included if:

$$\left|\frac{\hbar^3 f_{ijk}^4}{64\omega_i^2\omega_j^2\omega_k^2(\omega_i+\omega_k-\omega_j)^3}\right| > 30\mathrm{cm}^{-1}, \tag{2.77}$$

in which case the following term is also not included in G_0:

$$\frac{\hbar^2}{4}\frac{f_{ijk}^2}{[(\omega_i+\omega_k)^2-\omega_j^2][(\omega_i-\omega_k)^2-\omega_j^2]}. \tag{2.78}$$

In addition to removing these terms from the above sums, a strictly rigorous treatment with degenerate perturbation theory would also involve diagonalising the coupling matrices $\mathbf{W}$ involving these degenerate states. However, this would have to be done numerically for each state $\Psi^{(0)}_{\{n\}}$ in question, rendering it impossible to obtain a general analytical formula for the energy of this system in terms of its quantum numbers. As will become evident in the next section, an analytical formula substantially simplifies the calculation of reaction probabilities by SCTST. Consequently, terms arising from the diagonalisation of the coupling matrices are typically not included in SCTST calculations. A fully rigorous treatment is more commonly applied in vibrational spectroscopy calculations. In this context, the energies of only a few states are required, which makes numerical calculations tractable, and the accuracy of calculated spacings between energy levels is more important [117, 179–182].

2.4 Cumulative Reaction Probability

VPT2 can be applied to any stationary point of a PES, including a saddle point, at which all vibrational frequencies except for one are real [114]. The imaginary frequency corresponds to the reaction mode eigenvector, which is tangent to the reaction-path at the TS. The F^{th} frequency, ω_F, will be considered to be imaginary in the following analysis. In order to give a real-valued expression for the energy, the F^{th} action variable, $(n_F+1/2)$, must also be imaginary [114]. It is evident that motion along the reaction-path is not separable from other DOFs in the Hamiltonian in this framework, as the energy expression involves products of the F^{th} action variable with other action variables (equation (2.67)). This justifies the application of SCTST to derive an expression for the CRP.

This expression can be derived by first considering the motion of a particle moving in a one-dimensional harmonic potential, $V(x)$. The action variable for this motion, J, is defined as follows [183]:

$$J = \oint p\mathrm{d}x, \tag{2.79}$$

where p is the particle's momentum, and the path integral is over a single oscillation at a constant energy, E. Because a single oscillation involves forward and reverse motion between the turning points of the potential, this integral can be rewritten as follows:

$$J = 2\int p\mathrm{d}x, \tag{2.80}$$

where the limits of integration are the classical turning points. The following relation can be derived using Hamilton-Jacobi Theory, a formulation of classical mechanics equivalent to Lagrangian and Newtonian mechanics [183]:

$$\frac{\partial E}{\partial J} = \nu, \tag{2.81}$$

where ν is the frequency of the vibration. Integrating this expression with respect to J yields:

$$E = \nu J + C'. \tag{2.82}$$

The constant of integration, C', must be 0 because the action variable J must be 0 when the energy is 0 (equation (2.80)). Substituting the expression for the quantized energy levels of a one-dimensional harmonic oscillator,

$$E = h\nu(n + 1/2), \tag{2.83}$$

into equation (2.82) yields the following equation:

$$h(n + 1/2) = 2\int p\mathrm{d}x. \tag{2.84}$$

The same equation applies to motion along the F^{th} action variable of a system of coupled harmonic oscillators [113]:

$$h(n_F + 1/2) = 2 \int p_F \mathrm{d}q_F, \tag{2.85}$$

where p_F is the momentum conjugate to position q_F, which can be defined as follows:

$$p_F = [E_\mathrm{v} - V_{\{n\}'}(q_F)]^{1/2}, \tag{2.86}$$

where E_v is the energy in the F internal DOFs of the system and $V_{\{n\}'}(q_F)$ is the effective potential associated with motion along q_F for a particular configuration $\{n\}'$ of the remaining $F-1$ quantum numbers of the system. Substituting equation (2.86) into equation (2.85) yields:

$$\hbar 2\pi(n_F + 1/2) = 2 \int [E_\mathrm{v} - V_{\{n\}'}(q_F)]^{1/2} \mathrm{d}q_F \tag{2.87}$$

and

$$\frac{\pi(n_F + 1/2)}{i} = \frac{1}{\hbar} \int [V_{\{n\}'}(q_F) - E_\mathrm{v}]^{1/2} \mathrm{d}q_F, \tag{2.88}$$

where the limits of the above integrals are the turning points of $V_{\{n\}'}(q_F)$ at energy E_v. The right side of this expression is equivalent to a barrier penetration integral $\theta_{\{n\}'}(E_\mathrm{v})$. Making this substitution yields:

$$\frac{(n_F + 1/2)}{i} = \frac{\theta_{\{n\}'}(E_\mathrm{v})}{\pi}. \tag{2.89}$$

The energy in the F internal DOFs at the TS, relative to the energy of the reactants, is given as the following VPT2 expression:

$$E_\mathrm{v} = \Delta V_f + G_0 + \sum_{i=1}^{F} \hbar\omega_i(n_i + 1/2) + \sum_{i=1}^{F} \sum_{k=i}^{F} x_{ik}(n_i + 1/2)(n_k + 1/2), \tag{2.90}$$

where ΔV_f is the reaction's forward barrier height. Substituting equation (2.89) into this expression gives:

$$E_{\mathrm{v}} = \Delta V_f + G_0 + \sum_{i=1}^{F-1} \hbar\omega_i (n_i + 1/2) + \sum_{i=1}^{F-1}\sum_{k=i}^{F-1} x_{ik}(n_i + 1/2)(n_k + 1/2) - \frac{\theta_{\{n\}'}(E_{\mathrm{v}})}{\pi}\left[\frac{\hbar\omega_F}{i} + \sum_{i=1}^{F-1}\frac{x_{iF}}{i}(n_i + 1/2)\right] - x_{FF}\frac{\theta_{\{n\}'}(E_{\mathrm{v}})^2}{\pi^2}. \quad (2.91)$$

Solving this equation for $\theta_{\{n\}'}(E_{\mathrm{v}})$ gives:

$$\theta_{\{n\}'}(E_{\mathrm{v}}) = \pi\frac{-\Omega_{\{n\}'} \pm \left[\Omega_{\{n\}'}^2 + 4x_{FF}(\Delta V_f + G_0 + E_{\{n\}'} - E_{\mathrm{v}})\right]^{1/2}}{2x_{FF}}, \quad (2.92)$$

where

$$\Omega_{\{n\}'} = \frac{\hbar\omega_F}{i} + \sum_{i=1}^{F-1}\frac{x_{iF}}{i}(n_i + 1/2) \quad (2.93)$$

and

$$E_{\{n\}'} = \sum_{i=1}^{F-1} \hbar\omega_i (n_i + 1/2) + \sum_{i=1}^{F-1}\sum_{k=i}^{F-1} x_{ik}(n_i + 1/2)(n_k + 1/2). \quad (2.94)$$

$\Omega_{\{n\}'}$ represents an effective reaction mode frequency, through which SCTST accounts for the nonseparability of the Hamiltonian at the TS. $E_{\{n\}'}$ represents the energy in the non-reactive vibrational modes. The effective potential, $V_{\{n\}'}(q_F)$, evaluated at the TS is:

$$V_{\{n\}'}(0) = \Delta V_f + G_0 + E_{\{n\}'}. \quad (2.95)$$

The barrier penetration integral should be 0 when E_{v} equals the energy at the top of the barrier:

$$\theta_{\{n\}'}(V_{\{n\}'}(0)) = 0. \quad (2.96)$$

Only the "+" term in equation (2.92) should be retained to satisfy this condition:

$$\theta_{\{n\}'}(E_{\mathrm{v}}) = \pi\frac{-\Omega_{\{n\}'} + \left[\Omega_{\{n\}'}^2 + 4x_{FF}(\Delta V_f + G_0 + E_{\{n\}'} - E_{\mathrm{v}})\right]^{1/2}}{2x_{FF}}. \quad (2.97)$$

This represents a barrier penetration integral for a particular configuration $\{n\}'$ of quantum numbers of the non-reactive vibrational modes. This expression was further simplified by Barker *et al.* [123] by assuming that $\Omega_{\{n\}'} > 0$. This was not always the

case for the calculations performed in this thesis, so the simplified formula was not used.

The WKB approximation can be used to calculate the probability of tunnelling through a potential barrier from a barrier penetration integral [77]. It is based upon the assumption that the potential barrier changes slowly on the scale of the wavelength of the associated wavefunction. Within this approximation, the state-dependent reaction probability $P_{\{n\}'}(E_\mathrm{v})$ for this configuration is:

$$P_{\{n\}'}(E_\mathrm{v}) = \{1 + \exp\big[2\theta_{\{n\}'}(E_\mathrm{v})\big]\}^{-1}. \tag{2.98}$$

The cumulative reaction probability (CRP) $N(E_\mathrm{v})$ is calculated as a sum over all energetically allowed configurations of $\{n\}'$ at energy E_v [23, 71, 112–114]:

$$N(E_\mathrm{v}) = \sum_{\{n\}'} P_{\{n\}'}(E_\mathrm{v}). \tag{2.99}$$

The maximum energetically allowed quantum number of a particular mode, $n_{\mathrm{max},i}$, is a function of E_v and the quantum numbers of all other non-reactive modes [126]:

$$n_{\mathrm{max},i} = \begin{cases} n_{D,i} & \text{if } E_\mathrm{v} - E_{F-2} \geq D_i \\ n_{D,i}\left[1 - \left(1 - E_\mathrm{v} D_i^{-1}\right)^{1/2}\right] & \text{if } E_\mathrm{v} - E_{F-2} < D_i, \end{cases} \tag{2.100}$$

where E_{F-2} is the vibrational energy calculated from the $F-2$ quantum numbers of the other non-reactive modes (equation (2.67)), and

$$n_{D,i} = -\frac{\hbar\omega_i + \sum_{j\neq i} x_{ij}(n_j + 1/2)}{2x_{ii}} - \frac{1}{2}, \tag{2.101}$$

and

$$D_i = -\frac{\left[\hbar\omega_i + \sum_{j\neq i} x_{ij}(n_j + 1/2)\right]^2}{4x_{ii}}. \tag{2.102}$$

It is further required that the first partial derivatives of the energy in the non-reactive modes with respect to each of the $F-1$ quantum numbers of these modes are greater

than 0, as this ensures that the configuration $\{n\}'$ is "bound," i.e., not beyond the system's dissociation limit [126]. These derivatives are specified as follows:

$$\frac{\partial E_{\{n\}'}}{\partial n_i} = \hbar\omega_i + \sum_{k=1}^{F-1} x_{ik}(n_k + 1/2) + x_{ii}(n_i + 1/2). \tag{2.103}$$

2.5 Thermal Rate Constants

As in other methods, the rate constant $k(T)$ is calculated from a Boltzmann-weighted average of the CRP [71, 112, 133, 184, 185]:

$$k(T) = \frac{1}{h}\frac{Q^{\ddagger}_{\text{trans}}(T)Q^{\ddagger}_{\text{rot}}(T)Q^{\ddagger}_{\text{elec}}(T)\int_0^{\infty} N(E_\text{v})\ \exp\left(-E_\text{v}k_\text{B}^{-1}T^{-1}\right)\mathrm{d}E_\text{v}}{Q_\text{r}(T)}. \tag{2.104}$$

where $Q_\text{r}(T)$ is the partition function for the reactants, and $Q^{\ddagger}_{\text{trans}}(T)$, $Q^{\ddagger}_{\text{rot}}(T)$, and $Q^{\ddagger}_{\text{elec}}(T)$ are the translational, rotational, and electronic partition functions for the transition state. The integral in equation (2.104) is most straightforwardly evaluated by enumerating over all configurations $\{n\}'$ with energies $E_{\{n\}'}$ less than a maximum energy E_max chosen to ensure convergence of the integral. For each configuration, $P_{\{n\}'}(E_\text{v})$ is calculated for all energies from $E_{\{n\}'}$ to E_max.

2.6 Deep Tunnelling Corrections

The treatment discussed thus far sometimes inaccurately represents tunnelling at energies near the reaction's quantum mechanical threshold energy, E_thresh, defined as follows:

$$E_\text{thresh} = \max(\Delta V_f - \Delta V_r, 0), \tag{2.105}$$

where ΔV_r is the reaction's reverse barrier height. This inaccuracy can be understood by considering equation (2.97). This expression is equivalent to the WKB integral for an inverted Morse potential of the following form [125]:

$$V_\text{MP}(q_F) = \Delta V_f + G_0 + E_{\{n\}'} - D + D[2\exp(\alpha q_F) - \exp(2\alpha q_F)], \tag{2.106}$$

with

$$D = -\frac{\Omega_{\{n\}'}^2}{4x_{FF}} \tag{2.107}$$

and

$$\alpha = \frac{(-8x_{FF})^{1/2}}{\hbar}. \tag{2.108}$$

This result arises from the fact that a VPT2 treatment in 1-D yields the exact energy levels of a Morse potential. This is significant because VPT2 neglects fifth and higher derivatives, which are nonzero for a Morse potential. Mills and Robiette [179] commented extensively on this result.

Equation (2.97) is also equivalent to the WKB intergral for a symmetric Eckart potential of the following form [125, 186]:

$$V_{\mathrm{SE}}(q_F) = \Delta V_f + G_0 + E_{\{n\}'} - D + 4D\frac{\exp(\alpha q_F)}{[1+\exp(\alpha q_F)]^2}. \tag{2.109}$$

The reactant asymptotes of these two potential barriers are not E_{thresh}, as would be motivated by physical intuition, and are instead given as follows:

$$\lim_{q_F\to-\infty} V_{\mathrm{MP}}(q_F) = \lim_{q_F\to\pm\infty} V_{\mathrm{SE}}(q_F) = \Delta V_f + G_0 + E_{\{n\}'} - D. \tag{2.110}$$

Consequently, no tunnelling occurs when $E_{\mathrm{thresh}} < E_{\mathrm{v}} < \Delta V_f + G_0 + E_{\{n\}'} - D$, which is physically unrealistic. To correct this, Wagner proposed that the barrier be modeled as a piecewise asymmetric Eckart potential. Details of the construction of this potential can be found in ref [125] and its Supplementary Information. It is defined such that its reactant asymptote is 0 and its product asymptote is $\Delta V_f - \Delta V_r$, which ensures that tunneling is allowed at all energies greater than E_{thresh}. The potential is also defined to be smooth and continuous. The barrier penetration integral for this potential can be calculated analytically to obtain $\theta_{\{n\}'}(E_{\mathrm{v}})$ [125]. $P_{\{n\}'}(E_{\mathrm{v}})$

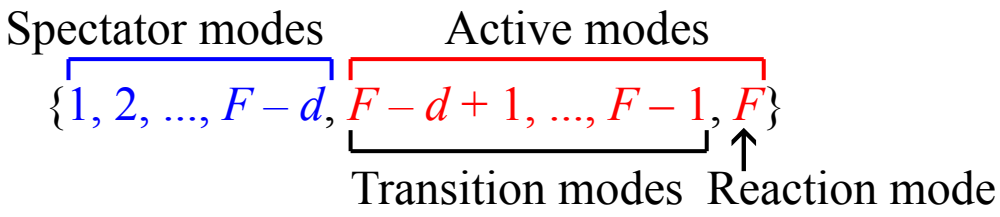


Figure 2.1: Diagram showing the paritioning of the F internal DOFs of the TS into $F-d$ spectator modes and d active modes. The set of active modes includes the reaction mode, with index F. The remaining $d-1$ active modes are transition modes.

is then calculated as follows [74]:

$$P_{\{n\}'}(E_\mathrm{v}) = \begin{cases} \{1+\exp\left[2\theta_{\{n\}'}(E_\mathrm{v})\right]\}^{-1} & \text{if } E_\mathrm{v} - E_{\{n\}'} < \Delta V_f + G_0, \\ 1 - P_{\{n\}'}(2(\Delta V_f + G_0 + E_{\{n\}'}) - E_\mathrm{v}) & \text{if } \Delta V_f + G_0 < E_\mathrm{v} - E_{\{n\}'} \leq \\ & \quad V_2 + E_{\{n\}'} \\ 1 & \text{if } V_2 + E_{\{n\}'} < E_\mathrm{v} - E_{\{n\}'} \end{cases} \tag{2.111}$$

where

$$V_2 = \Delta V_f + 2G_0 + \min(\Delta V_f, \Delta V_r). \tag{2.112}$$

This method for calculating the CRP and rate constants will be referred to as SCTST-W. The method discussed in the previous section, without deep tunnelling corrections, will be referred to as SCTST-M.

2.7 The Reduced-Dimensionality Framework

In a reduced-dimensionality SCTST calculation, anharmonic constants are calculated for only a subset of d vibrational DOFs of the system (the active modes). The remaining $F-d$ modes (the spectator modes) are assumed to be harmonic, so the third and fourth derivatives in equations (2.18) and (2.19) involving these modes are zero (Figure 2.1). In this case, according to equations (2.64) and (2.68), the diagonal and off-diagonal anharmonic constants for the spectator modes are 0. Anharmonic constants for the active modes also differ from their FD counterparts, as does G_0.

Assigning the value 0 to third and fourth derivatives along active modes yields the following formulas for these parameters:

$$x_{ii} = \frac{\hbar^2}{16\omega_i^2}\left(f_{iiii} - \sum_{k=F-d+1}^{F} \frac{f_{iik}^2}{\omega_k^2}\frac{8\omega_i^2 - 3\omega_k^2}{4\omega_i^2 - \omega_k^2}\right) \tag{2.113}$$

$$x_{ik} = \frac{\hbar^2}{4\omega_i\omega_k}\left(f_{iikk} - \sum_{j=F-d+1}^{F} \frac{f_{iij}f_{jkk}}{\omega_j^2} + \sum_{j=F-d+1}^{F} \frac{2f_{iik}^2(\omega_i^2 + \omega_k^2 - \omega_i^2)}{[(\omega_i+\omega_k)^2 - \omega_i^2][(\omega_i-\omega_k)^2 - \omega_i^2]}\right), i < k \tag{2.114}$$

$$G_0 = \frac{\hbar^2}{64}\sum_{i=F-d+1}^{F}\frac{f_{iiii}}{\omega_i^2} - \frac{7\hbar^2}{576}\sum_{i=F-d+1}^{F}\frac{f_{iii}^2}{\omega_i^2} + \frac{3\hbar^2}{64}\sum_{i\neq k}\frac{f_{iik}^2}{(4\omega_i^2 - \omega_k^2)\omega_i^2} - \frac{\hbar^2}{4}\sum_{i<j<k}\frac{f_{ijk}^2}{[(\omega_i+\omega_k)^2 - \omega_j^2][(\omega_i-\omega_k)^2 - \omega_j^2]}. \tag{2.115}$$

Active modes other than the reaction mode are defined as "transition modes" (Figure 2.1). Considering the set $\{n\}''$ of quantum numbers of the transition modes yields formulas for the terms used in an RD SCTST calculation:

$$\Omega_{\{n\}''} = \frac{\hbar\omega_F}{i} + \sum_{i=F-d+1}^{F-1}\frac{x_{iF}}{i}(n_i + 1/2) \tag{2.116}$$

and

$$E_{\{n\}''} = \sum_{i=F-d+1}^{F-1}\hbar\omega_i(n_i + 1/2) + \sum_{i=F-d+1}^{F-1}\sum_{k=i}^{F-1}x_{ik}(n_i + 1/2)(n_k + 1/2), \tag{2.117}$$

where the reaction mode is not included in the sums above. When the third and fourth derivatives involving the spectator modes are 0 in the FD formulas, they exhibit the following relationships with the RD formulas:

$$\Omega_{\{n\}'} = \Omega_{\{n\}''} \tag{2.118}$$

and

$$E_{\{n\}''} = E_{\{n\}'} - \sum_{i=1}^{F-d}\hbar\omega_i(n_i + 1/2). \tag{2.119}$$

Considering the definitions of $\theta_{\{n\}'}(E_\mathrm{v})$ and $P_{\{n\}'}(E_\mathrm{v})$ (equations (2.97) and (2.98)) gives:

$$\theta_{\{n\}''}(E_\mathrm{v}) = \theta_{\{n\}'}\left(E_\mathrm{v} + \sum_{i=1}^{F-d} \hbar\omega_i(n_i + 1/2)\right) \tag{2.120}$$

and therefore

$$P_{\{n\}''}(E_\mathrm{v}) = P_{\{n\}'}\left(E_\mathrm{v} + \sum_{i=1}^{F-d} \hbar\omega_i(n_i + 1/2)\right) \tag{2.121}$$

or, equivalently:

$$P_{\{n\}''}(E'_\mathrm{v}) = P_{\{n\}'}(E_\mathrm{v}) \tag{2.122}$$

where

$$E'_\mathrm{v} = E_\mathrm{v} - \sum_{i=1}^{F-d} \hbar\omega_i(n_i + 1/2). \tag{2.123}$$

Following analysis similar to that presented in ref [133], this expression can be substituted into the Boltzmann-weighted integral of the CRP:

$$\int_0^\infty \exp\left(-E_\mathrm{v}k_\mathrm{B}^{-1}T^{-1}\right) \sum_{n_1=0} ... \sum_{n_{F-1}=0} P_{\{n\}'}(E_\mathrm{v})\mathrm{d}E_\mathrm{v}, \tag{2.124}$$

which yields:

$$\int_0^\infty \exp\left(-E_\mathrm{v}k_\mathrm{B}^{-1}T^{-1}\right) \sum_{n_1=0} ... \sum_{n_{F-1}=0} P_{\{n\}''}(E'_\mathrm{v})\mathrm{d}E_\mathrm{v}. \tag{2.125}$$

Changing the variable of integration from E_v to E'_v yields the following:

$$\prod_{i=1}^{F-d} \sum_{n_i=0}^{\infty} \exp\left(\hbar\omega_i(n_i + 1/2)k_\mathrm{B}^{-1}T^{-1}\right) \times \int_0^\infty \exp\left(-E'_\mathrm{v}k_\mathrm{B}^{-1}T^{-1}\right) \sum_{n_{F-d+1}=0} ... \sum_{n_{F-1}=0} P_{\{n\}''}(E'_\mathrm{v})\mathrm{d}E'_\mathrm{v}. \tag{2.126}$$

The integrand of the above expression is the RD CRP, $N_\mathrm{RD}(E'_\mathrm{v})$, weighted by a Boltzmann factor:

$$N_\mathrm{RD}(E'_\mathrm{v}) = \sum_{\{n\}''} P_{\{n\}''}(E'_\mathrm{v}). \tag{2.127}$$

The first part of equation (2.126) is a harmonic partition function for the spectator modes, here denoted $Q^{\ddagger}_{\mathrm{spec}}(T)$, which has been used previously in other RD studies [146, 150, 158]. Thus, the expression for the rate constant in the RD framework is:

$$k_{\mathrm{RD}}(T) = \frac{1}{h}\frac{Q^{\ddagger}_{\mathrm{trans}}(T)Q^{\ddagger}_{\mathrm{rot}}(T)Q^{\ddagger}_{\mathrm{elec}}(T)Q^{\ddagger}_{\mathrm{spec}}(T)\int_0^{\infty} N_{\mathrm{RD}}(E_{\mathrm{v}})\ \exp\left(-E_{\mathrm{v}}k_{\mathrm{B}}^{-1}T^{-1}\right)\mathrm{d}E_{\mathrm{v}}}{Q_{\mathrm{r}}(T)}. \tag{2.128}$$

In calculating the RD CRP, one needs only to enumerate over energetically allowed configurations $\{n\}''$ of the $d-1$ transition modes, which yields efficiency in dynamics calculations in RD SCTST.

Chapter 3

SCTST Calculations on Analytical Potential Energy Surfaces

3.1 Introduction

The aim of this chapter is to rigorously evaluate the accuracy of RD approaches to SCTST through calculations using 2-D PESs with which RD QRS calculations have previously been performed [146, 150, 158]. Because the same PESs are used in these comparisons, differences in the resulting rate constants can arise only from differences in how the RD QRS and RD SCTST methods treat the system's dynamics, and not from differences in the underlying PESs. Results from other quantum mechanical methods are also presented, but comparison with these results is less relevant because different PESs constructed at a different *ab initio* level of theory were used in these calculations. The aim of this chapter is not to evaluate the validity of the PESs considered. Rather, it is to evaluate RD SCTST as a means of obtaining accurate rate constants from a given RD PES. Furthermore, the effect of the deep tunnelling corrections to SCTST (section 2.6) are evaluated within the 1-D and 2-D frameworks.

First, an overview of the methods used to construct the RD PESs are given, including a discussion of the coordinate systems they employ. Two methods for calculating frequencies and anharmonic constants from these PESs are then presented, and their relative accuracies and efficiencies are discussed. Results from 1-D and

2-D SCTST calculations are given for reactions (1.1)–(1.4). In a 2-D calculation, anharmonic constants are calculated for the reaction mode and one transition mode. The extent to which the anharmonicity of the transition mode and the coupling between the modes contributes to 2-D rate constants are analysed.

3.2 Methods

3.2.1 Potential Energy Surface Construction

The reduced-dimensionality potential energy surfaces (RD PESs) considered here were constructed previously by others. Methods for their construction are therefore discussed in detail elsewhere [145, 150, 152, 158]. Briefly, *ab initio* calculations are performed on a grid in (r_1, r_2) coordinate space. For the generic hydrogen atom abstraction or exchange reaction $\mathrm{Y} + \mathrm{H_aZ} \longrightarrow \mathrm{YH_a} + \mathrm{Z}$, r_1 is the Y-$\mathrm{H_a}$ distance, and r_2 is the distance between $\mathrm{H_a}$ and the atom in Z to which $\mathrm{H_a}$ is bonded (Figure 3.1). At each grid point, the bond lengths r_1 and r_2 are fixed, and the remaining $3N - 8$ degrees of freedom (the spectator modes) are optimised to minimise the energy calculated using second-order Møller-Plesset Perturbation Theory (MP2) with a correlation consistent polarised valence triple-zeta Dunning (cc-pVTZ) basis set. The single-point energy is then calculated at this geometry using coupled cluster electronic structure methods (CCSD(T)/cc-pVTZ for reactions (1.1), (1.2), and (1.4), and CCSD(T)-F12a/cc-pVTZ-F12a for reaction (1.3)).

These electronic structure methods recover some of the system's correlation energy, making them more accurate than single-reference methods like Hartree-Fock (HF) [187, 188]. In the MP2 method, the difference between the system's Born-Oppenheimer Hamiltonian operator and the sum of the mean-field Fock operators is considered as a perturbation to the HF energy. The HF wavefunction is used to calculate the magnitude of this perturbation to second-order. Coupled cluster (CC)

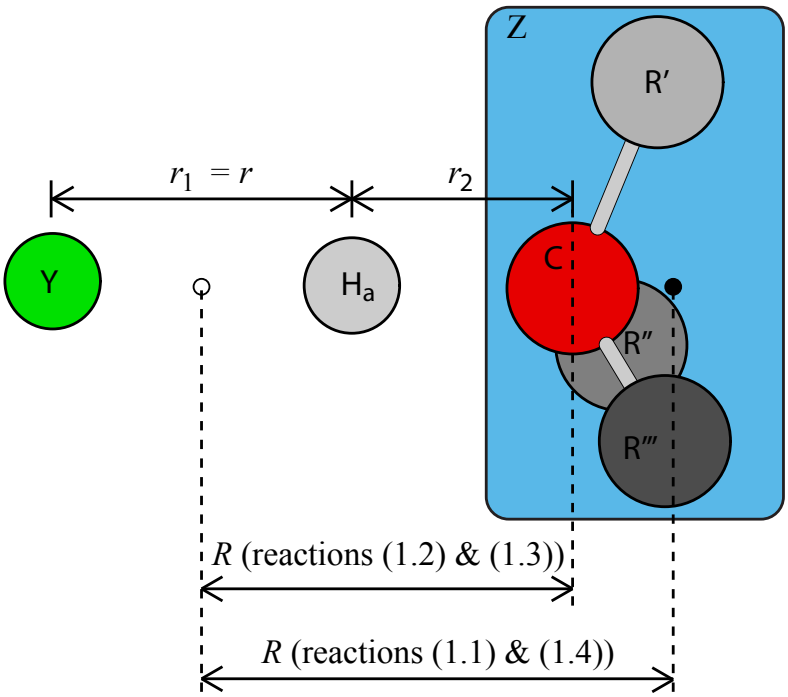


Figure 3.1: The bond lengths (r_1 and r_2) and Jacobi coordinates (r and R) used to construct the PESs for the generic reaction $\mathrm{Y} + \mathrm{H_aZ} \longrightarrow \mathrm{YH_a} + \mathrm{Z}$. The Z fragment represents a hydrocarbon, with R′, R″, and R‴ bonded to the central C atom. The white and black circles denote the centers of mass of $\mathrm{H_aY}$ and Z, respectively. Note the differing definitions of the Jacobi coordinate R among the reactions considered in this study.

methods calculate the energy variationally, using a sum of the HF wavefunction and excited-state wavefunctions as a reference. Relationships between the amplitudes for higher- and lower-order excited state wavefunctions can be exploited to yield gains in efficiency. The CCSD(T) method calculates the amplitudes for single and double excitations explicitly and uses these amplitudes to calculate contributions to the energy associated with triple excitations from fourth- and fifth-order perturbation theory [189]. A particular choice of basis set is required for each of these electronic structure methods. The cc-pVTZ basis set was designed to facilitate recovery of more of the system's correlation energy with fewer primitive basis functions [188, 190]. The CCSD(T)-F12a method makes use of basis functions that explicitly include inter-electronic distances, which enables recovery of more of the correlation energy with a smaller basis set [191–193].

Motion corresponding to stretching of the $Y-H_a$ and H_a-Z bonds is projected out of the Hessian matrix, enabling calculation of the "post-projection" frequencies of the spectator modes. In the case of reactions (1.1) and (1.4), the curvilinear projection method [150, 151, 194] is used. Rectilinear projection [195] is used for reactions (1.2) and (1.3). The zero-point energy (ZPE) of these modes is then added to the single-point energy to account explicitly for their effect on the PES.

At each grid point, the Jacobi coordinates r and R are calculated from the partially optimised geometry. r is defined as the distance between H_a and the Y atom or moiety (H for reactions (1.1)–(1.3), and the C atom in CH_3 for reaction 1.4). For reactions (1.1) and (1.4), R is the distance between the centers of mass of fragments YH_a and Z. For reactions (1.2) and (1.3), R is defined differently as the distance between the center of mass of YH_a and the atom in the Z fragment to which H_a is bonded. In the case of reaction (1.3), this choice was made due to the presence of a van der Waals complex that affects the behaviour of the reaction-path in conventional Jacobi

coordinates. This has been discussed in more detail previously [158]. Both definitions of R are consistent with the Bending-Corrected Rotating Linear Model used in QRS calculations and with the treatment of the system as a three-body system in this thesis, as it is equally valid to consider the motion of Y and H_a relative to either the center of mass of Z or the C atom in Z.

Jacobi coordinates are then transformed into hyperspherical coordinates ρ and δ as follows:

$$\rho = \left[\left(\frac{m_1}{\mu} \right) R^2 + \left(\frac{m_2}{\mu} \right) r^2 \right]^{1/2} \tag{3.1}$$

and

$$\delta = \tan^{-1} \left[\frac{r}{R} \left(\frac{m_2}{m_1} \right)^{1/2} \right], \tag{3.2}$$

where

$$m_1 = \frac{(m_Y + m_H) m_Z}{m_Y + m_H + m_Z} \tag{3.3}$$

and

$$m_2 = \frac{m_Y m_H}{m_Y + m_H}, \tag{3.4}$$

where m_Y and m_Z are the masses of the Y and Z fragments, respectively, and m_H is the mass of an H atom. Although the mass μ uniquely defines a transformation from Jacobi to hyperspherical coordinates, it can be defined arbitrarily for the purpose of QRS calculations due to the presence of a factor of μ in the Hamiltonian operator in hyperspherical coordinates. μ is defined as follows for the PESs considered in this thesis:

$$\mu = (m_1 m_2 m_3)^{1/3}. \tag{3.5}$$

For reactions (1.1), (1.3), and (1.4), m_3 is defined as:

$$m_3 = \frac{m_C (m_Z - m_C)}{m_Z}. \tag{3.6}$$

For reaction (1.2), m_3 is defined as:

$$m_3 = \frac{(m_{\mathrm{C}} + 2m_{\mathrm{H}})(m_{\mathrm{C}} + 3m_{\mathrm{H}})}{2m_{\mathrm{C}} + 5m_{\mathrm{H}}}. \tag{3.7}$$

m_{C} and m_{H} are the masses of C and H atoms, respectively. Following this coordinate transformation to hyperspherical coordinates, the ZPE-corrected *ab initio* energies are then fit to a double-Morse potential function, $V(\rho, \delta)$, in hyperspherical coordinates (section 3.2.5). A 29-parameter function of the following form is used for reactions (1.1), (1.2), and (1.3) [145, 151, 158]:

$$\begin{aligned} V(\rho,\delta) = {} & [c_1 + c_2\rho^{c_3}\exp(-c_4\rho)]\left(\left\{1 - \exp\left[(c_5 + c_6\rho + c_7\rho^2)\delta + (c_8 + c_9\rho + c_{10}\rho^2)\right.\right.\right. \\ & \left.\left.\left. - \log\left(c_{11} + c_{12}\rho + c_{13}\rho^2\right)\right]\right\}^2 - c_{14}\right) + [c_{15} + c_{16}\rho^{c_{17}}\exp(-c_{18}\rho)]\left[(1 - \exp\left\{-\left[(c_{19}\right.\right.\right. \\ & \left.\left.\left. + c_{20}\rho + c_{21}\rho^2)\delta + (c_{22} + c_{23}\rho + c_{24}\rho^2) + \log\left(c_{25} + c_{26}\rho + c_{27}\rho^2\right)\right]\right\}\right)^2 - c_{28}\Bigg] + c_{29}. \end{aligned} \tag{3.8}$$

Only 18 parameters re required for the function for reaction (1.4) due to its symmetry [152]:

$$\begin{aligned} V(\rho,\delta) = {} & [1 + c_1\rho^{c_2}\exp(c_3\rho)]\, c_4\left(\left\{1 - \exp\left[\left(c_5 + c_6\rho + c_7\rho^2\right)\right.\right.\right. \\ & \left.\left.\left.\left(\frac{c_8 + c_9\rho + c_{10}\rho^2 - \log(c_{11} + c_{12}\rho + c_{13}\rho^2)}{c_{14} + c_{15}\rho + c_{16}\rho^2} - \delta\right)\right]\right\}^2 + (\{1 - \\ & \exp\left[\left(c_5 + c_6\rho + c_7\rho^2\right)\left(\frac{c_8 + c_9\rho + c_{10}\rho^2 - \log(c_{11} + c_{12}\rho + c_{13}\rho^2)}{c_{14} + c_{15}\rho + c_{16}\rho^2} + \delta - \delta_{\max}\right)\right]\right\}^2 \\ & - 2c_{17})\,, \end{aligned} \tag{3.9}$$

where $\delta_{\max}$ is the reaction's skewing angle, or the value of δ at the reactant asymptote, given as follows [152]:

$$\delta_{\max} = \tan^{-1}\left(\left[\frac{m_{\mathrm{H}}(m_{\mathrm{Y}} + m_{\mathrm{Z}} + m_{\mathrm{H}})}{m_{\mathrm{Y}}m_{\mathrm{Z}}}\right]^{1/2}\right). \tag{3.10}$$

Detailed discussions of the choice of this function and the methods for fitting it to *ab initio* data points can be found in previous studies and references therein [146, 158].

3.2.2 Frequency and Anharmonic Constant Calculations

Two methods are investigated for calculating frequencies and anharmonic constants from RD PESs defined in Jacobi coordinates. In both methods, the hyperspherical coordinates corresponding to the TS geometry, $(\rho_{\mathrm{TS}}, \delta_{\mathrm{TS}})$, are calculated numerically using Newton-Raphson root-finding. In the first of these methods, the Jacobi coordinates of the system are transformed into Cartesian coordinates along the Y–H_a–Z axis with the assumption that these three moieties are collinear at the TS. For reactions (1.1) and (1.4), they are exactly collinear, as is evident from symmetry considerations. For reactions (1.2) and (1.3), the angle of the Y, H_a, and Z moieties is 178° and 176°, respectively.

Derivatives of the PES with respect to the Cartesian coordinates of each moiety are calculated analytically as follows:

$$\frac{\partial}{\partial x_{\mathrm{Y}}} = -\frac{m_{\mathrm{Y}}}{m_{\mathrm{Y}} + m_{\mathrm{H}}}\frac{\partial}{\partial R} - \frac{\partial}{\partial r}, \tag{3.11}$$

$$\frac{\partial}{\partial x_{\mathrm{H}}} = -\frac{m_{\mathrm{H}}}{m_{\mathrm{Y}} + m_{\mathrm{H}}}\frac{\partial}{\partial R} + \frac{\partial}{\partial r}, \tag{3.12}$$

and

$$\frac{\partial}{\partial x_{\mathrm{Z}}} = \frac{\partial}{\partial R}. \tag{3.13}$$

The chain rule is applied to calculate derivatives of $V(\rho, \delta)$, in hyperspherical coordinates, with respect to the Jacobi coordinates r and R:

$$\frac{\partial}{\partial r} = \left(\frac{m_2}{\mu}\right)^{1/2}\left(\sin\delta\frac{\partial}{\partial \rho} + \frac{\cos\delta}{\rho}\frac{\partial}{\partial \delta}\right) \tag{3.14}$$

$$\frac{\partial}{\partial R} = \left(\frac{m_1}{\mu}\right)^{1/2}\left(\cos\delta\frac{\partial}{\partial \rho} - \frac{\sin\delta}{\rho}\frac{\partial}{\partial \delta}\right). \tag{3.15}$$

The masses m_{Y}, m_{H}, and m_{Z} are used to weight the 3×3 Hessian matrix in Cartesian coordinates, and the mass-weighted Hessian is diagonalised to calculate the frequencies of the reaction mode and transition mode. The derivatives along normal modes

required for anharmonic constant calculations are then calculated as follows:

$$\frac{\partial}{\partial q_i} = \mathbf{v}_i \cdot \left(m_{\mathrm{Y}}^{-1/2} \frac{\partial}{\partial x_{\mathrm{Y}}}, m_{\mathrm{H}}^{-1/2} \frac{\partial}{\partial x_{\mathrm{H}}}, m_{\mathrm{Z}}^{-1/2} \frac{\partial}{\partial x_{\mathrm{Z}}} \right), \tag{3.16}$$

where the vector $\mathbf{v}_i$ is a normalised eigenvector of the mass-weighted Hessian.

In the second method for calculating frequencies and anharmonic constants, the assumption of collinearity at the TS is removed. The velocities $\mathbf{v}_{\mathrm{Y}}$, $\mathbf{v}_{\mathrm{H}}$, and $\mathbf{v}_{\mathrm{Z}}$ of each of the three moieties are considered in three-dimensional space. Subtracting the kinetic energy associated with center-of-mass translation of the system,

$$T_{\mathrm{COM}} = \frac{1}{2} \left(m_{\mathrm{Y}} + m_{\mathrm{H}} + m_{\mathrm{Z}} \right) \left(\frac{m_{\mathrm{Y}} \mathbf{v}_{\mathrm{Y}} + m_{\mathrm{H}} \mathbf{v}_{\mathrm{H}} + m_{\mathrm{Z}} \mathbf{v}_{\mathrm{Z}}}{m_{\mathrm{Y}} + m_{\mathrm{H}} + m_{\mathrm{Z}}} \right)^2, \tag{3.17}$$

from the total kinetic energy of the system,

$$T_{\mathrm{tot}} = \frac{1}{2} \left(m_{\mathrm{Y}} \mathbf{v}_{\mathrm{Y}}^2 + m_{\mathrm{H}} \mathbf{v}_{\mathrm{H}}^2 + m_{\mathrm{Z}} \mathbf{v}_{\mathrm{Z}}^2 \right), \tag{3.18}$$

yields the following, after simplification:

$$T_{\mathrm{rel}} = \frac{1}{2} \left(m_1 v_R^2 + m_2 v_r^2 \right), \tag{3.19}$$

where v_R and v_r are the time derivatives of the Jacobi coordinates, and m_1 and m_2 are defined as in equations (3.3) and (3.4). Expanding the potential V as a Taylor series to second order in R and r enables a typical normal mode analysis (section 2.2), whereby the mass-weighted Hessian matrix H in Jacobi coordinates is diagonalised to yield two frequencies and normal mode eigenvectors:

$$H = \begin{pmatrix} m_1^{-1} \frac{\partial^2 V}{\partial^2 R} & (m_1 m_2)^{-1/2} \frac{\partial^2 V}{\partial R \partial r} \\ (m_1 m_2)^{-1/2} \frac{\partial^2 V}{\partial R \partial r} & m_2^{-1} \frac{\partial^2 V}{\partial^2 r} \end{pmatrix}. \tag{3.20}$$

Derivatives along the eigenvectors of this matrix, $\{\mathbf{v}_i'\}$, are then calculated as follows:

$$\frac{\partial}{\partial q_i} = \mathbf{v}_i' \cdot \left(m_1^{-1/2} \frac{\partial}{\partial R}, m_2^{-1/2} \frac{\partial}{\partial r} \right). \tag{3.21}$$

All derivatives are calculated analytically from PES functions using Mathematica, version 8.0 [196]. Calculating derivatives along normal mode eigenvectors using Jacobi

instead of Cartesian coordinates requires differentiation along two dimensions instead of three. Measurements of the CPU time required to apply each method to the four reactions considered in this study indicate that the second of these two approaches is, on average, 43 times faster than the first.

Three unique anharmonic constants are used in a 2-D SCTST calculation: two diagonal anharmonic constants for the reaction mode and transition mode (x_{FF} and x_{11}, respectively), and one off-diagonal anharmonic constant (x_{1F}). These 2-D anharmonic constants can be calculated using equations (2.113) and (2.115). Simplified expressions for these anharmonic constants are given below:

$$x_{FF} = \frac{\hbar^2}{16\omega_F^2}\left(f_{FFFF} - \frac{5f_{FFF}^2}{3\omega_F^2} - \frac{f_{1FF}^2(8\omega_F^2 - 3\omega_1^2)}{\omega_1^2(4\omega_F^2 - \omega_1^2)}\right), \tag{3.22}$$

$$x_{11} = \frac{\hbar^2}{16\omega_1^2}\left(f_{1111} - \frac{5f_{111}^2}{3\omega_1^2} - \frac{f_{11F}^2(8\omega_1^2 - 3\omega_F^2)}{\omega_F^2(4\omega_1^2 - \omega_F^2)}\right), \tag{3.23}$$

and

$$x_{1F} = \frac{\hbar^2}{4\omega_1\omega_F}\left(f_{11FF} - \frac{f_{111}f_{1FF}}{\omega_1^2} - \frac{f_{11F}f_{FFF}}{\omega_F^2} + \frac{2f_{11F}^2\omega_F^2}{[(\omega_1+\omega_F)^2 - \omega_1^2][(\omega_1-\omega_F)^2 - \omega_1^2]} + \frac{2f_{1FF}^2\omega_1^2}{[(\omega_1+\omega_F)^2 - \omega_F^2][(\omega_1-\omega_F)^2 - \omega_F^2]}\right). \tag{3.24}$$

The formula for G_0 in the 2-D framework is given by equation (2.115) and presented in simplified form here:

$$G_0 = \sum_{i=1}^{2}\hbar^2\left(\frac{1}{64}\frac{f_{iiii}}{\omega_i^2} - \frac{5}{576}\frac{f_{iii}^2}{\omega_i^4}\right) + \frac{3}{64}\sum_{i\neq j}\frac{\hbar^2 f_{iij}^2}{\omega_i^2(4\omega_i^2 - \omega_j^2)}, \tag{3.25}$$

Third and fourth derivatives along the spectator mode eigenvectors are assumed not to contribute to the active mode anharmonic constants and G_0.

In a 1-D SCTST calculation, third and fourth derivatives with respect to the transition mode (f_{111}, f_{11F}, f_{1FF}, f_{1111}, and f_{11FF}) are considered to be 0, such

that the transition mode is treated harmonically as a spectator mode. Within this framework, x_{11} and x_{1F} are 0, and x_{FF} is calculated as follows:

$$x_{FF} = \frac{\hbar^2}{16\omega_F^2}\left(f_{FFFF} - \frac{5f_{FFF}^2}{3\omega_F^2}\right). \tag{3.26}$$

It is interesting to note that the 2-D and 1-D diagonal anharmonic constants for the reaction mode (x_{FF}) differ because the 2-D constant depends on f_{1FF}. G_0 is given in the 1-D framework as follows:

$$G_0 = \hbar^2\left(\frac{1}{64}\frac{f_{FFFF}}{\omega_F^2} - \frac{5}{576}\frac{f_{FFF}^2}{\omega_F^4}\right). \tag{3.27}$$

3.2.3 Minimum-Energy Path Calculations

Methods for calculating the reaction-path, or minimum-energy path (MEP), of a FD PES are well documented [74, 76]. The MEP is defined as the union of the paths of steepest descent in mass-weighted coordinates from the TS to the reactant and product channels [74]. This section provides a brief overview of a method for calculating the MEP of an RD PES defined in Jacobi coordinates. Coordinates along the MEP are calculated numerically at discrete steps. The coordinates of the first steps from the TS towards the reactant and product channels are calculated from positive and negative displacements along the reaction-mode eigenvector, which is tangent to the MEP at the TS. The coordinates of subsequent steps are calculated by displacing the system in mass-weighted Jacobi coordinate space along the negative gradient vector, specified as follows:

$$\nabla\mathbf{V} = -\left(m_1^{-1/2}\frac{\partial V}{\partial R}, m_2^{-1/2}\frac{\partial V}{\partial r}\right). \tag{3.28}$$

This vector is normalised to yield a unit vector tangent to the MEP, and displacements in the direction given by this unit vector are specified in units of (length mass$^{-1/2}$). An arbitrary scaling mass μ, often assigned the value 1 Da, is often used to define

displacements along the MEP instead in units of (length). This is not done in this chapter, although the numerical values of the reaction coordinate presented are equivalent to those that would be obtained if a scaling mass $\mu = 1m_e$ is used. A step size of 0.001 $a_0 m_e^{1/2}$ is used in this chapter.

3.2.4 Barrier Height Calculations

Forward and reverse barrier heights are calculated from points on the analytical PESs corresponding to the TS, product, and reactant geometries. The forward barrier height is calculated as follows:

$$\Delta V_f = V(\rho_{TS}, \delta_{TS}) - V(\rho_{max}, \delta_r) - \frac{\hbar}{2}\left(\frac{m_H + m_Z}{m_H m_Z}\frac{\partial^2 V}{\partial R^2}\bigg|_{\rho=\rho_{max},\delta=\delta_r}\right)^{1/2}, \qquad (3.29)$$

where ρ_{max} is the maximum value of ρ considered in QRS calculations performed on each PES ($30a_0$, $26a_0$, $12a_0$, and $15a_0$ for reactions (1.1), (1.2), (1.3), and (1.4), respectively). δ_r, the value of δ at the minimum of the reactant well at $\rho = \rho_{max}$, was calculated numerically by Newton-Raphson root finding. The last term in equation (3.29) represents the ZPE of the reactant C–H bond and must be included because ZPE is not included in the vibrational component of the reactant partition function, $Q_r(T)$. The ZPE of the other reactant vibrational modes are included in the PES function $V(\rho, \delta)$. The ZPE of the TS is not included because it is included in $E_{\{n\}''}$ (equation (2.117)).

The reverse barrier height is calculated in a manner similar to the forward barrier height:

$$\Delta V_r = V(\rho_{TS}, \delta_{TS}) - V(\rho_{max}, \delta_p) - \frac{\hbar}{2}\left(\frac{m_H + m_Y}{m_H m_Y}\frac{\partial^2 V}{\partial r_1^2}\bigg|_{\rho=\rho_{max},\delta=\delta_p}\right)^{1/2}. \qquad (3.30)$$

The derivative with respect to r_1, the product bond length, is approximated as follows, based on the assumption that the TS is collinear:

$$\frac{\partial}{\partial r_1} = \frac{\partial}{\partial r} + \frac{m_Y}{m_Y + m_H}\frac{\partial}{\partial R} \qquad (3.31)$$

Rate constants calculated by SCTST are significantly less sensitive to the reverse barrier height than to the forward barrier height, so this approximation is expected to have a negligible effect on the accuracy of results.

3.2.5 Rate Constant Calculations

Rate constants were calculated by 1-D and 2-D SCTST from these RD anharmonic constants as described in section 2.7. In 2-D calculations, the set $\{n\}''$ contains one quantum number for the transition mode. In the 1-D calculation, $E_{\{n\}''}$ is 0, and $\Omega_{\{n\}''} = \mathrm{Im}(\hbar\omega_F)$. A maximum energy $E_{\max}$ equal to 20 times the forward barrier height (equation (3.29)) of each reaction was chosen to ensure convergence of the integral in equation (2.128).

These results were compared to QRS results from previous work by others [146, 150, 158]. In these previous studies, the R-matrix propagation scheme was used to solve the TI Schrödinger equation [197]. The Hamiltonian is given in hyperspherical coordinates as follows:

$$\hat{H} = -\frac{1}{2\mu}\left(\frac{\partial^2}{\partial\rho^2} + \frac{1}{\rho^2}\frac{\partial^2}{\partial\delta^2} - \frac{3}{4\rho^2} - \frac{\hat{J}^2}{\rho^2}\right) + V(\rho,\delta). \tag{3.32}$$

The angular momentum J is assumed to be 0, according to the J-shifting model, in which rotational DOFs are assumed not to be coupled to internal DOFs [23, 24, 198], as is commonly assumed in SCTST calculations. The R-matrix propagation scheme yields a scattering matrix, $\mathbf{S}$, from which the CRP $N_{\mathrm{QRS}}(E_{\mathrm{v}})$ is calculated as follows:

$$N_{\mathrm{QRS}}(E_{\mathrm{v}}) = \sum_{i,f} |\mathbf{S}_{i\to f}(E_{\mathrm{v}})|^2, \tag{3.33}$$

where the subscripts i and f denote the initial and final states of the reactants and products, respectively. The rate constant is then calculated from the CRP as in RD SCTST.

Rate constants were also calculated using conventional TST as a basis for comparison using the following expression [76]:

$$k_{\mathrm{TST}}(T) = \frac{k_{\mathrm{B}}T}{h}\frac{Q^{\ddagger}_{\mathrm{trans}}(T)Q^{\ddagger}_{\mathrm{rot}}(T)Q^{\ddagger}_{\mathrm{elec}}(T)Q^{\ddagger}_{\mathrm{vib}}(T)\exp\left(-\Delta V_f k_{\mathrm{B}}^{-1}T^{-1}\right)}{Q_{\mathrm{r}}(T)}, \tag{3.34}$$

where $Q^{\ddagger}_{\mathrm{vib}}(T)$ is the classical harmonic partition function for the $3N-7$ vibrational DOFs of the TS with real frequencies.

3.3 Results

3.3.1 Energetics

TS frequencies for the reactions considered in this chapter are presented in Table 3.1. Pre- and post-projection frequencies were calculated in previous studies from *ab initio* calculations [145, 150, 158] and are also reported in Table 3.1. Post-projection frequencies represent the frequencies of the remaining DOFs after motion along the bond lengths r_1 and r_2 is projected out of the Hessian matrix. By comparing the pre- and post-projection frequencies, one can identify the frequencies of the active modes treated in the RD framework. These are shown in bold in Table 3.1. The frequencies of the other spectator modes are predominantly unchanged, which indicates that the active modes are not strongly coupled to the spectator modes. In the case of reaction (1.2), post-projection frequencies were not provided in ref [145], so pre- and post-projection frequencies from a later 2-D QRS study [154] are presented in Table 3.1 and were used in calculations. Approximate calculations suggest that using these frequencies to calculate rate constants affected results by no more than 4% from 250 K to 1000 K.

Frequencies calculated for each reaction from their respective 2-D PESs according to the two methods presented in section 3.2.2 can be found in Table 3.1. Both methods yield equivalent frequencies due to the collinearity or near-collinearity of the TS. For

Table 3.1: TS frequencies for the reactions considered in this chapter[a]

Reaction		Frequencies (cm^{-1})			
$H + CH_4$ (1.1)[c]	pre-	**1648.6*i***	543.5 (2)	1076.5	1131.5 (2)
$T_c = 410$ K[b]		1457.6 (2)	**1941.4**	3127.8	3289.4 (2)
	post-	543.5 (2)	1047.5	1131.5 (2)	1457.6 (2)
		3125.5	3289.4 (2)		
	2-D PES	**1782.3*i***	**1352.9**		
$H + C_2H_6$ (1.2)[d]	pre-	**1665*i***	199	306	569
$T_c = 367$ K		836	870	1049	1117
		1181	1185	1242	1412
		1487	1509 (2)	**1848**	3068
		3141	3149	3169	3239
	post-	199	308	569	836
		852	1052	1126	1181
		1194	1242	1412	1487
		1509	1510	3068	3141
		3148	3169	3239	
	2-D PES	**1603.0*i***	**1390.0**		
$H + cyc-C_3H_6$ (1.3)[e]	pre-	**1342.3*i***	274.7	313.0	760.9
$T_c = 351$ K		815.5	871.1	886.5	952.0
		1023.6	1034.0	1074.4	1121.6
		1124.5	1165.9	1202.6	1267.2
		1486.4	1520.8	**2255.2**	3177.0
		3177.6	3257.2	3261.8	3272.3
	post-	272.7	313.0	760.4	815.5
		859.9	886.5	952.0	1023.6
		1033.8	1074.4	1121.6	1123.8
		1171.2	1202.6	1269.4	1486.4
		1521.6	3176.6	3177.6	3255.4
		3261.8	3271.2		
	2-D PES	**1527.6*i***	**1537.5**		
$CH_3 + CH_4$ (1.4)[b]	pre-	**1949.8*i***	48.5	322.5 (2)	**540.8**
$T_c = 387$ K		706.2 (2)	1164.5	1197.7	1375.7 (2)
		1463.1 (2)	1489.9 (2)	3109.2	3110.6
		3257.4 (2)	3257.8 (2)		
	post-	48.5	322.5 (2)	706.2 (2)	1052.3
		1074.6	1375.7 (2)	1463.1 (2)	1489.9 (2)
		3090.0	3109.2	3257.4 (2)	3257.8 (2)
	2-D PES	**1683.6*i***	**494.4**		

[a]Frequencies pre- and post-projection, and calculated from derivatives of the 2-D PES as described in section 3.2.2. Numbers in parentheses denote degeneracies.
[b]The reaction's crossover temperature, calculated from the 2-D PES imaginary frequency as described in ref [199].
[c]From ref [150]. [d]From ref [154]. [e]From ref [158].

Table 3.2: Anharmonic constants, G_0 parameters, and barrier heights for the reactions considered in this chapter

	Reaction (1.1)	Reaction (1.2)	Reaction (1.3)	Reaction (1.4)
x_{FF} (2-D)[a]	-166.44	-317.26	-254.57	-109.95
x_{FF} (1-D)[a]	-248.68	-485.39	-539.89	-174.01
x_{1F} (2-D)[a]	$-160.59i$	$-340.96i$	$-618.85i$	$-32.78i$
x_{11} (2-D)[a]	0.33	14.36	109.75	-1.64
G_0 (2-D)[b]	-240.43	-383.86	-338.20	-195.75
G_0 (1-D)[b]	-265.34	-446.41	-485.31	-198.21
ΔV_f^c	11.409	7.647	9.488	16.170
ΔV_r^c	11.786	4.504	4.800	16.170

[a]Anharmonic constants (cm^{-1}) calculated according to equations (3.22)–(3.24) and (3.26).
[b]G_0 parameters (μE_h) calculated from equations (3.25) and (3.27).
[c]Barrier heights (kcal mol^{-1}) used in SCTST calculations, as calculated according to equations (3.29) and (3.30).

reactions (1.1)–(1.3), the reaction mode frequencies calculated from the 2-D PESs are within 200 cm^{-1} of the pre-projection reaction mode frequencies, but the transition mode frequencies are less than the corresponding pre-projection frequencies, by as much as 718 cm^{-1}. In the case of reaction (1.4), the transition mode frequency from the 2-D PES (494.4 cm^{-1}) is closer to the corresponding pre-projection frequency (540.8 cm^{-1}), but the reaction mode frequency differs more than in the other reactions (1683.6i cm^{-1} from the 2-D PES vs. 1949.8i cm^{-1} pre-projection). These differences arise from the RD nature of the PESs, in particular that they only treat motion in 2 DOFs while the pre-projection active modes can include motion in 3 dimensions for each atom. Furthermore, the 2-D PESs include the zero-point energies (ZPE) of the spectator modes and were constructed by fitting a PES to *ab initio* calculations performed at a different level of theory. Both of these factors may contribute further to these discrepancies.

The crossover temperatures, T_c for each reaction are also presented in Table 3.1. This temperature represents the temperature at which the contribution to the reaction

rate from tunnelling is approximately equal to that from thermally activated classical motion over the reaction barrier [199]. Thus, quantum mechanical effects dominate at temperatures less than T_c, and classical effects dominate at greater temperatures. The crossover temperature is calculated from the frequency of the reaction mode, ω_F, as follows [199]:

$$T_c = \frac{\hbar|\omega_F|}{2\pi k_B}. \tag{3.35}$$

The anharmonic constants used in SCTST calculations are presented in Table 3.2. The anharmonic constants for the transition mode (x_{1F} and x_{11}) are both zero in the 1-D case (section 3.2.2). Anharmonic constants for the reaction mode (x_{FF}) in the 2-D case are considerably different from their 1-D counterparts due to the third term in equation (3.22), which is not present in equation (3.26). For reaction (1.1), the absolute value of this term constitutes 49% of the 2-D x_{FF} parameter, and because it is negative, the magntiude of the 1-D x_{FF} parameter is 49% greater than that of the 2-D parameter. For reactions (1.2)–(1.4), the 1-D x_{FF} parameters differ from their 2-D counterparts by factors of 1.53, 2.12, and 1.58, respectively. Differences between 1-D and 2-D values of G_0 were considerably greater for reactions (1.1)–(1.3) than for reaction (1.4). The forward and reverse barrier heights of reaction (1.4) are equal due to its symmetry.

3.3.2 2-D Rate Constants

3.3.2.1 $H + CH_4 \longrightarrow H_2 + CH_3$ (reaction (1.1))

Rate constants for reaction (1.1) calculated using the 2-D SCTST-M method are presented in Figure 3.2 and Table 3.3 (page 59). These exhibit acceptable agreement with QRS results [150] between 250 and 1000 K, differing at most by a factor of 3.77 at 250 K. At temperatures less than the crossover temperature for this reaction, 410 K, rate constants calculated using QRS are significantly greater than those from

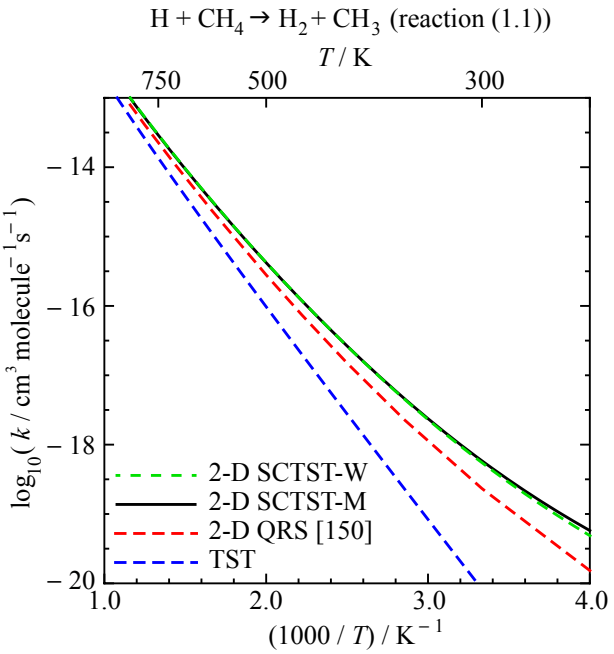


Figure 3.2: Rate constants for reaction (1.1) calculated by the 2-D SCTST-M and -W methods (black and dashed green curves, respectively) and by conventional TST (dashed blue curve) with QRS results calculated using the same PES (dashed red curve) [150].

conventional TST, differing by a factor of 185 at 250 K. This degree of difference (2–3 orders of magnitude) between QRS and TST rate constants is not unusual for reactions involving the abstraction or exchange of a light H atom. It reflects the inclusion of quantum mechanical tunneling effects in QRS and the neglect of these effects in TST. For this reason, and because reaction rate constants vary by several orders of magnitude from 250 K to 1000 K, agreement to within a factor of 10 of results from approximate theories like SCTST with those from "exact" theories, i.e. QRS, is often considered reasonable.

The same PES was used to calculate the rate constants in the QRS and 2-D SCTST methods, so discrepancies between their results arise from differences in how both methods treat the system's dynamics. Results from other theoretical studies [59, 60, 100] are presented in Figure 3.3, but comparisons between these results and the SCTST results in this chapter are not as important. It is difficult to evaluate the

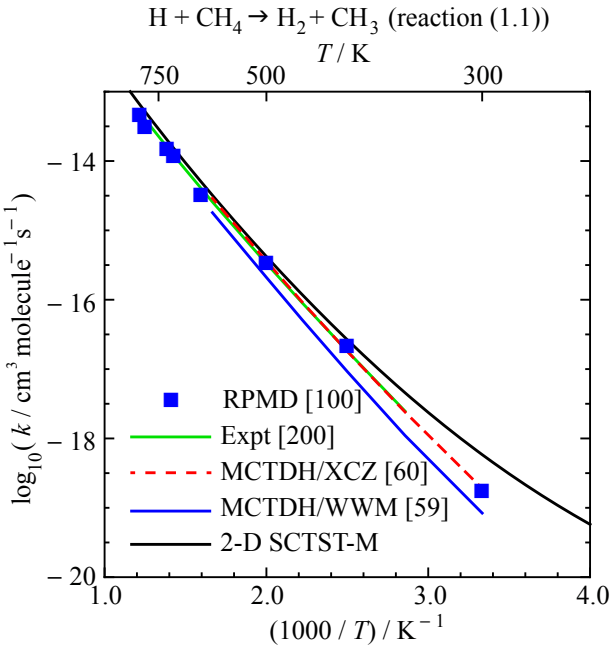


Figure 3.3: Rate constants for reaction (1.1) from the 2-D SCTST-M method (black curve) and from other theoretical and experimental studies. Results from RPMD [100] are presented as blue squares, from the multi-configurational time-dependent Hartree (MCTDH) method on the XCZ PES [60] as the red curve, and from MCTDH on the WWM PES [59] as the blue curve. The experimental results (green curve) are from ref [200].

extent to which discrepancies arise from differences in the PESs used in these calculations versus differences in their treatments of the system's dynamics. Nevertheless, results from 2-D SCTST-M exhibited acceptable agreement with these other results. Rate constants calculated by all RD SCTST methods are presented in Table 3.3.

The 2-D SCTST-M rate constant converges with the QRS rate constant as T increases but is greater at low T. This behaviour arises from differences in the cumulative reaction probability (CRP) calculated in both methods.[1] The CRP is multiplied by a Boltzmann factor and integrated with respect to energy to calculate the rate constant (equation (2.128)). Consequently, the CRP at lower energies contributes more to this integral than the CRP at greater energies. At 250 K, the integral is

[1]The CRP in the QRS framework, which was used to make Figure 3.4, was calculated from the PES using the R-matrix propagation method [197] by X. Shan.

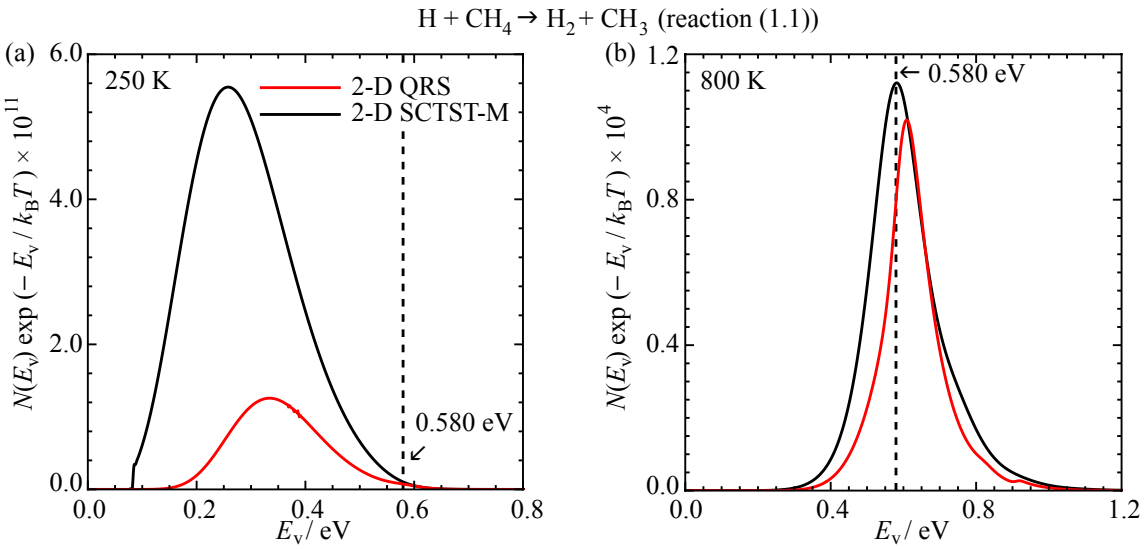


Figure 3.4: Product of the cumulative reaction probability (CRP), $N_{\mathrm{RD}}(E_{\mathrm{v}})$, from the 2-D SCTST-M method (black curve) for reaction (1.1) and the corresponding CRP from QRS (red curve), with a Boltzmann factor evaluated at (a) $T = 250$ K and (b) $T = 800$ K. The dashed vertical line denotes the vibrationally adiabatic barrier height from the 2-D SCTST-M method.

determined primarily by the CRP at energies less than approximately 0.6 eV. Because the CRP from the 2-D SCTST method is greater than that from QRS at these energies, the Boltzmann-weighted CRP is also greater (Figure 3.4(a)), and the 2-D SCTST method yields a greater rate constant at 250 K. At energies near the reaction's vibrationally adiabatic barrier height (indicated by vertical dashed lines in Figures 3.4(a) and 3.4(b)), the CRPs of the two methods are closer in value. The Boltzmann factor emphasizes this energy range more as T increases. Consequently, the Boltzmann-weighted CRPs from the two methods, and therefore the rate constants, become closer in value (Figure 3.4(b)).

Further insight into the differences between the QRS and 2-D SCTST-M rate constants can be gained by considering the potential barriers in Figure 3.5(a). The black curve shows the symmetric Eckart potential constructed using the energetic parameters from the 2-D SCTST-M calculation (equation (2.109)). In constructing this

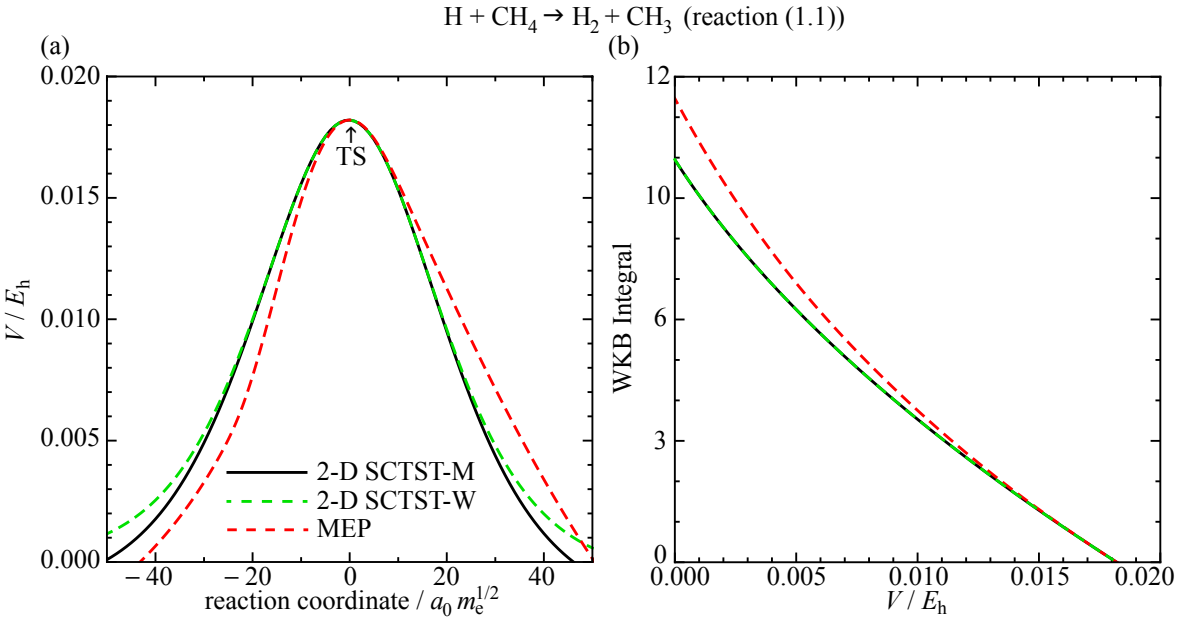


Figure 3.5: (a) The potential barrier for reaction (1.1) as a function of the reaction coordinate along the minimum-energy path (MEP) of the PES (dashed red curve), and the potential barriers corresponding to the 2-D SCTST-M (black curve) and SCTST-W (blue curve) calculations. The latter were constructed for the case in which $\Omega_{\{n\}''} = |\hbar\omega_F|$ to enable comparison with the MEP barrier from the PES. (b) WKB integrals for each of these barriers as a function of energy V.

barrier, coupling between the reaction mode and the transition mode was neglected. Consequently, the $E_{\{n\}''}$ parameter was assigned the values 0, and $\Omega_{\{n\}''}$ was assigned the value $|\hbar\omega_F|$. This was done to facilitate comparison with the barrier along the MEP of the PES.

Figure 3.5(b) presents the barrier penetration integrals, calculated using WKB Theory, for each of these barriers, as functions of energy. At low energies, the MEP barrier is wider than the 2-D SCTST-M barrier, resulting in a greater integral for the MEP barrier. The widths of the barriers are more similar near the TS, so the integrals converge as the energy approaches the barrier height. It is important to note that these integrals cannot be used directly to calculate reaction probabilities because they do not include coupling effects. Furthermore, the QRS method treats quantum mechanical tunnelling in 2-D instead of only along the MEP. Nevertheless, in the

Table 3.3: Rate constants for reaction (1.1) ($H + CH_4$), in units cm^3 $molecule^{-1}$ s^{-1}, calculated using TST, the SCTST methods discussed in this chapter, and QRS[a]

T(K)	TST	2-D SCTST-M	1-D SCTST-M	2-D SCTST-W	1-D SCTST-W	QRS[b]
200	8.52(−26)	4.57(−21)	9.07(−22)	3.03(−21)	2.97(−21)	5.67(−22)
250	8.26(−23)	5.77(−20)	2.99(−20)	4.85(−20)	5.02(−20)	1.53(−20)
300	8.25(−21)	5.84(−19)	4.64(−19)	5.46(−19)	5.82(−19)	2.33(−19)
350	2.26(−19)	4.55(−18)	4.27(−18)	4.42(−18)	4.75(−18)	2.25(−18)
400	2.77(−18)	2.65(−17)	2.65(−17)	2.61(−17)	2.80(−17)	1.50(−17)
450	1.98(−17)	1.18(−16)	1.21(−16)	1.17(−16)	1.25(−16)	7.34(−17)
500	9.73(−17)	4.20(−16)	4.34(−16)	4.19(−16)	4.43(−16)	2.80(−16)
600	1.11(−15)	3.20(−15)	3.32(−15)	3.21(−15)	3.36(−15)	2.34(−15)
700	6.57(−15)	1.51(−14)	1.56(−14)	1.52(−14)	1.58(−14)	1.16(−14)
800	2.59(−14)	5.17(−14)	5.32(−14)	5.19(−14)	5.37(−14)	4.07(−14)
1000	1.90(−13)	3.24(−13)	3.31(−13)	3.25(−13)	3.34(−13)	2.57(−13)
1300	1.34(−12)	2.05(−12)	2.09(−12)	2.06(−12)	2.10(−12)	1.57(−12)
1600	4.92(−12)	7.22(−12)	7.32(−12)	7.26(−12)	7.38(−12)	5.24(−12)
2000	1.65(−11)	2.36(−11)	2.38(−11)	2.37(−11)	2.40(−11)	1.57(−11)

[a]Numbers in parentheses denote powers of 10.
[b]From ref [150].

absence of significant corner-cutting, tunnelling along the MEP can be considered approximately as the primary contribution to reaction probabilities at energies less than the barrier height [74]. Thus, comparing these barriers provides an approximate idea of the relative amount of tunnelling associated with each barrier. The MEP barrier is somewhat wider than the 2-D SCTST-M barrier. This is a possible reason why the QRS rate constants are less than the 2-D SCTST-M rate constants at low T.

The 2-D SCTST-W barrier is similar in shape to the 2-D SCTST-M barrier, differing only at low energies (Figure 3.5(a)). For this reason, the WKB integrals associated with each barrier are also similar (Figure 3.5(b)). Consequently, the 2-D SCTST-M rate constants do not differ significantly from those calculated using the 2-D SCTST-W method (Figure 3.2, Table 3.3). At 250 K, the 2-D SCTST-M rate constant is 19% greater than the 2-D SCTST-W rate constant.

3.3.2.2 $H + C_2H_6 \longrightarrow H_2 + C_2H_5$ (reaction (1.2))

Rate constants for reaction (1.2) are presented in Figure 3.6 and Table 3.4 (page 63). The 2-D SCTST-M rate constant is 853 times greater than the TST rate constant at 260 K. Differences between 2-D SCTST-M rate constants and QRS results [145] are greater than for reaction (1.1). Rate constants from 2-D SCTST-M are 9.67 times greater than those from QRS at 260 K, indicating that the 2-D SCTST-M method overestimates contributions from tunnelling for this reaction. This discrepancy highlights a key difference between the SCTST and QRS methods. SCTST depends only upon the shape of the PES at the TS, whereas QRS uses the complete PES from the interaction region near the TS to the asymptotic region in the product and reactant channels. In the QRS method employed in ref [145], the CRP at lower energies is more sensitive to the shape of the PES in the asymptotic region than near the TS [152]. Rate constants are more sensitive to the CRP at lower energies due to the Boltzmann factor in equation (2.128), particularly at lower temperatures, at which QRS and 2-D SCTST rate constants differ more. Discrepancies between the fitted PES and the *ab initio* calculations to which it was fitted are greater near the TS than in the asymptotic region [145], which may indicate that the accuracy of the shape of the PES near the TS could be improved. If true, this would affect SCTST calculations more than QRS calculations. The difficulties involved in fitting a PES accurately have been discussed in detail previously [154]. For example, there are many different configurations of the 29 function parameters that minimize the sum of the squares of the differences between the fitted PES and *ab initio* calculations, and it is difficult, if not impossible, to find a global, rather than a local, minimum. Furthermore, some *ab initio* calculations are often excluded from the fit [153]. The fitting procedures used to obtain the PES for this reaction were not as rigorous as those used for the other reactions [145].

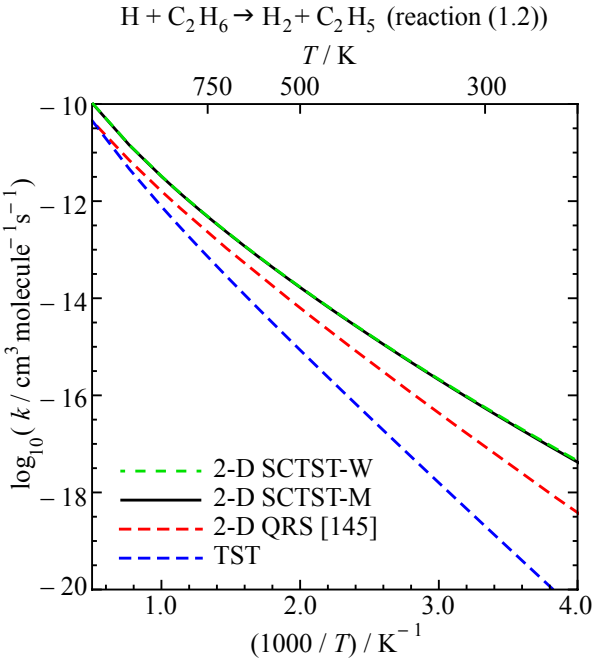


Figure 3.6: Rate constants for reaction (1.2) from the 2-D SCTST-M and -W methods (black and dashed green curves, respectively), TST (dashed blue curve), and QRS (dashed red curve) [145].

Differences between the 2-D SCTST-M and QRS results are further reflected in the plots of the Boltzmann-weighted CRPs associated with both methods (Figures 3.7(a) and 3.7(b)). At energies below the reaction's vibrationally adiabatic barrier height, the CRP from the 2-D SCTST-M method is significantly greater than that from QRS, even though the barrier along the MEP is significantly narrower than that associated with the 2-D SCTST-M method (Figure 3.7(c)). There are two possible explanations. In calculating the barrier heights for SCTST calculations from the PES, it was assumed that the zero-point energy in the reactant C–H bond could be obtained from a harmonic expansion of the PES in the reactant well. However, such a harmonic approximation may not be sufficient. According to an approximate VPT2 calculation, the anharmonic ZPE of this bond is 0.025 kcal mol^{-1} less than the harmonic ZPE, so the barrier height with this anharmonic effect included is 0.025 kcal mol^{-1} greater than the barrier height used in the original 2-D SCTST-M calculation.

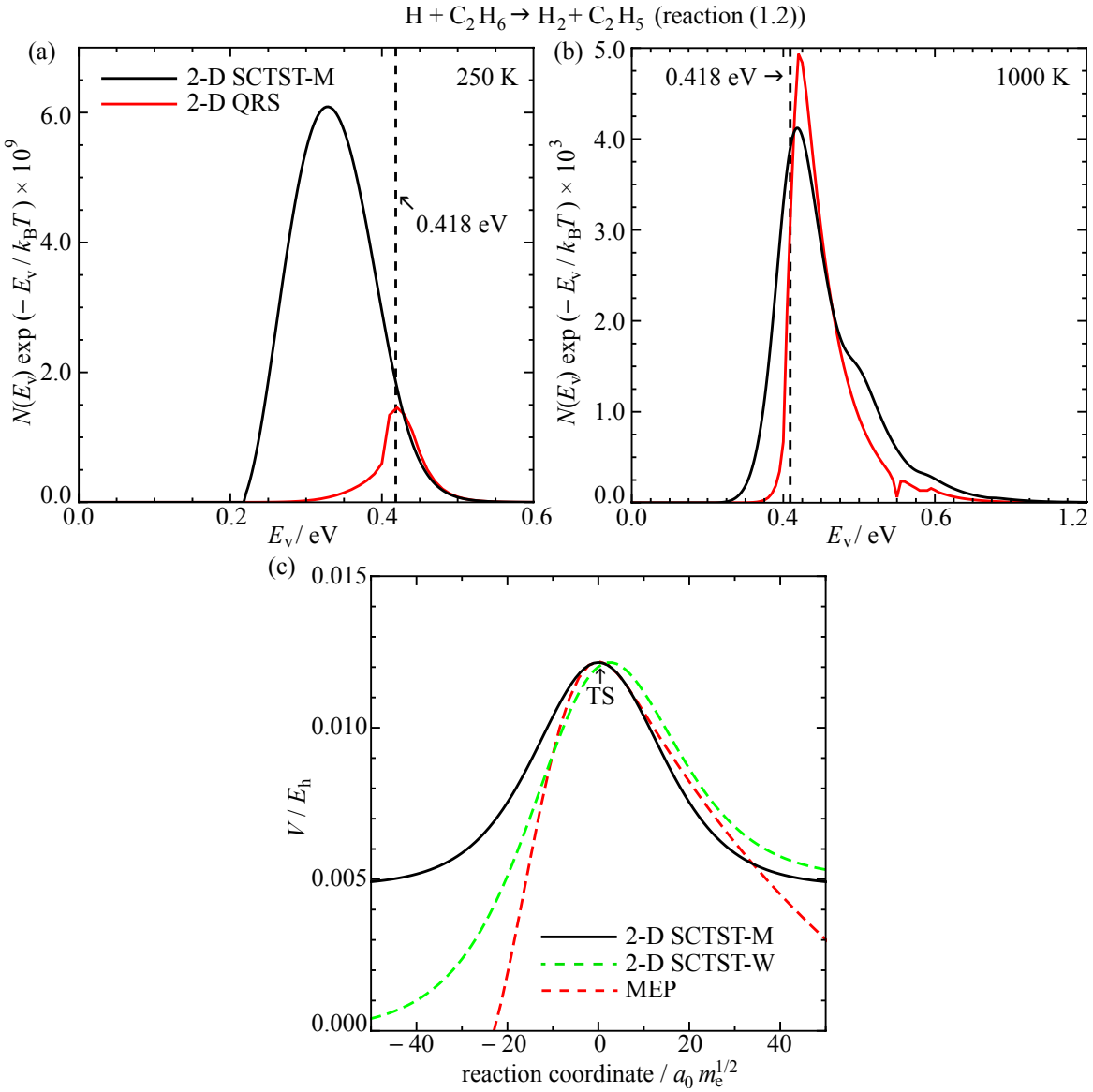


Figure 3.7: (a) and (b) The Boltzmann weighted CRPs from the 2-D SCTST-M (black curve) and QRS (red curve) methods for reaction (1.2), evaluated at 250 K and 1000 K, respectively. The vibrationally adiabatic barrier is indicated by a dashed vertical line. (c) Potential barriers along the MEP of the fitted PES (dashed red curve) and from 2-D SCTST-M (black curve) and 2-D SCTST-W (dashed green curve) calculations in which $\Omega_{\{n\}''} = |\hbar\omega_F|$.

Table 3.4: Rate constants for reaction (1.2) ($H + C_2H_6$), in units cm^3 $molecule^{-1}$ s^{-1}, calculated by TST, SCTST, and QRS[a]

T(K)	TST	2-D SCTST-M	1-D SCTST-M	2-D SCTST-W	1-D SCTST-W	QRS[b]
200	7.97(−24)	1.21(−19)	1.35(−19)	1.36(−19)	2.32(−19)	4.08(−21)
260	8.78(−21)	7.49(−18)	8.98(−18)	7.91(−18)	1.17(−17)	7.74(−19)
320	7.31(−19)	1.25(−16)	1.49(−16)	1.29(−16)	1.73(−16)	2.36(−17)
360	6.28(−18)	5.27(−16)	6.19(−16)	5.39(−16)	6.89(−16)	1.27(−16)
420	7.55(−17)	2.94(−15)	3.38(−15)	2.99(−15)	3.63(−15)	9.08(−16)
480	5.01(−16)	1.13(−14)	1.28(−14)	1.15(−14)	1.35(−14)	4.11(−15)
520	1.41(−15)	2.41(−14)	2.69(−14)	2.45(−14)	2.82(−14)	9.43(−15)
680	2.81(−14)	2.30(−13)	2.49(−13)	2.33(−13)	2.58(−13)	1.06(−13)
880	2.88(−13)	1.44(−12)	1.53(−12)	1.46(−12)	1.58(−12)	7.12(−13)
1000	7.78(−13)	3.24(−12)	3.42(−12)	3.29(−12)	3.51(−12)	1.61(−12)
1300	4.57(−12)	1.42(−11)	1.49(−11)	1.44(−11)	1.52(−11)	6.92(−12)
2000	4.55(−11)	1.05(−10)	1.09(−10)	1.06(−10)	1.11(−10)	4.50(−11)

[a]Numbers in parentheses denote powers of 10.
[b]From ref [145].

Using this modified barrier height results in a 2-D SCTST-M rate constant 5% less than the original rate constant at 260 K, i.e. in slightly improved agreement with the QRS results. Furthermore, the QRS method may simulate more reflection at low energies than SCTST due to the fact that it treats quantum mechanical effects in 2-D. This may further reduce the CRP.

Results from the 2-D SCTST-M method agreed closely with those from another 2-D QRS study [154] and from two experimental studies [201, 202] (Figure 3.8). In spite of this degree of agreement, it is important to remember that comparison with QRS results from the same PES is more important than comparison with other theoretical results based on a different PES or with experimental results. Results from the 2-D SCTST-M and SCTST-W methods agree very closely, differing by only 6% at 250 K.

3.3.2.3 $H + cyc-C_3H_6 \longrightarrow H_2 + cyc-C_3H_5$ (reaction (1.3))

Rate constants calculated for reaction (1.3) are given in Figure 3.9 and Table 3.5. The 2-D SCTST-M method reproduces results from QRS well, yielding results greater

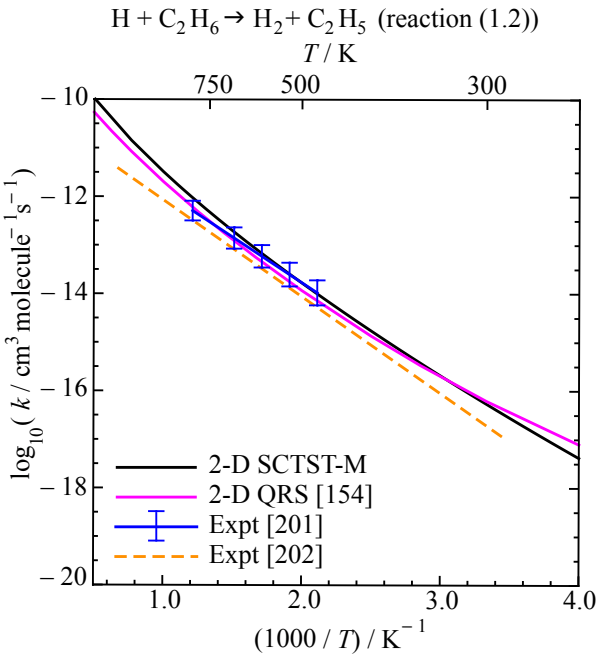


Figure 3.8: 2-D SCTST-M results for reaction (1.2) presented in comparison to rate constants calculated using 2-D QRS on a different PES [154] (magenta curve), and two experimental studies [201, 202] (blue and dashed orange curves).

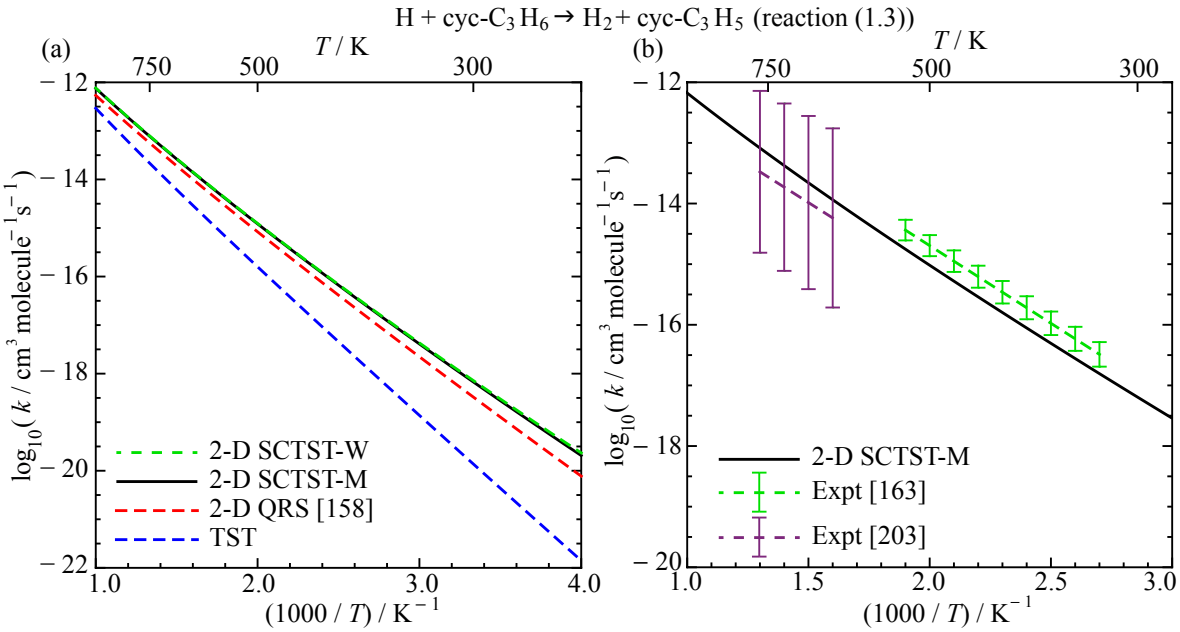


Figure 3.9: (a) 2-D SCTST-M and 2-D SCTST-W rate constants (black and dashed green curves, respectively) for reaction (1.3), with QRS (dashed red curve) [158] and TST (dashed blue curve) results for comparison. (b) Experimental results from two previous studies (dashed green and dashed purple curves) [163, 203].

Table 3.5: Rate constants for reaction (1.3) ($H + cyc-C_3H_6$), in units cm^3 $molecule^{-1}$ s^{-1}, calculated by TST, SCTST, and QRS[a]

T(K)	TST	2-D SCTST-M	1-D SCTST-M	2-D SCTST-W	1-D SCTST-W	QRS[b]
360	6.49(−19)	1.39(−17)	2.15(−17)	1.45(−17)	2.59(−17)	8.08(−18)
390	2.90(−18)	4.62(−17)	6.84(−17)	4.77(−17)	7.97(−17)	2.83(−17)
420	1.05(−17)	1.31(−16)	1.88(−16)	1.35(−16)	2.13(−16)	8.38(−17)
450	3.24(−17)	3.28(−16)	4.57(−16)	3.36(−16)	5.10(−16)	2.17(−16)
480	8.73(−17)	7.42(−16)	1.01(−15)	7.58(−16)	1.11(−15)	5.02(−16)
510	2.10(−16)	1.54(−15)	2.04(−15)	1.57(−15)	2.22(−15)	1.06(−15)
540	4.63(−16)	2.96(−15)	3.87(−15)	3.02(−15)	4.17(−15)	2.08(−15)
630	3.21(−15)	1.51(−14)	1.89(−14)	1.54(−14)	2.01(−14)	1.09(−14)
660	5.49(−15)	2.39(−14)	2.96(−14)	2.43(−14)	3.12(−14)	1.73(−14)
690	8.99(−15)	3.64(−14)	4.46(−14)	3.70(−14)	4.69(−14)	2.64(−14)
720	1.42(−14)	5.38(−14)	6.54(−14)	5.47(−14)	6.86(−14)	3.91(−14)
750	2.16(−14)	7.73(−14)	9.32(−14)	7.86(−14)	9.76(−14)	5.63(−14)

[a]Numbers in parentheses denote powers of 10.
[b]From ref [158].

than those from QRS by a factor of 2.66 at 250 K. 2-D SCTST-M rate constants are 146 times greater than the TST rate constants at 250 K. These results lie within the range of results from two previous experimental studies [163, 203], as shown in Figure 3.9(b). 2-D SCTST-W results are marginally greater than those from the 2-D SCTST-M method, differing by 12% at 250 K.

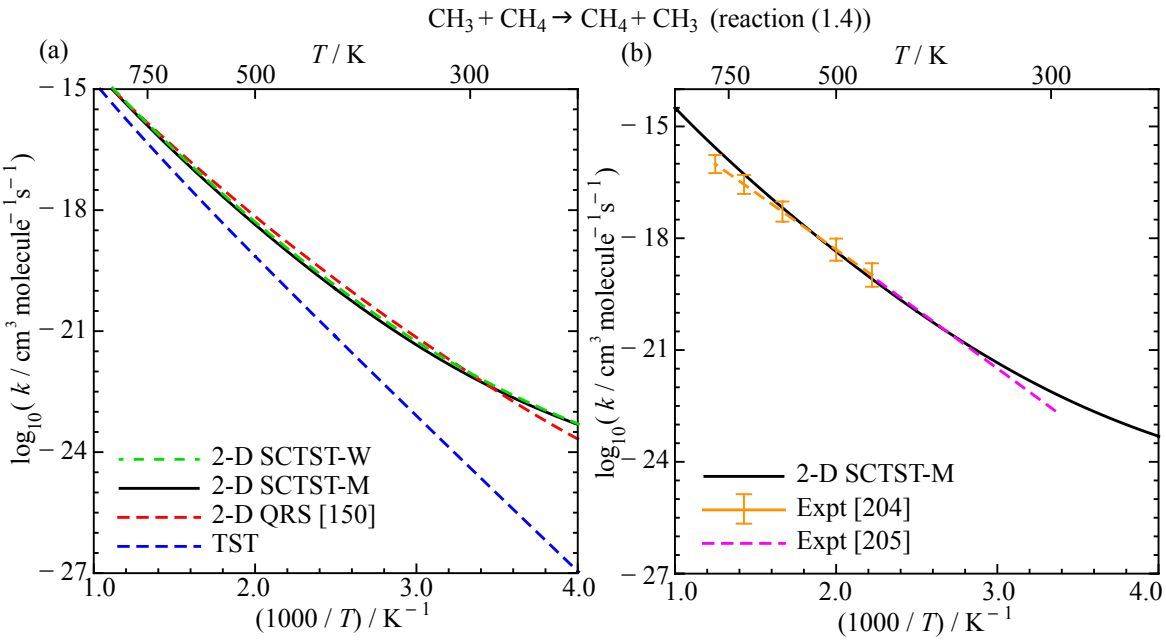


Figure 3.10: (a) Rate constants for reaction (1.4) calculated by 2-D SCTST-M (black curve) and 2-D SCTST-W (dashed green curve) with results from QRS (red dashed curve) [150] and TST (dashed blue curve). (b) Experimental results (dashed orange and dashed magenta curves) [204, 205].

3.3.2.4 $CH_3 + CH_4 \longrightarrow CH_4 + CH_3$ (reaction (1.4))

2-D rate constants for this reaction are presented in Figure 3.10 and Table 3.6. At 250 K, the 2-D SCTST-M rate constant is 3.20 times greater than the rate constant calculated by QRS and 6108 times greater than the TST rate constant. The fact that the ratio of the 2-D SCTST-M rate constant to the TST rate constant is considerably greater for reaction (1.4) than for the other reactions considered in this study suggests the relative importance of quantum tunneling effects in this reaction. The 2-D SCTST-M and QRS rate constants converge at high T, although the Arrhenius plot of the 2-D SCTST-M rate constant exhibits more curvature than that of the QRS rate constant. The 2-D rate constant calculated with deep tunnelling corrections (SCTST-W) is 37% less than the 2-D SCTST-M rate constant at 250 K. Experimental measurements of rate constants for reaction (1.4) from two studies are

Table 3.6: Rate constants for reaction (1.4), in units cm^3 $molecule^{-1}$ s^{-1}, calculated by TST, SCTST, and QRS[a]

T(K)	TST	2-D SCTST-M	1-D SCTST-M	2-D SCTST-W	1-D SCTST-W	QRS[b]
200	1.68(−31)	5.70(−25)	1.31(−26)	2.46(−25)	8.09(−26)	1.83(−26)
250	1.11(−27)	6.78(−24)	1.25(−24)	4.94(−24)	2.49(−24)	2.12(−24)
300	4.08(−25)	9.83(−23)	4.81(−23)	8.88(−23)	6.16(−23)	8.90(−23)
350	2.88(−23)	1.31(−21)	9.55(−22)	1.27(−21)	1.05(−21)	1.74(−21)
400	7.24(−22)	1.30(−20)	1.11(−20)	1.29(−20)	1.16(−20)	1.91(−20)
450	9.20(−21)	9.33(−20)	8.56(−20)	9.29(−20)	8.76(−20)	1.36(−19)
500	7.23(−20)	5.00(−19)	4.75(−19)	4.99(−19)	4.81(−19)	7.02(−19)
600	1.71(−18)	7.34(−18)	7.17(−18)	7.35(−18)	7.23(−18)	9.30(−18)
700	1.76(−17)	5.72(−17)	5.65(−17)	5.74(−17)	5.68(−17)	6.51(−17)
800	1.07(−16)	2.92(−16)	2.89(−16)	2.92(−16)	2.91(−16)	2.99(−16)
1000	1.52(−15)	3.35(−15)	3.32(−15)	3.36(−15)	3.34(−15)	2.83(−15)
1300	2.15(−14)	4.02(−14)	3.98(−14)	4.03(−14)	4.01(−14)	2.65(−14)
1600	1.31(−13)	2.25(−13)	2.22(−13)	2.26(−13)	2.23(−13)	1.21(−13)
2000	7.23(−13)	1.17(−12)	1.15(−12)	1.18(−12)	1.16(−12)	5.11(−13)

[a]Numbers in parentheses denote powers of 10.
[b]From ref [150].

presented in Figure 3.10(b) [204, 205].

Reaction (1.4) involves the exchange of a light H atom between two heavier CH_3 species and is therefore characterised by relatively significant reaction-path curvature. This suggests that, at low collision energies, tunnelling along "corner-cutting" paths between the reactant and product channels contributes more to the reaction rate than tunnelling along the MEP because the potential barrier associated with the corner-cutting path is narrower than the MEP barrier. At a particular energy, the WKB integral associated with the corner-cutting barrier is less than that for the MEP barrier, even though the corner-cutting barrier is higher.

One possible corner-cutting path on the 2-D PES is presented in Figure 3.11(a), and the potential barrier associated with this path is presented in Figure 3.11(b). The corner-cutting barrier is considerably narrower than the MEP barrier and similar in width at lower energies to the symmetric Eckart potential used in 2-D SCTST-

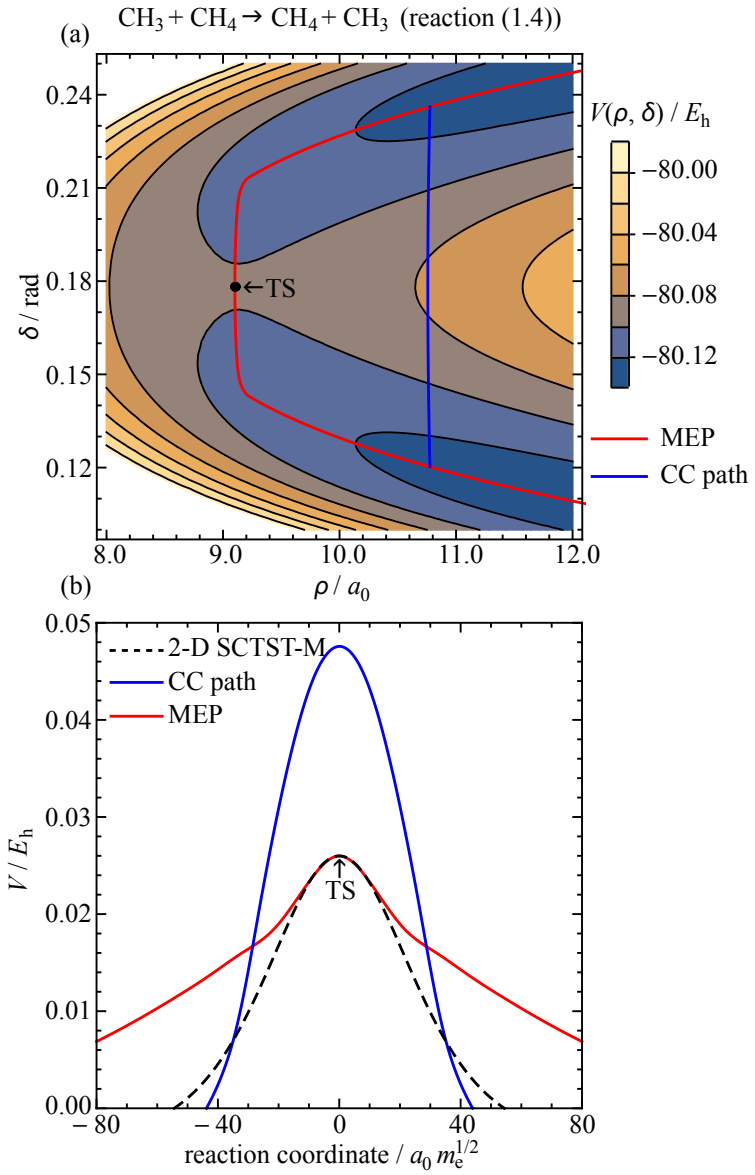


Figure 3.11: (a) Contour plot of the fitted 2-D PES in hyperspherical coordinates from ref [150]. The red curve is the minimum-energy path (MEP), and the blue line represents a possible corner-cutting (CC) path between the reactant and product channels. (b) The potentials as a function of the reaction coordinate along each of these paths, as well as the 2-D SCTST-M barrier (dashed black curve). Note that the intersection points of the CC and MEP barriers do not correspond to the intersection points of their respective paths on the PES.

M calculations. Only the x_{FF} anharmonic constant, and not the x_{1F} anharmonic constant, was used to construct this Eckart potential. Both of these anharmonic constants account for coupling between the transition and reaction modes, as they both are calculated from derivatives of the potential V along the eigenvectors of both of these modes. The fact that the Eckart potential presented in Figure 3.11(b) is narrower than the MEP barrier suggests that corner-cutting in SCTST is treated via the coupling included in the x_{FF} parameter. Corner-cutting effects in this reaction will be examined in more detail in section 3.3.3.4.

3.3.3 1-D Rate Constants

3.3.3.1 $\mathbf{H + CH_4 \longrightarrow H_2 + CH_3}$ (reaction (1.1))

Rate constants calculated by the 1-D SCTST-M method from the 2-D PES for reaction (1.1) are shown in Figure 3.12(a). These exhibit good agreement with those from the 2-D SCTST-M method from 250 K to 1000 K, differing at most by a factor of 1.93 at 250 K. In order to gain insight into the factors that give rise to the difference between these rate constants, additional calculations were performed in which some of the parameters in the 2-D SCTST calculation (x_{FF}, x_{1F}, x_{11}, and G_0) were varied individually. In each of these calculations, one of these parameters was assigned its value from the 1-D framework, and the remaining parameters were assigned their values from the 2-D framework. Varying these parameters in this way enables a systematic evaluation of which contribute most to the difference in results between the 1-D and 2-D methods. Figure 3.12(b) presents results from this analysis over a temperature range smaller than that in Figure 3.12(a).

Assigning the parameter x_{1F} its 1-D value (0) causes the rate constant to increase relative to the 2-D case (by a factor of 2.42 at 250 K). This increase can be understood by considering the symmetric Eckart potentials that correspond to these calculations,

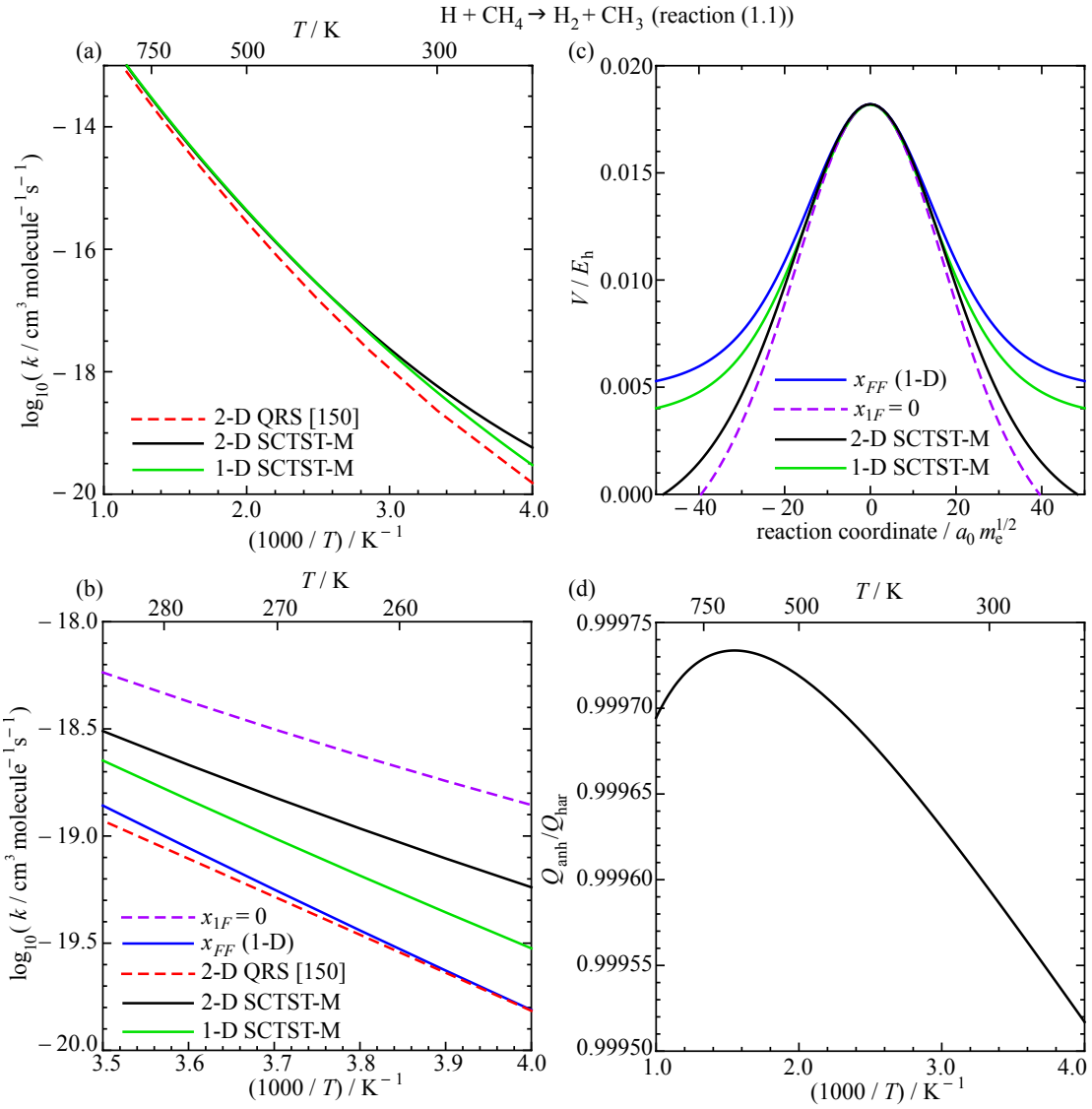


Figure 3.12: (a) Rate constants calculated for reaction (1.1) using the 2-D and 1-D SCTST-M methods (black and green curves, respectively), with QRS results (dashed red curve) [150]. (b) Rate constants calculated by setting the parameters x_{1F} (dashed purple curve) and x_{FF} (blue curve) to their 1-D values, as given in section 3.2.2. Note the different scales of the axes in this plot. (c) Symmetric Eckart potentials for $\{n\}'' = 0$ corresponding to the rate constant calculations presented in (b). (d) The ratio of the anharmonic to the harmonic partition function for the transition mode as a function of temperature.

which are presented in Figure 3.12(c) for the case in which the quantum number of the transition mode is 0. Because $\mathrm{Im}(x_{1F}) < 0$ for reaction (1.1), setting x_{1F} to zero increases the effective reaction mode frequency $\Omega_{\{n\}''}$ (equation (2.116)). The square of this parameter is proportional to the second derivative of the barrier at the TS, so increasing it causes a narrowing of the barrier. Narrowing the barrier decreases the barrier penetration integral and therefore increases the CRP and the rate constants. Only the $n = 0$ case is considered in this discussion because it contributes significantly more to the rate constant than the higher-energy $n = 1$ case due to the presence of a Boltzmann factor in equation (2.128).

In contrast, assigning the parameter x_{FF} its 1-D value causes the rate constant to decrease relative to the 2-D rate constant (by a factor of 3.74 at 250 K). The reaction barrier in this case is wider than the 2-D barrier, and its asymptotes are greater due to a lesser value of D (equations (2.107) and (2.110)). This results in less tunneling and a lower rate constant.

Assigning the parameter x_{11} its 1-D value (0) affected the rate constant negligibly, indicating that the transition mode for reaction (1.1) is not significantly anharmonic. This is illustrated in Figure 3.12(d), in which the ratio of the anharmonic partition function for the transition mode to the harmonic partition function is presented as a function of temperature. This ratio is close to 1 from 250 K to 1000 K. At 250 K, the temperature of greatest difference between these partition functions, the rate constant calculated assuming that x_{11} is 0 is 0.05% greater than the 2-D rate constant.

Assigning the parameter G_0 its 1-D value also affected the rate constant negligibly because G_0 contributes negligibly to ΔV_f. The absolute value of G_0 is 1.3% of ΔV_f in the 2-D case. The rate constant calculated by assigning G_0 its 1-D value is 3.2% greater than the 2-D rate constant at 250 K.

Only the changes in the x_{FF} and x_{1F} parameters contribute significantly to the

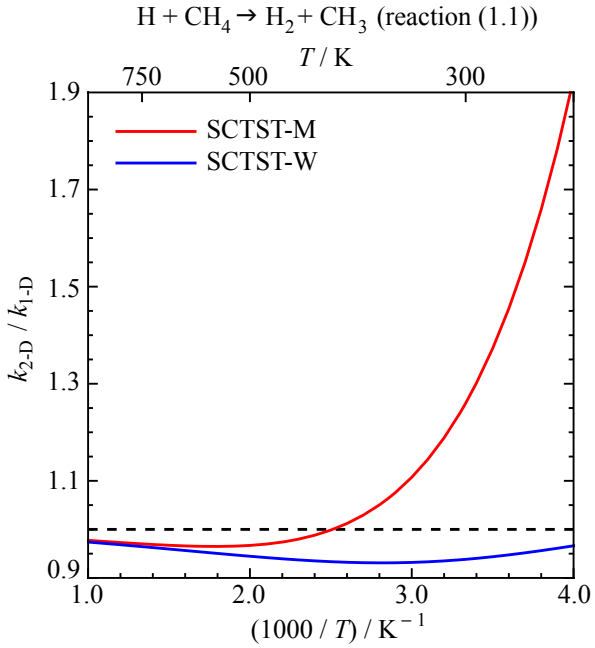


Figure 3.13: Ratios of rate constants calculated within the 2-D framework to those calculated within the 1-D framework using the SCTST-M (red curve) and SCTST-W (blue curve) methods for reaction (1.1). The horizontal dashed line denotes the value 1, at which 1-D and 2-D rate constants are equal.

difference in value between the 1-D and 2-D rate constants. The net effect of changing the x_{FF}, x_{1F}, and G_0 parameters on the barrier shape is represented as the 1-D SCTST-M barrier in Figure 3.12(c). Because assigning x_{FF} its 1-D value decreases the rate constant and setting x_{1F} to 0 increases the rate constant by approximately the same factor, and because the G_0 and x_{11} parameters do not contribute significantly to the 2-D rate constant, the 1-D and 2-D rate constants for reaction (1.1) do not differ significantly. 1-D rate constants calculated with the SCTST-M method are presented in Table 3.3 (page 59).

The SCTST-W method is even less sensitive than SCTST-M to a reduction in dimensionality from 2-D to 1-D. At 250 K, the 2-D SCTST-W rate constant is 1.02 times greater than the 1-D SCTST-W rate constant. Ratios of the 2-D to 1-D rate constants for the SCTST-M and SCTST-W methods are presented in Figure 3.13. Numerical values of rate constants calculated using the 1-D methods are also pre-

sented in Table 3.3. The insensitivity of the SCTST-W method to a reduction in dimensionality relative to the SCTST-M method will be discussed further in Section 3.3.3.4.

3.3.3.2 $\mathbf{H + C_2H_6 \longrightarrow H_2 + C_2H_5}$ (reaction (1.2))

1-D SCTST-M rate constants for reaction (1.2) also did not differ significantly from 2-D SCTST-M rate constants from 250 K to 1000 K (Figure 3.14(a)). Because $\mathrm{Im}(x_{1F}) < 0$, assigning this parameter the value 0 resulted in a narrowing of the $n = 0$ potential barrier and increased rate constants relative to the 2-D SCTST-M calculation, by a factor of 2.25 at 250 K (Figure 3.14(b) and 3.14(c)). Using the 1-D value of x_{FF} resulted in lesser rate constants, by a factor of 0.59 at 250 K. Assigning the parameter x_{11} its 1-D value increased the rate constant at 250 K by 2.1%, and using a 1-D G_0 parameter increased it by 8.2%. Applying deep tunnelling corrections in the 1-D framework did not significantly improve the accuracy of SCTST calculations (Figure 3.14(d)). Numerical values of these rate constants are presented in Table 3.4 (page 63).

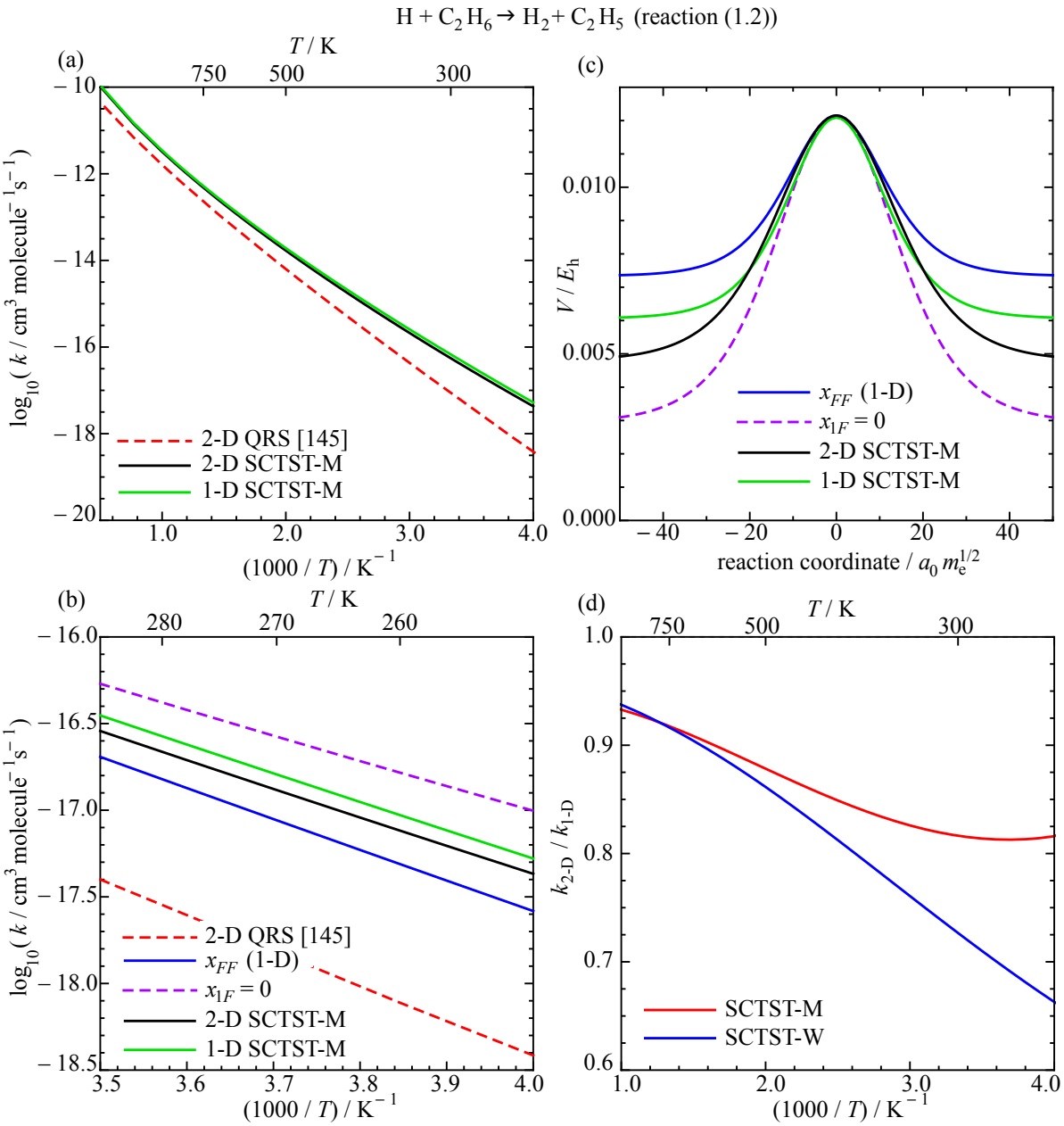


Figure 3.14: (a) Rate constants for reaction (1.2) calculated by SCTST-M in the 2-D (black curve) and 1-D (green curve) frameworks, with QRS results (dashed red curve) [145]. (b) and (c) Rate constants and potential barriers from additional 2-D SCTST-M calculations as presented in Figure 3.12. (d) Ratios of 2-D to 1-D rate constants calculated using the SCTST-M (red curve) and SCTST-W (blue curve) methods.

3.3.3.3 $\mathbf{H + cyc-C_3H_6 \longrightarrow H_2 + cyc-C_3H_5}$ (reaction (1.3))

For reaction (1.3), the 1-D and 2-D SCTST-M rate constants exhibit good agreement with each other from 250 K to 1000 K (Figure 3.15(a)). Results from the 1-D method are 1.85 times greater than those from the 2-D method at 250 K. This is because the effects on the rate constant of assigning the x_{FF} and x_{1F} parameters their 1-D values are approximately equal in magnitude but opposite in sign (Figures 3.15(b) and 3.15(c)), as in the previous two reactions. Using the 1-D values of G_0 and x_{11} resulted in discrepancies of 20% and 17%, respectively, at 250 K, relative to the 2-D calculation.

There are greater discrepancies between the 2-D and 1-D SCTST-W rate constants than for the previous two reactions (Figure 3.16(a)). The rate constant from the 1-D SCTST-W method is 2.78 times greater than that from the 2-D method at 250 K (Table 3.5, page 65). This is because the potential barrier used in the 1-D SCTST-W calculation is significantly narrower than that from the $\{n\}'' = 0$ case of the 2-D SCTST-W calculation (Figure 3.16(b)). This difference is more pronounced than in the previous reactions primarily because the magnitude of the 2-D x_{1F} parameter is considerably greater than for the other reactions. For reaction (1.3), the magnitude of this parameter is 41% of that of the reaction mode frequency calculated from the RD PES, whereas for reactions (1.1) and (1.2) it is only 9% and 21%, respectively. Thus, setting the x_{1F} parameter to 0 in the 1-D SCTST-W calculation results in more narrowing of the potential barrier and therefore greater 1-D rate constants. This effect is not observed to the same extent in the SCTST-M method because assigning the x_{FF} parameter its 1-D value increases the asymptotes of the potential barrier, resulting in less tunnelling (Figure 3.16 (c)).

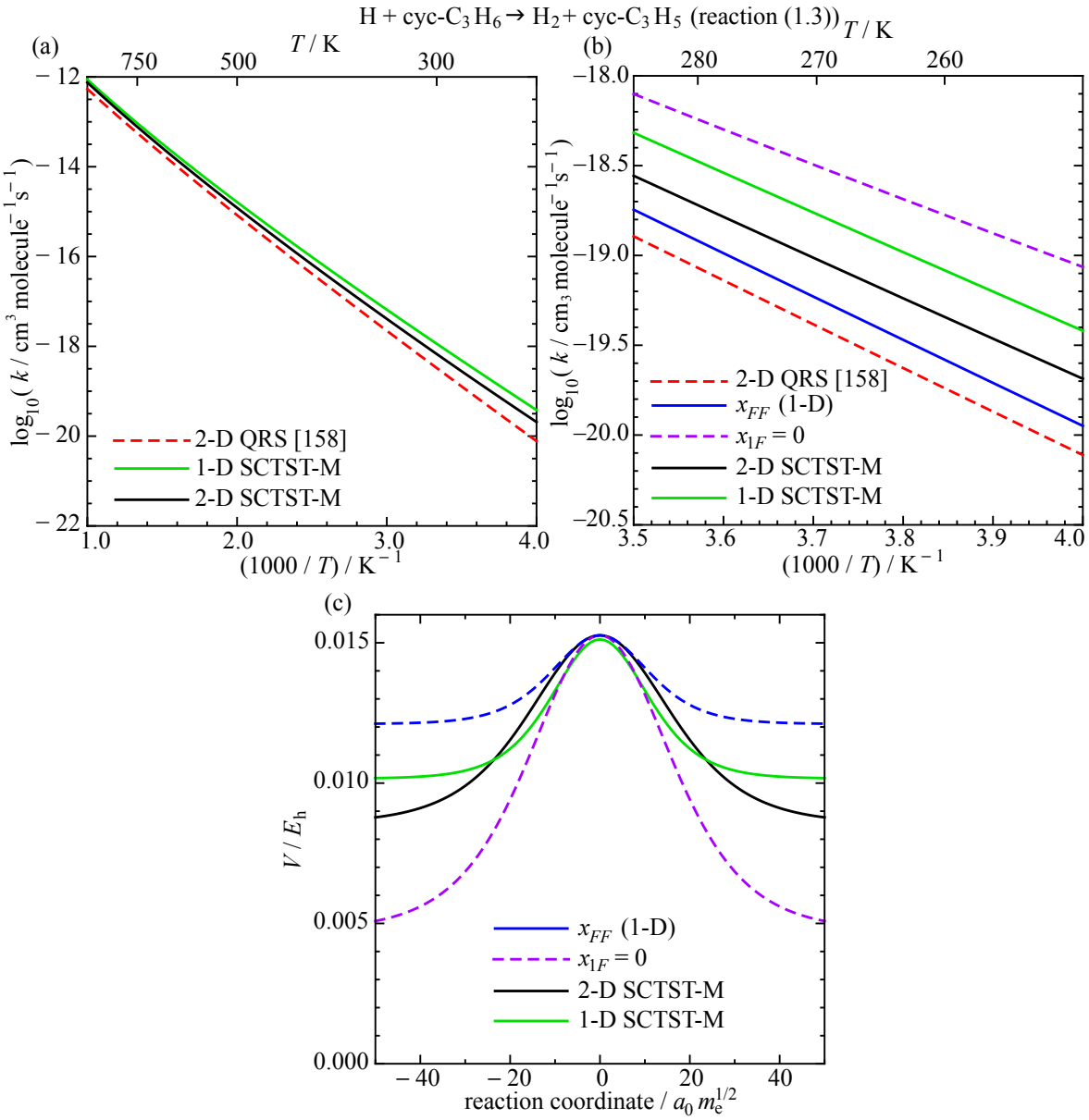


Figure 3.15: (a) 2-D (black curve) and 1-D (green curve) SCTST-M rate constants for reaction (1.3) and QRS results calculated using the same PES [158]. (b) and (c) Rate constants and potential barriers from modified SCTST-M calculations as presented in Figure 3.12.

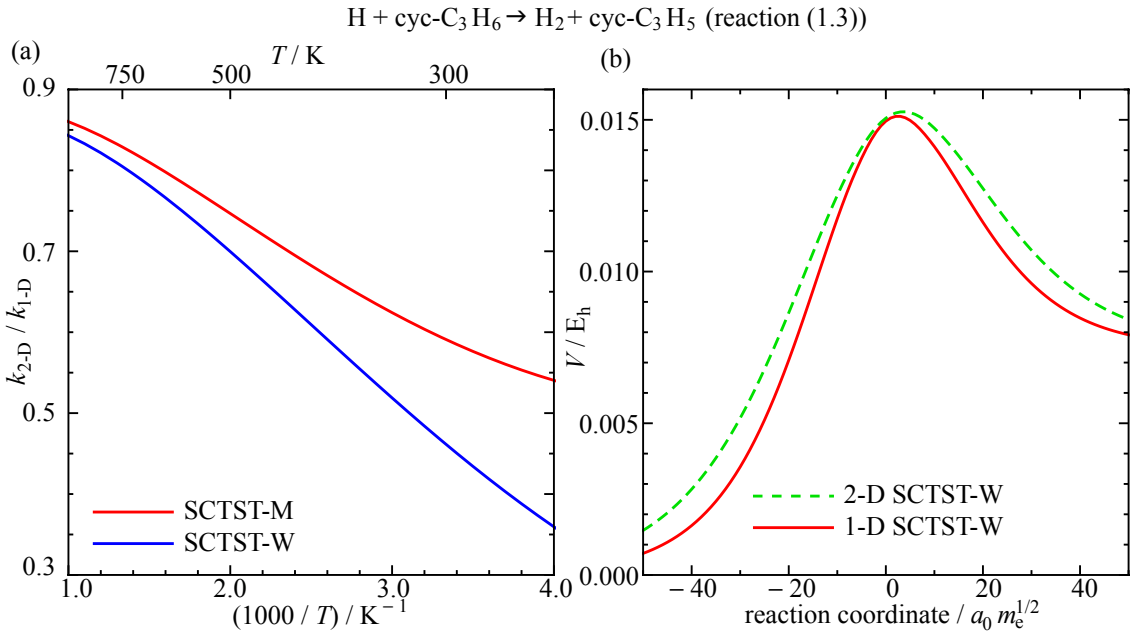


Figure 3.16: (a) Ratios of 2-D to 1-D rate constants from the SCTST-M (red curve) and SCTST-W (blue curve) methods. (b) The potential barriers corresponding to the 1-D and 2-D SCTST-W calculations (red and dashed green curves, respectively) for $\{n\}'' = 0$.

3.3.3.4 $CH_3 + CH_4 \longrightarrow CH_4 + CH_3$ (reaction (1.4))

The difference between rate constants calculated using the 2-D and 1-D SCTST-M methods is considerably greater for reaction (1.4) than for reactions (1.1)–(1.3). The 2-D rate constant is 5.42 times greater than the 1-D rate constant at 250 K. There are two factors that primarily account for this result. Firstly, the difference between the rate constant calculated assuming that $x_{1F} = 0$ and the 2-D rate constant is significantly less than in reactions (1.1)–(1.3). At 250 K, the rate constant from the $x_{1F} = 0$ calculation is 1.32 times greater than the 2-D rate constant (Figure 3.17(b)), whereas this ratio is 2.42, 2.31, and 4.29 for reactions (1.1), (1.2), and (1.3), respectively. The absolute value of the x_{1F} parameter is significantly less for reaction (1.4) than for reactions (1.1)–(1.3) (Table 3.2, page 53). Because $\mathrm{Im}(x_{1F}) < 0$ in all cases, assigning it the value 0 results in a broadening of the potential barrier.

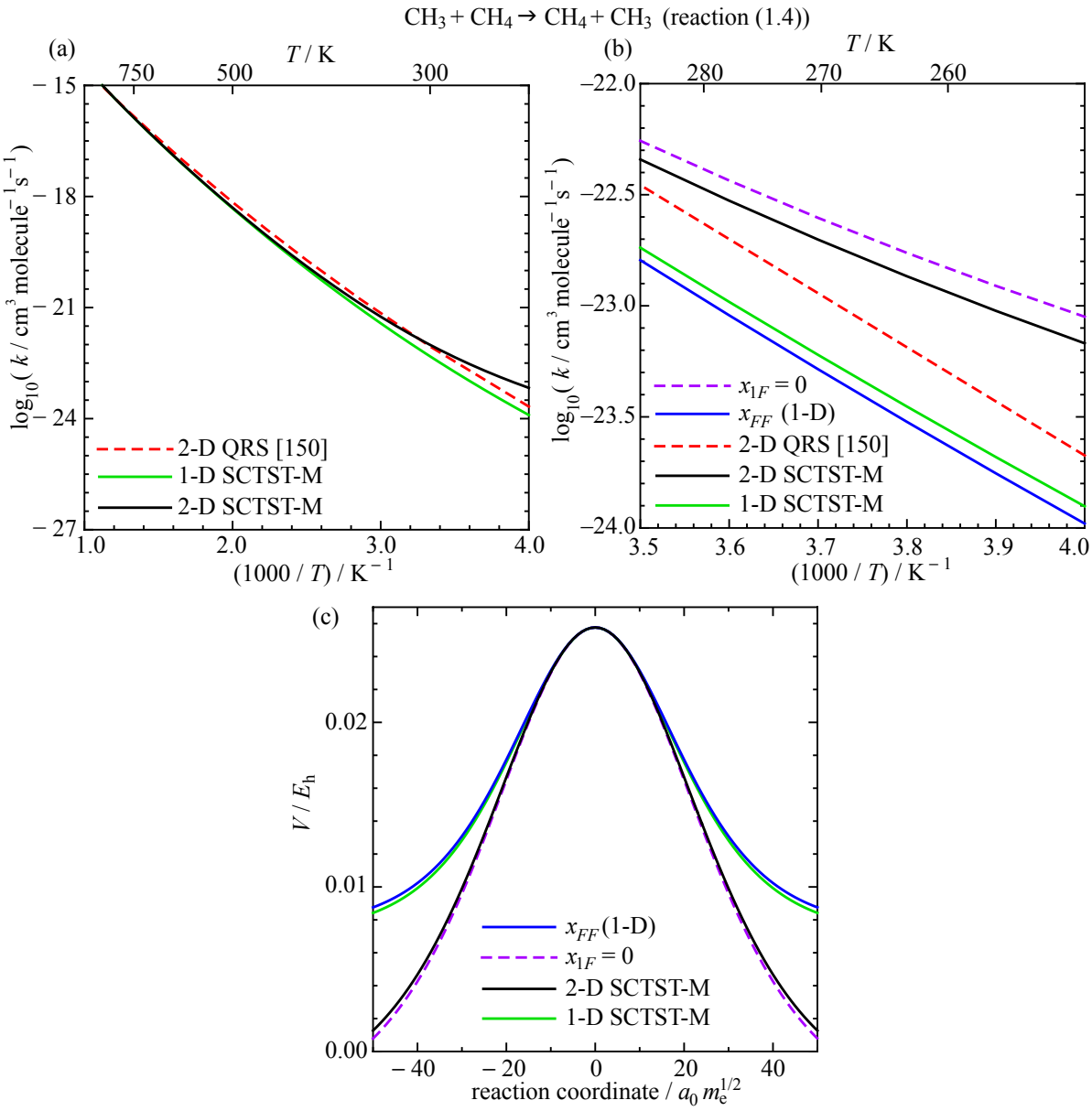


Figure 3.17: (a) Rate constants for reaction (1.4) calculated using the 2-D and 1-D SCTST-M methods (black and green curves, respectively) with QRS results (dashed red curve) [150]. (b) and (c) Rate constants and potential barriers from calculations in which parameters were individually assigned their 1-D values.

Less broadening is observed in reaction (1.4) because $\mathrm{Im}(x_{1F})$ is less negative (Figure 3.17(c)). Secondly, the ratio of the rate constant calculated using the 1-D value of x_{FF} to the 2-D rate constant is also considerably less for reaction (1.4) than for the other reactions. At 250 K, this ratio is 0.15, whereas for reactions (1.1), (1.2), and (1.3), it is 0.27, 0.61, and 0.55, respectively. This reflects the relative importance of corner-cutting in this reaction.

In order to further investigate the mechanism by which the 2-D SCTST-M method accounts for corner-cutting, additional frequency and anharmonic constant calculations were performed using the same PES. These corner-cutting effects are particularly important in determining rate constants at temperatures below T_c, which is 387 K for this reaction. Derivatives with respect to the Jacobi coordinates R and r were assumed to remain the same, but the mass of one of the CH_3 fragments was artificially assigned the mass of an H atom in order to decrease the reaction path curvature. The $\{n\}'' = 0$ potential barrier constructed using the reaction mode frequency and anharmonic constants from this "modified" calculation is shown in Figure 3.18. This barrier is broader and has greater asymptotes than the barrier from the unmodified 2-D SCTST-M calculation. An additional barrier, constructed by assigning only the x_{FF} parameter its value from the "modified" calculation, is presented as well. This barrier is also broader, which confirms that the SCTST-M method accounts for corner-cutting through the coupling term (f_{1FF}) in the x_{FF} parameter.

Differences between the 1-D and 2-D rate constants are less pronounced when the SCTST-W method is applied. The ratios of 2-D to 1-D rate constants calculated using the SCTST-M and SCTST-W methods are presented in Figure 3.19(a). At 250 K, the 2-D SCTST-W rate constant is only 1.98 times greater than the 1-D SCTST-W rate constant, whereas the 2-D SCTST-M rate constant is 5.42 times greater.

This relative insensitivity of the SCTST-W method to a reduction in dimensional-

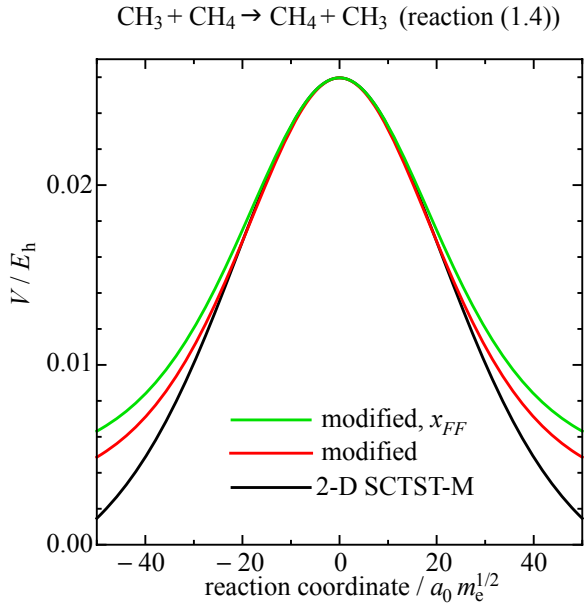


Figure 3.18: Potential barriers constructed for reaction (1.4) for the case in which $\{n\}'' = 0$. The black curve represents the barrier from the 2-D SCTST-M calculation, and the red curve represents the barrier calculated assuming the mass of one of the CH_3 fragments is m_H. In constructing the "modified, x_{FF} " barrier (green curve), only the x_{FF} parameter was assigned its value from this modified calculation.

ity can be understood by considering the potential barriers used in these calculations, which are presented in Figure 3.19(b) for $\{n\}'' = 0$. The value of the 1-D SCTST-W potential is slightly greater than that of the 2-D potential over the range of the reaction coordinate shown, but only by at most 0.0011 E_h. In contrast, the difference between the 1-D and 2-D SCTST-M barriers for reaction (1.4) is significantly greater (Figure 3.17(c)), tending to 0.011 E_h at the reactant and product asymptotes (equation (2.110)). Greater asymptotes result in less tunneling and therefore lower rate constants. Applying the SCTST-W method ensures that the barriers' asymptotes tend to physically realistic values, thereby eliminating the unrealistic differences between the asymptotes of the 1-D and 2-D barriers observed in the SCTST-M method. The SCTST-W method is therefore less sensitive to changes in the x_{FF} and x_{1F} parameters associated with reducing the dimensionality of the calculation from 2-D to 1-D, which suggests that it is less sensitive to the coupling terms in these parame-

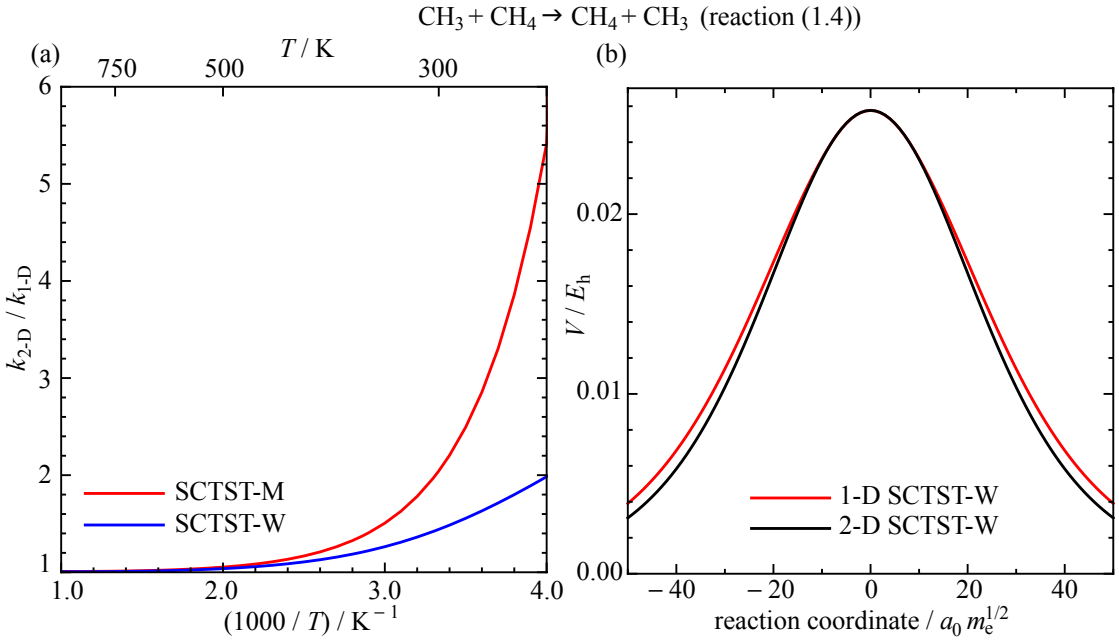


Figure 3.19: (a) Ratios of 2-D rate constants to 1-D rate constants for reaction (1.4) calculated using the SCTST-M (red curve) and SCTST-W (blue curve) methods. (b) The potential barriers associated with the $\{n\}'' = 0$ case in SCTST-W calculations for reaction (1.4). The red curve represents the barrier for the 1-D method, and the black curve for the 2-D method.

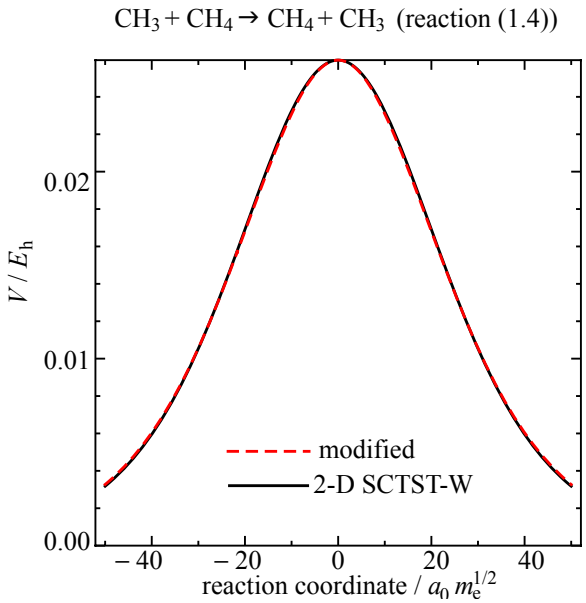


Figure 3.20: The potential barrier from the 2-D SCTST-W calculation (black curve) and an analogous barrier from the "modified" calculation (dashed red curve).

ters. This is further reflected in the 2-D SCTST-W potential barrier associated with the "modified" calculation above, which does not differ significantly from its counterpart from the unmodified calculation (Figure 3.20). This suggests that coupling does not play as important a role in determining rate constants when deep tunnelling corrections are applied.

3.4 Conclusions

This chapter discusses the application of the 1-D and 2-D SCTST methods to calculate rate constants from 2-D PESs previously developed for QRS calculations. These calculations serve as benchmarks for comparison because they explicitly account for the quantum mechanical effects that SCTST recovers in an approximate manner. Rate constants and CRPs from SCTST calculations were compared to those from QRS calculations. The PESs considered in this chapter were defined in terms of the Jacobi coordinates of the system and also include the ZPE of the system's spectator modes. Two methods were presented for calculating the frequencies and anharmonic constants needed for SCTST calculations from these PESs. Both methods yielded equivalent results, which therefore suggests the validity of these approaches. The effects of deep tunnelling corrections on rate constants were also evaluated in the 1-D and 2-D frameworks.

The frequencies calculated from the PESs exhibited an acceptable level of agreement with those from *ab initio* calculations. 2-D rate constants calculated without deep tunnelling corrections agreed closely with those from QRS calculations, except for the $H + C_2H_6$ reaction. Discrepancies in this case highlight differences between the two methods in their sensitivity to different regions of the PES. It is particularly notable that the SCTST method performed well for the $CH_3 + CH_4$ reaction, as corner-cutting effects likely contribute significantly to the rate of this reaction.

The coupling between vibrational modes that facilitates corner-cutting is included in SCTST through the cross-derivatives used to calculate the anharmonic constants of the reaction mode.

For the $H + CH_4$, $H + C_2H_6$, and $H + cyc-C_3H_6$ reactions, 1-D rate constants calculated without deep tunnelling corrections deviated little from 2-D results primarily due to two opposing effects approximately equal in magnitude. Assigning the anharmonic constants x_{1F} and x_{FF} their 1-D values resulted in increased and decreased rate constants, respectively, relative to the 2-D case. For the $CH_3 + CH_4$ reaction, assigning x_{1F} its 1-D value did not increase rate constants to the same extent as for the other reactions, so 1-D rate constants for this reaction were considerably less than 2-D rate constants. Applying deep tunnelling corrections rectifies this issue because it imposes more realistic behaviour of the reactant and product asymptotes of the reaction's potential barrier. In all other 1-D and 2-D calculations, applying deep tunnelling corrections did not significantly change the calculated rate constants.

These findings provide evidence that SCTST can yield good estimates of reaction rate constants in a RD framework and that deep tunnelling corrections should always be applied, as they (1) impose more physically realistic behaviour of the system, (2) yield results of comparable or better accuracy to those from calculations without these corrections, and (3) do not significantly increase the computational cost of calculations. Despite the computational advantages of SCTST over QRS, calculating rate constants from first principles as described in this chapter requires significant computational expense due to the cost of constructing the RD PES. The primary advantage of SCTST methods is that they do not require a full PES, as do QRS methods. This suggests an investigation of an *ab initio* approach to rate constant calculations using a minimal number of PES calculations, which is the focus of the next chapter.

Chapter 4

SCTST Rate Constants from *Ab Initio* Calculations

4.1 Introduction

This chapter focuses on the calculation of rate constants by FD and 1-D SCTST directly from *ab initio* calculations, without using PESs constructed previously. A primary challenge associated with these calculations is obtaining sufficiently accurate third and fourth PES derivatives (i.e., a quartic force field) for anharmonic constants from electronic structure theory. A common approach to calculating these derivatives involves transforming the mass-weighted Hessian matrix into normal coordinate space and differentiating the elements of the resulting matrix numerically [116, 118, 119]. This approach has been applied previously in the contexts of vibrational spectrum calculations and SCTST calculations [116–119, 122, 123, 180, 206]. In these previous studies, Hessian matrices were constructed either from analytical second PES derivatives or by finite differentiation of analytical first derivatives.

Analytical derivatives are implemented at several different levels of theory in many electronic structure software packages [171, 172, 207–209]. However, methods for calculating analytical derivatives for open-shell systems are not as widely implemented as for closed-shell systems [210–212]. For example, they are not implemented at the UMP2 level of theory in MOLPRO [172]. Many of the elementary gas-phase chemical

reactions studied previously using accurate QRS methods have open-shell transition state structures [2, 37, 49–51, 60], including the four reactions considered in this thesis.

In this chapter, a fully numerical approach to calculating third and fourth derivatives that does not require analytical first or second derivatives is presented. Richardson extrapolation [213] is used to improve the accuracy of these derivatives. An advantage of this approach is that it is available to users of all electronic structure packages at all levels of theory. In some cases, calculations of analytical second derivatives are computationally more expensive than numerical calculations, so this approach may offer advantages in efficiency in those cases [214, 215]. Fully numerical calculations are also more conducive to parallelisation [215], an advantage that becomes more important as the system size increases. Numerical differentiation is required for SCTST calculations even when analytical first or second derivatives are available [122, 123], and the approach discussed here enables systematic improvement of the accuracy of these numerical derivatives. Their accuracy can be adjusted according to what is required for the system being investigated.

The primary objective of this chapter is to evaluate whether good estimates of rate constants can be obtained using 1-D SCTST, as judged by comparison with results from FD SCTST, and to compare the computational costs of these methods. This chapter presents practical procedures for calculating rate constants in each of these frameworks. More rigorous treatments that involve greater computational expense are possible for the systems considered, but the aim is to develop a method that can be applied to larger systems.

Details of *ab initio* calculations are first presented, followed by a description of the quartic force field calculations. Rate constants calculated by SCTST for the H + CH_4 and H + C_2H_6 (reactions (1.1) and (1.2)) are then presented and compared to

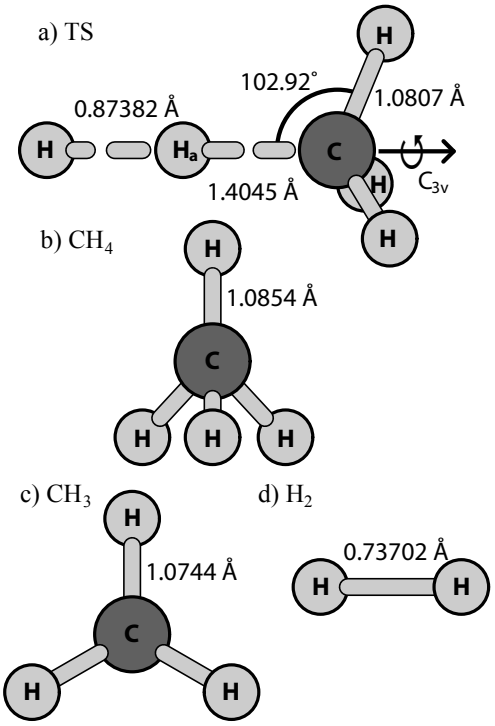


Figure 4.1: Optimised structures of the stationary points for reaction (1.1), i.e., (a) the TS, (b) CH_4, (c) CH_3, and (d) H_2, calculated at the MP2/cc-pVTZ level of theory. Bond lengths are reported in Åand bond angles in degrees. In (a), the H atom being abstracted from CH_4 is denoted as H_a.

results from previous theoretical and experimental studies. Finally, the computational efficiency and accuracy of the 1-D method is evaluated in relation to the FD method.

4.2 Methods

4.2.1 *Ab Initio* Calculations

All quantum chemistry calculations were performed using the MOLPRO software package [172]. The geometries of the stationary points on the PES were calculated at the MP2/cc-pVTZ level of theory [190]. A tight geometry optimization condition (maximum gradient component less than 5×10^{-8} E_h a_0^{-1}) was used to calculate the TS geometries, as suggested by Barone [116] for the purpose of anharmonic constant calculations. No symmetry constraints were applied in geometry optimisation calcu-

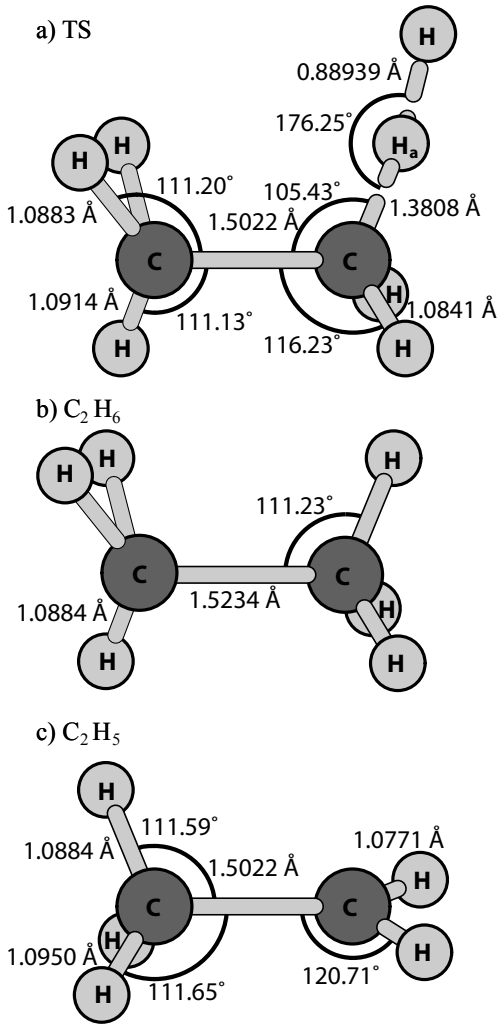


Figure 4.2: Optimised structures of the stationary points for reaction (1.2), i.e., (a) the TS, (b) C_2H_6, and (c) C_2H_5 presented as in Figure 4.1.

lations in order to ensure that no species had strictly degenerate frequencies. Barone suggested that degeneracy be broken in order to allow the use of formulas for asymmetric tops in anharmonic constant calculations, which greatly simplifies SCTST calculations [116]. Recent SCTST studies [122, 123] employed the MultiWell Program Suite [216, 217] to perform calculations, which only includes formulas for asymmetric tops, suggesting that degeneracy was broken in these studies as well.

Geometries of the stationary points of reaction (1.1) are presented in Figure 4.1. The C–H and C–H_a bond lengths of the TS differ from those calculated in previous

Table 4.1: Single-point CCSD(T)/aug-cc-pVTZ energies of the stationary points of reactions (1.1) and (1.2), and the associated forward and reverse barrier heights and reaction enthalpies.

Molecular energies (E_h)		
	R = CH_3	R = C_2H_5
RH	−40.441	−79.680
H	−0.500	−0.500
TS	−40.914	−80.161
R	−39.764	−79.008
H_2	−1.172	−1.172
Reaction energetics (kcal mol^{-1})[a]		
	Reaction (1.1)	Reaction (1.2)
ΔV_f	14.710	11.859
ΔV_r	11.703	12.183
$\Delta_r H$	3.007	−0.325

[a]Zero-point energies are not included in these quantities.

theoretical studies [27, 53] by $< 1\%$. The H−H_a bond is approximately 2% shorter than those reported in these studies. Geometries of the reactants and products exhibit a similar level of agreement. Geometries for reaction (1.2) are presented in Figure 4.2. The H−H_a bond in the TS is 3% longer than that calculated previously [145], and the C−H_a bond is 3% shorter. The remaining bond lengths and angles of the TS and other stationary points exhibit closer agreement.

Single-point energies of the stationary points at these geometries were obtained at the CCSD(T) level of theory with the cc-pVTZ basis set augmented with diffuse s, p, d, and f orbitals (aug-cc-pVTZ) [218]. These results, as well as the reaction barrier heights, are presented in Table 4.1. The nonadiabatic forward barrier height of reaction (1.1) is 0.439 kcal mol^{-1} greater and 0.6 kcal mol^{-1} less than those calculated at the CCSD(T)/cc-pVTZ level of theory in refs [150] and [154], respectively. The forward barrier height of reaction (1.2) is 0.1 kcal mol^{-1} less than that reported in ref. [154], which was calculated at the CCSD(T)-F12a/cc-pVTZ-F12a level of theory.

Hessian matrices, which were used to calculate anharmonic constants and vibrational partition functions, were calculated at the MP2/cc-pVTZ level of theory. All Hessian elements were calculated from central differences of the energy, using the NUMERICAL option in MOLPRO. Richardson extrapolation was used to improve the accuracy of Hessian elements for the TS, as described in the following section. This involves calculating the numerical Hessian using multiple step sizes by changing the STEP parameter in MOLPRO.

4.2.2 Numerical Differentiation by Richardson Extrapolation

In general terms, Richardson extrapolation is a method for accelerating convergence in a calculation of the value of an infinite series [219]. Ridders [213] adapted this technique to the calculation of the derivatives of a function [220]. Calculations of a numerical derivative at larger step sizes are used to remove the contribution of higher-order derivatives to the error in a calculation at a smaller step size. A summary of this method is presented below.

Consider a Taylor expansion of the function f about a point x, evaluated at $(x+h)$:

$$f(x+h) = f(x) + f'(x)h + \sum_{n=2}^{\infty} \frac{1}{n!} f^{(n)}(x) h^n, \tag{4.1}$$

and at $(x-h)$:

$$f(x-h) = f(x) - f'(x)h + \sum_{n=2}^{\infty} \frac{(-1)^n}{n!} f^{(n)}(x) h^n, \tag{4.2}$$

where $f^{(n)}(x)$ denotes the n^{th} derivative of f evaluated at x. The expression resulting from subtracting equation (4.2) from equation (4.1) and dividing by $2h$ is defined as $A(h)$, the zeroth-order extrapolation of the numerical derivative of $f(x)$ calculated using a step size of h. This expression is given as follows:

$$A(h) \equiv \frac{f(x+h) - f(x-h)}{2h} = f'(x) + \sum_{n=1}^{\infty} \frac{1}{(2n+1)!} f^{(2n+1)}(x) h^{2n}. \tag{4.3}$$

Only odd-numbered derivatives of f are included in the sum because terms involving even derivatives cancel when equation (4.2) is subtracted from equation (4.1). The sum in the right-hand side of this expression comprises the error in this estimate of the derivative. These error terms are proportional to only even powers of h.

Next considering calculations of this derivative with a different step size, $A(ch)$, where $c > 1$, gives:

$$A(ch) = \frac{f(x+ch) - f(x-ch)}{2ch} = f'(x) + \sum_{n=1}^{\infty} \frac{1}{(2n+1)!} f^{(2n+1)}(x) c^{2n} h^{2n}. \tag{4.4}$$

Both $A(h)$ and $A(ch)$ represent the exact value of the first derivative, $f'(x)$, plus an infinite sum of error terms. They can be combined as follows:

$$\frac{c^2 A(h) - A(ch)}{c^2 - 1} = f'(x) + \sum_{n=1}^{\infty} \frac{1}{(2n+1)!} f^{(2n+1)}(x) \frac{c^2 - c^{2n}}{c^2 - 1} h^{2n}. \tag{4.5}$$

When $n = 1$, the first term in the above sum is 0. Thus, this expression can be rewritten:

$$\frac{c^2 A(h) - A(ch)}{c^2 - 1} = f'(x) + \sum_{n=2}^{\infty} \frac{1}{(2n+1)!} f^{(2n+1)}(x) \frac{c^2 - c^{2n}}{c^2 - 1} h^{2n}. \tag{4.6}$$

In situations in which this formulation is useful, successively higher-order terms in the Taylor expansion constitute lesser contributions to $f(x)$. The left-hand side of the above expression will be referred to as a first-order extrapolation of $f'(x)$. Because it does not include the $f^{(3)}(x)$ term from the Taylor expansion, it is an estimate of $f'(x)$ with a lesser error than the zeroth-order extrapolation (equation (4.3)).

The key feature of equation (4.3) that enables the construction of an expression for $f'(x)$ with fewer error terms is the dependence of the error terms on even powers of h. Equation (4.6) also depends only on even powers of h, so the above technique can be applied again to further reduce the error. Defining equation (4.6) as $B(h)$, it can be shown that:

$$\frac{c^4 B(h) - B(ch)}{c^4 - 1} = f'(x) + \sum_{n=3}^{\infty} \frac{1}{(2n+1)!} f^{(2n+1)}(x) \frac{c^2 - c^{2n}}{c^2 - 1} \frac{c^4 - c^{2n}}{c^4 - 1} h^{2n}, \tag{4.7}$$

where the error is further reduced because the above sum does not include the $f^{(5)}(x)$ term. Substituting the definition of $B(h)$ and simplifying gives:

$$\frac{c^4 B(h) - B(ch)}{c^4 - 1} = \frac{c^6 A(h) - (c^2 + c^4)A(ch) + A(c^2 h)}{(c^2 - 1)^2 (c^2 + 1)}. \tag{4.8}$$

This is a second-order extrapolation of $f'(x)$, and evaluating it involves calculating numerical derivatives at three different step sizes. In theory, the above approach can be applied arbitrarily many times, with successively larger step sizes $c^n h$, with n a positive integer, to reduce the error in a numerical calculation of $f'(x)$.

Richardson extrapolation can also be used to improve estimates of second derivatives. Adding equations (4.1) and (4.2), subtracting $2f(x)$, and dividing the resulting equation by h^2 yields:

$$\frac{f(x+h) - 2f(x) + f(x-h)}{h^2} = f''(x) + \sum_{n=1}^{\infty} \frac{2}{(2n+2)!} f^{(2n+2)}(x) h^{2n}. \tag{4.9}$$

Because the error terms are proportional to even powers of h, successively better approximations of $f''(x)$ can be obtained from numerical calculations of $f''(x)$ with step sizes $c^n h$, as above. Expressions for the first- and second-order extrapolations of the derivative are identical to those given above, except that $A(h)$ is defined as $f''(x)$ calculated numerically with a step size of h.

Furthermore, this technique can be applied to calculate mixed second partial derivatives numerically. Briefly, the function $f(x, y)$ is expanded in four Taylor series at $f(x \pm h, y \pm h)$. These expressions are combined to give:

$$\frac{f(x+h, y+h) - f(x+h, y-h) - f(x-h, y+h) + f(x-h, y-h)}{4h^2} =$$
$$f_{xy}(x, y) + \sum_{n_x=2}^{\infty} \sum_{n_y=2}^{\infty} \frac{1}{n_x! n_y!} \left(\frac{\partial^{(n_x+n_y)} f}{\partial x^{n_x} \partial y^{n_y}} \right) h^{n_x+n_y} [1 - (-1)^{n_x} - (-1)^{n_y} + (-1)^{n_x+n_y}], \tag{4.10}$$

which again is the numerical expression for the mixed second partial derivative of f with respect to x and y, here denoted $f_{xy}(x, y)$, plus a sum of error terms. The error

terms are nonzero only when both n_x and n_y are odd, in which case the quantity $(n_x + n_y)$ is even, so all error terms are proportional to even powers of h. The analysis discussed above can therefore be applied here, yielding analogous expressions for higher-order extrapolations of the derivative. It can be shown through similar analysis that the error terms in expressions for numerical third and fourth derivatives are also proportional to even powers of h.

4.2.3 Force Constants

Calculating the third and fourth derivatives of the PES along normal modes is accomplished straightforwardly by differentiating Hessian matrix elements [116, 119, 221]. First, $\mathbf{H}(0)$ is defined as the mass-weighted Hessian matrix (equation (2.11)) evaluated at the stationary point of the PES (i.e., the minimum for a molecule and the saddle point for a TS). Diagonalising it yields a matrix of eigenvectors, $\mathbf{L}$. The matrix $\mathbf{\Phi}(0)$ is defined as follows:

$$\mathbf{\Phi}(0) = \mathbf{L}^{\mathrm{T}}\mathbf{H}(0)\mathbf{L}, \tag{4.11}$$

such that its elements are directional derivatives of the PES along normal mode eigenvectors:

$$\phi_{ij}(0) = \frac{\partial^2 V}{\partial Q_i \partial Q_j}. \tag{4.12}$$

By definition, $\mathbf{\Phi}(0)$ is diagonal, and its elements are proportional to the squares of the system's harmonic frequencies. These elements can be differentiated to obtain third and fourth directional derivatives of the potential at the stationary point. Third derivatives, f_{ijk}, are calculated as follows:

$$f_{ijk} = \frac{\partial^3 V}{\partial Q_i \partial Q_j \partial Q_k} = \frac{1}{3}\left(\frac{\partial \phi_{jk}(0)}{\partial Q_i} + \frac{\partial \phi_{ki}(0)}{\partial Q_j} + \frac{\partial \phi_{ij}(0)}{\partial Q_k}\right). \tag{4.13}$$

Note that f_{ijk} can be obtained by differentiating three different matrix elements, and the above formula reflects an average of those three derivatives. Only fourth

derivatives of the form f_{iijj} are needed for anharmonic constant calculations (section 2.3). These are calculated as follows:

$$f_{iijj} = \frac{1}{2}\left(\frac{\partial^2\phi_{ii}(0)}{\partial Q_j^2} + \frac{\partial^2\phi_{jj}(0)}{\partial Q_i^2}\right). \tag{4.14}$$

In principle, these derivatives could also be obtained by differentiating the matrix element $\phi_{ij}(0)$ along Q_i and Q_j. However, as will be made apparent below, adding these terms in the calculation of these derivatives would greatly increase the number of Hessian matrix calculations required for the implementation presented in this study.

Calculating these derivatives numerically involves obtaining the Hessian matrix $\mathbf{H}(\pm\Delta Q_i)$ at positive and negative displacements $\pm\Delta Q_i$ away from the stationary point along each respective eigenvector. If $\mathbf{x}(0)$ represents the vector of atomic coordinates at the stationary point, then $\mathbf{x}(\pm\Delta Q_i)$, the coordinates at the displaced geometry, is calculated as follows:

$$\mathbf{x}(\pm\Delta Q_i) = \mathbf{x}(0) \pm \Delta Q_i \mathbf{M}\mathbf{L}_i, \tag{4.15}$$

where $\mathbf{L}_i$ denotes the i^{th} eigenvector. The matrix $\mathbf{\Phi}(\pm\Delta Q_i)$ is thus defined at these displaced geometries:

$$\mathbf{\Phi}(\pm\Delta Q_i) = \mathbf{L}^{\mathrm{T}}\mathbf{H}(\pm\Delta Q_i)\mathbf{L}. \tag{4.16}$$

$\mathbf{\Phi}(\pm\Delta Q_i)$ is not necessarily diagonal because the matrix of eigenvectors $\mathbf{L}$ diagonalizes the mass-weighted Hessian matrix at the stationary point, and not at the displaced geometries. The derivatives f_{ijk} can then be calculated numerically as follows [116]:

$$f_{ijk} = \frac{1}{3}\left(\frac{\phi_{jk}(\Delta Q_i) - \phi_{jk}(-\Delta Q_i)}{2\Delta Q_i} + \frac{\phi_{ki}(\Delta Q_j) - \phi_{ki}(-\Delta Q_j)}{2\Delta Q_j} + \frac{\phi_{ij}(\Delta Q_k) - \phi_{ij}(-\Delta Q_k)}{2\Delta Q_k}\right). \tag{4.17}$$

f_{iijj} is calculated similarly:

$$f_{iijj} = \frac{1}{2}\left(\frac{\phi_{ii}(\Delta Q_j) + \phi_{ii}(-\Delta Q_j) - 2\phi_{ii}(0)}{\Delta Q_j^2} + \frac{\phi_{jj}(\Delta Q_i) + \phi_{jj}(-\Delta Q_i) - 2\phi_{jj}(0)}{\Delta Q_i^2}\right). \tag{4.18}$$

Equations (4.17) and (4.18) comprise numerical derivatives of elements of $\mathbf{\Phi}$; elements of the Hessian matrices used to calculate $\mathbf{\Phi}$ are also calculated numerically. Thus, Richardson extrapolation can be applied in two independent ways to calculations of the potential derivatives f_{ijk} and f_{iijj}. Calculations can be performed with higher-order extrapolations of Hessian elements and zeroth-order extrapolations of derivatives of elements of $\mathbf{\Phi}$, or vice-versa, or higher-order extrapolations of both.

Displacements along normal mode eigenvectors are given in this chapter in dimensionless reduced normal coordinates. A displacement ΔQ_i in units of (length mass$^{1/2}$) is calculated from a displacement Δq in reduced normal coordinates as follows [116, 222, 223]:

$$\Delta Q_i = \frac{\hbar^{1/2}}{\omega_i^{1/2}} \Delta q, \tag{4.19}$$

where ω_i is the frequency of the i^{th} normal mode. In this chapter, Richardson extrapolation is applied to both Hessian elements and to the potential derivatives f_{ijk} and f_{iijj} for the TSs of reactions (1.1) and (1.2). Richardson extrapolation is not applied to the calculation of anharmonic constants for the reactants CH_4 and C_2H_6, as those calculated with Richardson extrapolation were not found to differ significantly from those calculated without it. A single displacement of $\Delta q = 0.4$ was used for the reactants.

The anharmonic constants and G_0 parameters for all species are calculated according to equations (2.64), (2.66), and (2.68). None of the frequencies of the species considered were strictly degenerate because symmetry constraints were not applied when calculating their structures by *ab initio* methods. All frequencies differed by at least 0.1 cm^{-1}. This enables the application of these formulas for the anharmonic constants of an asymmetric top to CH_4, C_2H_6, and the TS of reaction (1.1). Fermi resonances are also deperturbed as described in section 2.3.

4.2.4 Coriolis Coupling

Due to the number of vibrational DOFs treated in FD calculations for the reactions in this chapter, Coriolis coupling was included in the VPT2 treatment of their energy levels. This involves including the following term in the system's vibrational Hamiltonian (equation (2.17)) [116]:

$$\sum_{\alpha} B_{\alpha} \left[\sum_{i=1}^{F} \sum_{j=1}^{i-1} \zeta_{ij}^{\alpha} (q_i \frac{\partial}{\partial q_j} - q_j \frac{\partial}{\partial q_i}) \right]^2 , \tag{4.20}$$

where B_α is the rotational constant for axis α, calculated from the respective moment of inertia at the equilibrium geometry. ζ_{ij}^{α} is a Coriolis coupling constant, calculated as follows [224]:

$$\zeta_{ij}^{\alpha} = \sum_{a} (\mathbf{L}_{ia} \times \mathbf{L}_{ja}) \cdot \mathbf{e}_{\alpha}, \tag{4.21}$$

where $\mathbf{L}_{ia}$ denotes a vector of the elements of eigenvector $\mathbf{L}_i$ corresponding to the Cartesian coordinates of atom a, and $\mathbf{e}_\alpha$ is a unit vector along the rotational axis α. In this treatment, the following term is added to the expression for the off-diagonal anharmonic constants x_{ik} [120]:

$$B_{\alpha} (\zeta_{ik}^{\alpha})^2 \left(\frac{\omega_i}{\omega_k} + \frac{\omega_k}{\omega_i} \right). \tag{4.22}$$

4.2.5 Density of States

Calculating the anharmonic partition function for a system of coupled harmonic oscillators with energy levels specified by a VPT2 energy expression and calculating the CRP for an SCTST calculation both involve enumerating over configurations $\{n\}$ of F quantum numbers (section 2.5).[1] This is very computationally demanding for systems with more than 3 or 4 atoms [126]. To improve the efficiency of this calculation for larger systems, Nguyen and Barker [126] adapted a random walk algorithm in

[1] $F-1$ quantum numbers in the case of a FD SCTST calculation. For clarity in the discussion that follows, F will be used to denote the number of DOFs considered.

energy space developed originally by Wang and Landau [225, 226] and later modified by Basire *et al.* [227].

This algorithm involves first calculating the un-normalized density of states, $G(E)$, as a function of energy. The energy range from the anharmonic ZPE to $E_{\max}$ is partitioned into a number of bins (N_{bins}), and the density in each bin, $G(E_i)$, is initially assigned the value 1. The quantum numbers $\{n\}$ are initialised at random, subject to the constraints discussed in section 2.4. A number of iterations are performed, and within each iteration a number N_{trial} of trials are performed. In each trial, each of the quantum numbers in $\{n\}$ is either incremented, decremented, or left unchanged, according to the value of a random number, ranging from 0 to 1, generated for each DOF, R_j. If $R_j \leq p$, where $p = \min(F^{-1}, 0.25)$, then n_j is decremented, unless it is already 0. If $p < R_j \leq 2p$, then n_j is incremented. If $2p < R_j$, then n_j is left unchanged.

The energy E_{new} of this new configuration of quantum numbers is computed. E_{old} is defined as the energy of the old configuration. If the ratio $G(E_{\text{old}})/G(E_{\text{new}})$ is greater than another random number, the step is accepted, and the next trial begins with this new configuration. Otherwise, $\{n\}$ is reverted to the old configuration, and the next trial begins. In either case, the density at the energy of the current configuration is increased by a factor f, where:

$$\ln f = 2^{1-k}, \tag{4.23}$$

and k is the index of the current iteration, which increases from 1 to N_{iter} over the course of the calculation.

The normalised density of states in each bin, $\rho(E_i)$, is then calculated as follows:

$$\rho(E_i) = \frac{G(E_i)}{G(E_0)\Delta E}, \tag{4.24}$$

where $G(E_0)$ is the un-normalized density in the lowest-energy bin, at the anharmonic ZPE of the system. Using this formula to calculate $\rho(E_i)$ requires that the size ΔE of the energy bins is chosen such that only the ground-state configuration is in the lowest-energy bin [126]. A value of 0.0001 E_h = 21.9 cm^{-1} was used for ΔE, and values of 22 and 10^7 were used for the N_iter and N_trial parameters. The effect of the choice of these parameters on calculated rate constants will be discussed further in section 4.3.2.3. The partition function Q_anh is calculated from the density of states as follows:

$$Q_\mathrm{anh}(T) = \sum_{i=1}^{N_\mathrm{bins}} \rho(E_i)\Delta E \exp\left(-E_i k_\mathrm{B}^{-1} T^{-1}\right) \tag{4.25}$$

The energy in the non-reactive modes of the TS, $E_{\{n\}'}$, and the effective reaction mode frequency, $\Omega_{\{n\}'}$, are needed to calculate the CRP for a FD calculation (section 2.4). In order to calculate the CRP from the density of states, average values of these parameters for each energy bin are needed. These are calculated by averaging the values of $E_{\{n\}'}$ and $\Omega_{\{n\}'}$ calculated for all configurations of $\{n\}'$ sampled within each bin during the final iteration of the Wang-Landau algorithm [216, 217]. The average reaction probability for each bin, $P_i(E)$, is calculated from these parameters according to equation (2.111). Only the SCTST-W method was employed in this chapter. The CRP in this framework is given as follows:

$$N(E) = \sum_{i=1}^{(E-E_\mathrm{ZPE})/\Delta E} \rho(E_i) P_i(E) \Delta E. \tag{4.26}$$

4.2.6 Rate Constants

FD and 1-D rate constants were calculated as described in sections 2.5 and 2.7. For FD calculations, anharmonic partition functions were calculated for the vibrational DOFs of the reactants as described in the previous section. Both C_2H_6 and the TS of reaction (1.2) have a normal mode that corresponds to torsional motion about the

C−C bond. These torsional modes have low frequencies, so truncating the Taylor expansion of the PES along these modes at fourth order can be problematic. Consequently, these modes were not considered vibrational DOFs and therefore not included in anharmonic constant calculations or anharmonic partition functions. Instead, they were treated using hindered rotor partition functions in FD and 1-D calculations using the "single-frequency" approximation presented in ref [228].

With this approximation, the partition function is chosen such that as T decreases, it tends to the partition function for a harmonic oscillator, and as T increases, it tends to the partition function for a free rotor, interpolating smoothly between these two regimes [228]. This partition function, $Q_{\mathrm{HR}}(T)$, is given as follows:

$$Q_{\mathrm{HR}}(T) = Q_{\mathrm{HO}}(T) \tanh\left[Q_{\mathrm{FR}}(T)/Q_{\mathrm{I}}(T)\right], \tag{4.27}$$

where $Q_{\mathrm{HO}}(T)$ is a standard partition function for a harmonic oscillator with frequency ω, and $Q_{\mathrm{I}}(T)$ is defined as follows:

$$Q_{\mathrm{I}}(T) = \frac{k_{\mathrm{B}}T}{\hbar\omega}. \tag{4.28}$$

$Q_{\mathrm{FR}}(T)$ is a standard rigid rotor partition function:

$$Q_{\mathrm{FR}}(T) = \frac{(2\pi I k_{\mathrm{B}}T)^{1/2}}{\hbar\sigma}. \tag{4.29}$$

The moment of inertia I is calculated with respect to rotation around the C−C bond, and a symmetry number σ of 3 is used. Thus, the formulas used to calculate rate constants for reaction (1.2) have an additional partition function in the numerator and denominator.

4.3 Results

4.3.1 Vibrational Frequencies

Vibrational frequencies for the stationary points of reaction (1.1) are presented in Table 4.2. Higher orders of Richardson extrapolation were applied to calculate Hessian

Table 4.2: MP2/cc-pVTZ harmonic frequencies of the stationary points of reaction (1.1), obtained with different orders of Richardson extrapolation applied to the calculation of Hessian matrix elements.

	CH_4		TS			CH_3	H_2
	$2^{nd,a}$	0^{th}	4^{th}	2^{nd}	0^{th}	0^{th}	0^{th}
	3211.83	3211.86	1642.93i	1643.02i	1644.09i	3368.94	4526.52
	3211.79	3211.76	3291.55	3291.51	3290.98	3368.73	
	3211.79	3211.70	3290.09	3290.08	3289.88	3178.37	
	3076.09	3076.05	3133.46	3133.37	3132.10	1446.04	
	1586.14	1586.14	1948.13	1948.02	1946.41	1446.00	
	1586.13	1586.10	1473.15	1472.92	1468.93	486.593	
	1349.61	1349.61	1469.65	1469.47	1466.57		
	1349.57	1349.59	1151.75	1151.46	1146.80		
	1349.57	1349.56	1148.09	1147.85	1144.02		
			1090.13	1089.93	1086.67		
			591.965	591.292	580.398		
			576.733	576.268	568.752		
ZPE[b]	28.495	28.495	27.397	27.394	27.336	19.006	6.471

[a]The order of Richardson extrapolation applied. For all orders, the smallest step size used was 0.01 a_0.

[b]Harmonic zero-point energy in kcal mol^{-1}.

Table 4.3: MP2/cc-pVTZ harmonic frequencies of the stationary points of reaction (1.2) used in rate constant calculations.

	Frequencies (cm^{-1})						ZPE[a]
C_2H_6[b]	3176.48	3176.40	3154.37	3154.29	3082.40	3080.94	47.484
	1522.88	1522.84	1522.65	1522.56	1430.90	1410.76	
	1229.57	1229.56	1029.26	827.033	826.344	316.378	
TS[c]	1644.08i	3254.62	3168.86	3156.37	3150.23	3082.05	46.669
	1867.81	1528.38	1524.86	1506.54	1409.28	1279.77	
	1212.80	1204.12	1148.88	1064.20	912.838	887.457	
	617.580	350.584	318.029				
C_2H_5[b]	3337.15	3223.29	3181.13	3127.42	3045.94	1536.31	38.345
	1521.32	1507.27	1409.52	1225.58	1099.32	1013.28	
	810.847	490.931	293.700				

[a]Harmonic zero-point energy in kcal mol^{-1}.
[b]Calculated without Richardson extrapolation.
[c]Calculated using second-order Richardson extrapolation.

elements and frequencies of CH_4 and the transition state (TS). Step sizes of 0.01, 0.02, and 0.04 a_0 were used for CH_4, and step sizes from 0.01 to 0.16 a_0 were used for the TS. All zeroth order calculations were performed at 0.01 a_0. For CH_4, second-order frequencies differ from their zeroth-order counterparts by at most 0.09 cm^{-1}. Larger differences between second- and zeroth-order frequencies are observed for the TS, particularly for lower-frequency modes. The difference for the lowest-frequency mode of the TS is 7.516 cm^{-1}. Fourth-order frequencies for the TS are significantly closer to second-order frequencies than to zeroth-order frequencies, indicating that Hessian elements converge as the order of extrapolation is increased. All frequencies exhibited agreement with those calculated previously by Banks *et al.* [150] at the same level of theory. The zeroth-order frequencies of the products, CH_3 and H_2 are also reported in Table 4.2. These are used only to calculate the reaction's vibrationally adiabatic reverse barrier height, ΔV_r. SCTST calculations are generally significantly less sensitive to the reverse barrier height than to the forward barrier height, so only zeroth-order frequencies were calculated for the products.

The vibrational frequencies used in rate constant calculations for reaction (1.2) are presented in Table 4.3. Only second-order Richardson extrapolation was applied to the TS, as higher orders of extrapolation were not found to significantly change the frequencies for the TS of reaction (1.1). The TS frequencies of reaction (1.2) differ significantly from those reported in ref [145] but less significantly from those from a later study [154]. In general, greater differences are observed at lower frequencies. The difference between the lowest frequency calculated in this chapter and that from ref [154] is 119 cm^{-1}. This is likely due to the tighter geometry optimization condition used to calculate the TS geometry in this chapter and not to the application of Richardson extrapolation. Zeroth-order frequencies were more similar to second-order frequencies than to those from ref [154].

4.3.2 Full-Dimensional SCTST Calculations

4.3.2.1 $H + CH_4 \longrightarrow H_2 + CH_3$ (reaction (1.1))

The anharmonic constants of the TS required for full-dimensional (FD) rate constant calculations on reaction (1.1) were calculated at three different levels of accuracy. At the highest level of accuracy, fourth-order Richardson extrapolation was applied to calculate elements of the TS Hessian. A fourth-order calculation requires five numerical Hessian matrices, each calculated using a different step size. Calculations were then performed at four displacements along each of the normal mode eigenvectors, $\Delta q = \pm 0.8$ and $\Delta q = \pm 1.6$. Previous studies that used analytical Hessians to calculate anharmonic constants have used smaller displacements along normal mode eigenvectors [116, 122, 123, 209]. However, it was found that some of the functions relating the Hessian matrix elements to the displacement Δq exhibited erratic behaviour at displacements less than 0.8.

At each of the $4F$ displaced geometries, 3 Hessian matrices were calculated numer-

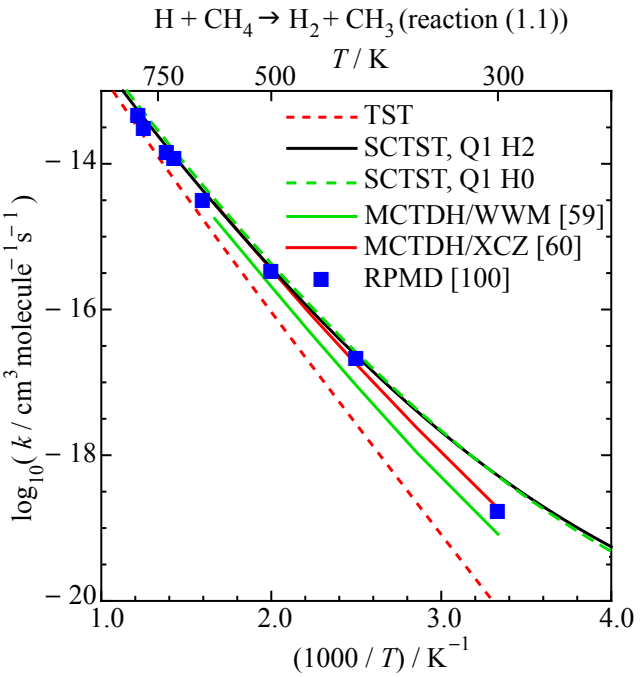


Figure 4.3: Rate constants for reaction (1.1) calculated using two different sets of anharmonic constants ("Q1 H0," black curve, and "Q1 H0," dashed green curve), as defined in the text, presented in comparison with results from two previous MCTDH calculations on the WWM [59] and XCZ [60] PESs (red and green curves, respectively) and one RPMD study [100] (blue squares). Results from Transition State Theory (TST) are presented for comparison (dashed red curve).

ically in order to apply second-order Richardson extrapolation to the Hessian matrix elements. $0.01a_0$ was the smallest step size used in these calculations. First-order Richardson extrapolation was then applied using these converged Hessian elements at both Δq displacements to calculate third and fourth potential derivatives. This calculation will be denoted "Q1 H2," since Hessian elements at each of the displaced geometries were calculated at second order and derivatives along the normal mode coordinates Q were calculated at first order. This is computationally the most expensive method applied in this chapter, requiring 149 Hessian matrix calculations at the TS. At this level of accuracy, increasing the size of the system requires 36 additional Hessian matrix calculations per additional atom.

The rate constants calculated using this set of anharmonic constants are pre-

Table 4.4: Rate constants for reaction (1.1), in units cm^3 $molecule^{-1}$ s^{-1}, calculated by TST and SCTST[a]

T(K)	TST	SCTST, Q1 H2	SCTST, Q1 H0	1-D SCTST, Hessians	1-D SCTST, energies
200	1.30(−25)	5.33(−21)	3.94(−21)	4.56(−22)	3.96(−22)
250	1.15(−22)	5.54(−20)	4.78(−20)	1.22(−20)	1.13(−20)
300	1.08(−20)	5.23(−19)	5.12(−19)	2.22(−19)	2.14(−19)
350	2.81(−19)	4.01(−18)	4.24(−18)	2.45(−18)	2.41(−18)
400	3.31(−18)	2.33(−17)	2.58(−17)	1.73(−17)	1.72(−17)
450	2.30(−17)	1.04(−16)	1.18(−16)	8.55(−17)	8.56(−17)
500	1.10(−16)	3.70(−16)	4.27(−16)	3.24(−16)	3.25(−16)
600	1.20(−15)	2.78(−15)	3.26(−15)	2.61(−15)	2.63(−15)
700	6.93(−15)	1.28(−14)	1.52(−14)	1.25(−14)	1.26(−14)
800	2.67(−14)	4.25(−14)	5.03(−14)	4.27(−14)	4.31(−14)
1000	1.89(−13)	2.49(−13)	2.94(−13)	2.61(−13)	2.63(−13)
	Number of *ab initio* Hessian calculations required				
CH_4	1	19	19	1	1
TS	1	149	53	17	5

[a]Numbers in parentheses denote powers of 10.

sented in Figure 4.3 and Table 4.4. Rate constants calculated previously using the Multi-Configurational Time-Dependent Hartree (MCTDH) method on two different potential energy surfaces [59, 60] and using RPMD on another PES [100] are also presented in Figure 4.3 for comparison. Results from SCTST are somewhat greater than those from other studies, differing from RPMD results by a factor of 3.08 and from MCDTH results by factors of 2.75 and 6.23 at 300 K, but this level of agreement is comparable to that among results from the other studies.

In order to evaluate the extent to which Richardson extrapolation affects rate constants calculated using SCTST, another calculation was performed without Richardson extrapolation. Hessians were calculated at displacements of $\Delta q = \pm 0.8$ along different eigenvectors than in the "Q1 H2" calculation, as the Hessian calculated at the TS without Richardson extrapolation differs from the fourth-order Hessian. It was impossible to calculate a density of states for the bound vibrational modes of the TS using the resulting set of anharmonic constants because the first derivatives

of the energy in the bound modes $E_{\{n\}'}$ with respect to each of the $F-1$ quantum numbers were all negative at the zero-point configuration. As these derivatives are required to be non-negative for all "bound" configurations (section 2.4), the fact that the zero-point configuration was not bound implies that the anharmonic constants used in this calculation were not realistic. Rate constants therefore could not be calculated for this case.

As discussed previously, the number of Hessian matrix calculations required to perform a calculation at the "Q1 H2" level of accuracy increases significantly with system size. Furthermore, the cost of each individual numerical Hessian matrix calculation increases with system size. It is therefore desirable to find a method at an intermediate level of accuracy that scales more favourably but yields accurate results, as determined by agreement with results from the "Q1 H2" calculation. Further calculations were therefore performed, and it was found that results from a "Q1 H0" calculation with the same step sizes exhibited the best agreement. This treatment only differs from the "Q1 H2" scheme in that only one numerical Hessian matrix calculation was performed at each displaced geometry. Rate constants calculated with this set of TS anharmonic constants can be found in Fig. 4.3 and Table 4.4. These results differ from the "Q1 H2" results by 14% at 250 K.

The number of *ab initio* Hessian matrix calculations required for each of the rate constant calculations discussed in this section are listed in Table 4.4 in order to give a sense of their relative computational costs. Numerical Hessian matrices calculated at different step sizes and used to calculate higher-order matrix elements by Richardson extrapolation are considered separate Hessian calculations. The "Q1 H0" calculation requires 36% of the Hessian calculations required for the "Q1 H2" calculation, and yet the resulting rate constants are comparable in accuracy. This reduction in the number of Hessian calculations required may yield substantial efficiency gains for

larger systems with more DOFs.

4.3.2.2 $\mathbf{H + C_2H_6 \longrightarrow H_2 + C_2H_5}$ (reaction (1.2))

Rate constants for reaction (1.2) calculated at the "Q1 H0" level of accuracy are presented in Figure 4.4 and Table 4.5. In these calculations, the DOFs corresponding to internal rotation about the C−C bond (torsional modes) in both the TS and C_2H_6 were not included in anharmonic constant calculations and were instead treated using hindered rotor partition functions. These results exhibit reasonable agreement with those from a previous 2-D QRS calculation by von Horsten *et al.* [154], differing by 16% at 250 K. Results from the earlier 2-D QRS calculation [145] considered in Chapter 3 exhibit better agreement at higher temperatures but are 14.1 times less than the "Q0 H1" SCTST rate constants at 260 K. Results from two experimental studies [201, 202], as well as from conventional TST, are included for comparison. In TST calculations, torsional modes were treated as in SCTST calculations.

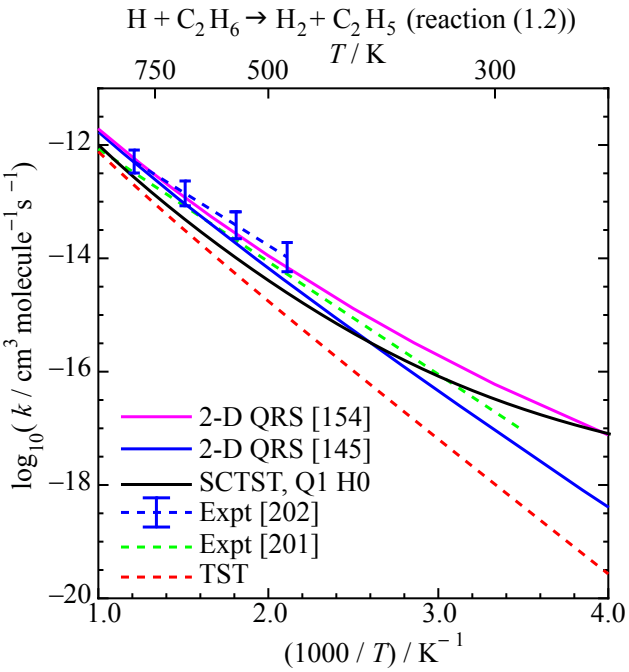


Figure 4.4: Rate constants for reaction (1.2) calculated at the "Q1 H0" level of accuracy described in the text (black curve) shown in comparison with results from previous 2-D QRS studies [145, 154] (magenta and blue curves), and other experimental studies [201, 202] (dashed green and blue curves). Rate constants calculated using TST are included as well (red dashed curve).

Table 4.5: Rate constants for reaction (1.2), in units cm^3 $molecule^{-1}$ s^{-1}, calculated using the methods discussed in this study.[a]

T(K)	TST	SCTST, Q1 H0	1-D SCTST (Hessians)	1-D SCTST (energies)
200	8.36(−23)	2.20(−18)	7.34(−19)	1.84(−19)
250	2.09(−20)	8.29(−18)	3.89(−18)	2.08(−18)
300	8.47(−19)	3.35(−17)	2.14(−17)	1.86(−17)
350	1.22(−17)	1.34(−16)	1.04(−16)	1.16(−16)
400	9.16(−17)	4.84(−16)	4.18(−16)	5.18(−16)
450	4.48(−16)	1.52(−15)	1.37(−15)	1.78(−15)
500	1.62(−15)	4.13(−15)	3.78(−15)	5.02(−15)
600	1.16(−14)	2.13(−14)	1.94(−14)	2.57(−14)
700	4.93(−14)	7.63(−14)	6.77(−14)	8.87(−14)
800	1.51(−13)	2.13(−13)	1.83(−13)	2.35(−13)
1000	7.70(−13)	1.01(−12)	8.11(−13)	1.01(−12)
	Number of *ab initio* Hessian calculations required			
C_2H_6	1	35	1	1
TS	1	83	7	3

[a]Numbers in parentheses denote powers of 10.

Table 4.6: Statistics of the rate constant of reaction (1.1) at 250 K associated with multiple executions of the Wang-Landau algorithm to calculate the density of states of the TS[a]

N_{iter}	N_{trial}	Mean	Standard Deviation	Range
22	10^7	5.491(−20)	3.93(−22)	1.53(−21)
22	10^6	5.469(−20)	1.21(−21)	4.16(−21)
21	10^7	5.495(−20)	4.03(−22)	1.20(−21)

[a]Numbers in parentheses denote powers of 10. The Wang-Landau algorithm was executed 10 times for each configuration of the parameters N_{iter} and N_{trial}.

4.3.2.3 Sensitivity to Wang-Landau Parameters

There is some degree of error associated with the choice of parameters N_{iter} and N_{trial} in the Wang-Landau algorithm used to calculate the CRP for FD calculations. The impact of this error on the calculated density of states has been calculated and discussed previously [126]. Here, further tests that provide insight into the impact of this error on rate constants calculated using SCTST are discussed.

The Wang-Landau algorithm was executed multiple times with the anharmonic constants from the "Q1 H2" calculation to calculate the rate constant at 250 K for reaction (1.1). Results from this analysis are presented in Table 4.6. The first line in this table presents results from executing the algorithm 10 times with the values of N_{iter} and N_{trial} given in section 4.2.5. Subsequent lines present results obtained by changing the value of one of these parameters and executing the algorithm 10 more times.

When N_{iter} and N_{trial} are assigned the values given in section 4.2.5, the range of the results from the 10 executions is 2.8% of the mean of these results, and the standard deviation is 0.72%. This level of uncertainty is significantly less than the difference between the SCTST and TST rate constants (factor of 229 at 250 K). Decreasing the N_{trial} parameter by one order of magnitude increased the standard

deviation and range somewhat, by factors of 3.1 and 2.7, respectively, and decreasing N_{iter} affected them negligibly. This suggests that that the chosen values of N_{iter} and N_{trial} are sufficient for the purposes of this study. The value of the N_{trial} parameter used for the calculations in this chapter is an order of magnitude greater than the greatest value suggested in ref [126], and the N_{iter} parameter is 1 greater.

4.3.3 One-Dimensional SCTST Calculations

A 1-D SCTST calculation depends only on the third and fourth derivatives of the PES along the reaction mode, which are used to calculate the anharmonic constant for the reaction mode, x_{FF}. 1-D SCTST calculations were performed using the same derivatives that were used in the "Q1 H2" and "Q1 H0" FD calculations for reactions (1.1) and (1.2), respectively. The resulting rate constants are labeled as "1-D SCTST, Hessians" in Figure 4.5 and Tables 4.4 and 4.5, as they were calculated by differentiating Hessian matrix elements. For both reactions (1.1) and (1.2), results from 1-D calculations agree favourably with those from FD calculations. This 1-D method underestimates rate constants by factors of 4.54 and 2.14 at 250 K, respectively.

These discrepancies can be understood by considering the potential barriers associated with each of these calculations, which are presented in Figures 4.5(b) and 4.5(d). Only the potential barriers corresponding to the ground-state configuration of $\{n\}'$ are shown for the FD calculations. The ground-state configuration is the only configuration sampled in the lowest-energy bin of the density of states (equation (4.26)), as is required in the Wang-Landau algorithm [126]. This configuration contributes most significantly to calculated rate constants due to the presence of a Boltzmann factor in equation (2.104).

The FD barriers for reactions (1.1) and (1.2) are narrower than the respective 1-D barriers, which gives rise to greater reaction probabilities at low energies in FD

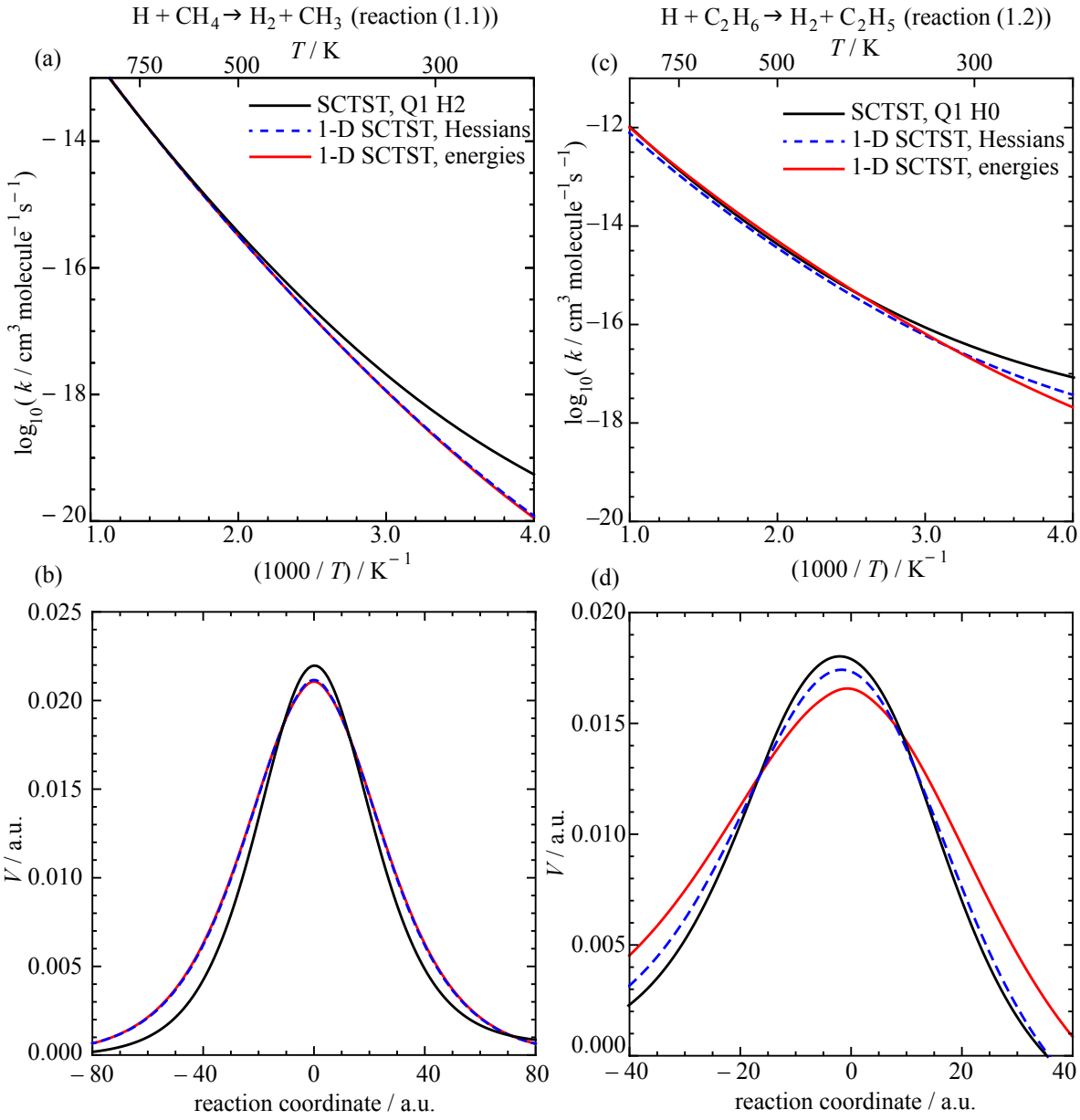


Figure 4.5: (a) Rate constants for reaction (1.1) calculated using FD and 1-D SCTST. The results labeled "1-D SCTST, Hessians" were calculated using anharmonic constants obtained from Hessian matrices at displaced geometries (dashed blue curve). Those labeled "1-D SCTST, energies" were calculated using single-point energy calculations along the reaction mode (red curve). (b) The corresponding vibrationally adiabatic potential barriers used to calculate these rate constants. The FD barrier is presented for the case in which the quantum numbers of all bound modes are 0. (c) and (d) The same results for reaction (1.2).

calculations, and therefore greater rate constants, relative to the "1-D, Hessians" calculations. The width of each barrier is determined by the effective reaction mode frequency Ω and reaction mode anharmonic constant x_{FF} used to construct it. Both of these parameters incorporate coupling between the reaction mode and bound modes through cross-derivatives of the PES. Therefore, this coupling can be thought to narrow the FD barrier relative to the 1-D barrier. Differences in the heights of these barriers arise from differences between the harmonic and anharmonic ZPEs of the reactants and TS.

Performing a 1-D calculation in this way requires two numerical Hessian matrix calculations at displaced geometries. The number of single-point energy calculations required for these calculations generally increases with system size. In principle, however, only four single-point energy calculations along the reaction mode are required to calculate the third and fourth PES derivatives required for a 1-D SCTST calculation, in addition to one at the TS. An additional calculation was performed in this way, using single-point energies calculated at the MP2/cc-pVTZ level of theory with a step size of 0.02 $\mathrm{Da}^{1/2}a_0$, which was found to yield the best agreement with FD rate constants. Second-order Richardson extrapolation was found not to significantly change these results. Rate constants calculated from the resulting anharmonic constants are presented in Figure 4.5 and Tables 4.4 and 4.5 and labeled as "1-D SCTST, energies." These results exhibited a high level of agreement with the "1-D SCTST, Hessians" results, which is reflected in the similarity of the corresponding potential barriers (Figures 4.5(b) and 4.5(d)).

In the case of reaction (1.1), calculating the FD "Q1 H2" rate constants required 144 Hessian matrices at displaced geometries, which in total required 33,504 single-point energy calculations, more than 8000 times more than the 4 required for the "1-D SCTST, energies" calculation. For reaction (1.2), the number of calculations

required for the FD and 1-D methods beyond those required for a conventional TST calculation differed by a factor of approximately 10,000.

4.4 Conclusions

This chapter presents an evaluation the accuracy and efficiency of 1-D SCTST in relation to those of FD SCTST for the $H + CH_4$ and $H + C_2H_6$ reactions. A practical procedure for numerically calculating the third and fourth derivatives of the PES was presented, and a method (Richardson extrapolation) for systematically improving the accuracy of these derivatives was presented and applied. Third and fourth derivatives along only the reaction mode are required for 1-D SCTST calculations, so these were also obtained by differentiating single-point energies. The Wang-Landau algorithm was discussed as an efficient method for approximating the density of states for the vibrational modes of the TS, which is used to calculate the CRP for FD calculations.

FD SCTST rate constants calculated for both reactions agreed well with results from previous theoretical and experimental studies. FD calculations for the $H + CH_4$ reaction were performed at three different levels of accuracy, according to the order of Richardson extrapolation applied to different derivatives. Calculations at the lowest level of accuracy, which involved the least computational expense, failed because the anharmonic constants calculated by this method were determined not to be physically realistic. Calculations at an intermediate level of accuracy agreed reasonably well with those at the highest level of accuracy but required 64% fewer Hessian matrix calculations. Rate constant calculations for the $H + C_2H_6$ reaction were therefore performed at this intermediate level of accuracy. These results suggest the applicability of Richardson extrapolation to SCTST calculations as an alternative to existing methods that depend upon analytical derivatives.

For both reactions, the two 1-D SCTST methods yielded rate constants in acceptable agreement with each other and with FD rate constants. The 1-D method that used single-point energy calculations was significantly more efficient than the FD methods implemented in this chapter, as it requires at minimum only 4 single-point energy calculations in addition to those required for a conventional TST calculation. If necessary, this approach can be systematically improved by Richardson extrapolation. The low computational expense of this 1-D method suggests its applicability as a method for approximating the rate constants for systems significantly larger than those that could previously be treated by quantum scattering approaches.

Chapter 5

Conclusions

The first-principles calculation of chemical reaction rate constants is a discipline of contemporary interest and importance. This thesis focuses on one method for calculating rate constants, Semiclassical Transition State Theory (SCTST). SCTST offers potential gains in computational efficiency over existing exact and approximate theories because it does not require a complete PES. In SCTST, the energy of the transition state (TS) is expressed in terms of "good" quantum numbers, and an expression for the cumulative reaction probability (CRP) is derived from this energy expression. In this thesis, second-order vibrational perturbation theory (VPT2) is used to derive the energy expression, although it is possible to employ other approaches as well [170]. Deep tunnelling corrections [125] are presented as a means of correcting physically unrealistic behaviour of the reactant and product asymptotes. Finally, a novel reduced-dimensionality (RD) approach to SCTST, analogous to previous RD approaches to QRS calculations, is presented as a method for achieving further gains in computational efficiency over full-dimensional (FD) SCTST.

Chapter 3 discusses the application of SCTST to reduced-dimensionality potential energy surfaces (PESs) on which accurate quantum reactive scattering (QRS) calculations have been performed previously. Because QRS methods explicitly account for quantum mechanical effects on reaction rate constants, comparing their results to

those from SCTST calculations enables a rigorous test of the accuracy with which SCTST recovers these effects. SCTST calculations on these 2-D PESs yielded results in generally good agreement with 2-D QRS calculations.

One-dimensional calculations are also performed on these 2-D PESs. In these calculations, tunnelling only along the reaction mode is treated within the SCTST framework. When deep tunnelling corrections were applied, results from the 1-D method did not differ significantly from 2-D results for all reactions. The fact that a 1-D calculation can yield results that agree closely with those from a calculation of higher dimensionality suggests its potential applicability as a method for approximating FD rate constants.

Constructing the PESs considered in Chapter 3 involved performing high-level *ab initio* calculations at multiple geometries in between the reactant and product channels, which involves significant computational expense. Calculating rate constants by SCTST from these PESs does not fully leverage one of the primary advantages of the theory, namely that it depends on the shape of the PES only near the TS. Furthermore, these PESs were constructed by fitting an analytical function, which can introduce errors. An alternative method for performing SCTST calculations using *ab initio* calculations instead of an analytical PES is presented in Chapter 4.

The MP2/cc-pVTZ level of theory was found to be sufficient for calculating the frequencies and anharmonic constants required for SCTST calculations, provided that Richardson extrapolation is applied to improve the accuracy of numerical derivatives. FD calculations on the H + CH_4 and H + C_2H_6 reactions yielded results in good agreement with previous theoretical and experimental studies. Furthermore, reducing the dimensionality of both of these calculations to 1-D, considering only the reaction mode, yielded results that agreed closely with those from FD calculations. Finally, an implementation of 1-D SCTST that requires only 4 single-point energy calculations in

addition to those required for an accurate TST calculation is presented. This method is significantly more computationally efficient than the implementation of FD SCTST discussed in this thesis but nevertheless yields results in reasonable agreement with those from FD SCTST.

These findings suggest that the RD SCTST approach to rate constant calculations can potentially be applied to reactions for which existing rate constant theories are computationally intractable. Furthermore, it can be systematically improved by applying Richardson extrapolation to frequency and anharmonic constant calculations. Future work should involve evaluating the accuracy of this method for a wider variety of reactions.

Appendix A

Definitions of Abbreviations

PES	Potential energy surface
QRS	Quantum reactive scattering
RD	Reduced-dimensionality
RPMD	Ring polymer molecular dynamics
SCT	Small-curvature tunnelling
SCTST	Semiclassical Transition State Theory
SCTST-M	SCTST as originally formulated
SCTST-W	SCTST with deep tunnelling corrections
TD	Time-dependent
TI	Time-independent
TS	Transition state
TST	Transition State Theory
VPT2	Second-order vibrational perturbation theory
VTST	Variational Transition State Theory
WKB	Wentzel-Kramers-Brillouin (Theory)
ZPE	Zero-point energy

CC	Coupled cluster
cc-pVTZ	Correlation consistent polarised valence triple-zeta Dunning (basis set)
aug-cc-pVTZ	cc-pVTZ basis set augmented with diffuse orbitals
CCSD(T)	Coupled Cluster Singles and Doubles with perturbative treatment of Triples
CCSD(T)-F12a	Explicitly correlated CCSD(T) method
CRP	Cumulative reaction probability
DOF	Degree of freedom
FD	Full-dimensional
HF	Hartree-Fock
LAG4	Least-action ground-state tunnelling, version 4
LCG4	Large-curvature ground-state tunnelling, version 4
MCTDH	Multiconfigurational Time-Dependent Hartree
MEP	Minimum-energy path
μOMT	Microcanonically optimised multidimensional tunnelling
MP2	Second-order Møller-Plesset Perturbation Theory
MT	Multidimensional tunnelling

References

[1] Levine, R. D. and Bernstein, R. B. *Molecular Reaction Dynamics and Chemical Reactivity.* Oxford University Press, New York, **1987**.

[2] Miller, W. H. *Annu. Rev. Phys. Chem.* 41, **1990**, 245–281.

[3] Nyman, G. and Yu, H.-G. *Rep. Prog. Phys.* 63, **2000**, 1001–1059.

[4] Althorpe, S. C. and Clary, D. C. *Annu. Rev. Phys. Chem.* 54, **2003**, 493–529.

[5] Prather, M. and Jaffe, A. H. *J. Geophys. Res.: Atmos.* 95, **1990**, 3473–3492.

[6] Douglass, A. R.; Schoeberl, M. R.; Stolarski, R. S.; Waters, J. W.; Russell, J. M.; Roche, A. E.; and Massie, S. T. *J. Geophys. Res.: Atmos.* 100, **1995**, 13967–13978.

[7] Michelsen, H. A.; Webster, C. R.; Manney, G. L.; Scott, D. C.; Margitan, J. J.; May, R. D.; Irion, F. W.; Gunson, M. R.; Russell, J. M.; and Spivakovsky, C. M. *J. Geophys. Res.: Atmos.* 104, **1999**, 26419–26436.

[8] Santee, M. L.; Froidevaux, L.; Manney, G. L.; Read, W. G.; Waters, J. W.; Chipperfield, M. P.; Roche, A. E.; Kumer, J. B.; Mergenthaler, J. L.; and Russell, J. M. *J. Geophys. Res.* 101, **1996**, 18835–18859.

[9] Arnold, P. A. and Carpenter, B. K. *Chem. Phys. Lett.* 328, **2000**, 90–96.

[10] Gao, J. and Truhlar, D. G. *Annu. Rev. Phys. Chem.* 53, **2002**, 467–505.

[11] Navarro Yerga, R. M.; Álvarez Galván, M. C.; del Valle, F.; Villoria de la Mano, J.; and Fierro, J. L. G. *ChemSusChem* 2, **2009**, 471–485.

[12] Leenheer, A. J. and Atwater, H. A. *J. Electrochem. Soc.* 157, **2010**, B1290–B1294.

[13] Hisatomi, T.; Kubota, J.; and Domen, K. *Chem. Soc. Rev.* 43, **2014**, 7520–7535.

[14] Clary, D. C. and Kroes, G.-J. In Sabatier, P. and Pike, R., eds., *Scattering: Scattering and Inverse Scattering in Pure and Applied Science*, Academic Press, London, **2001**, chap. 2.6.4, pp. 1068–1080.

[15] Born, M. and Oppenheimer, R. *Annalen der Physik* 389, **1927**, 457–484.

[16] Bowman, J. M.; Braams, B. J.; Carter, S.; Chen, C.; Czakó, G.; Fu, B.; Huang, X.; Kamarchik, E.; Sharma, A. R.; Shepler, B. C.; Wang, Y.; and Xie, Z. *J. Phys. Chem. Lett.* 1, **2010**, 1866–1874.

[17] Bowman, J. M.; Czako, G.; and Fu, B. *Phys. Chem. Chem. Phys.* 13, **2011**, 8094–8111.

[18] Koch, W. and Zhang, D. H. *J. Chem. Phys.* 141, **2014**, 021101.

[19] Conte, R.; Houston, P. L.; and Bowman, J. M. *J. Chem. Phys.* 140, **2014**, 151101.

[20] Espinosa-Garcia, J.; Monge-Palacios, M.; and Corchado, J. C. *Adv. Phys. Chem.* 2012, **2012**, 164752.

[21] Schlegel, H. B. *J. Comput. Chem.* 24, **2003**, 1514–1527.

[22] Corchado, J. C.; Bravo, J. L.; and Espinosa-Garcia, J. *J. Chem. Phys.* 130, 184314.

[23] Bowman, J. M. *J. Phys. Chem.* 95, **1991**, 4960–4968.

[24] Bowman, J. M. *Theor. Chem. Acc.* 108, **2002**, 125–133.

[25] Xu, X.; Chen, J.; and Zhang, D. H. *Chin. J. Chem. Phys.* 27, **2014**, 373–379.

[26] Li, J.; Chen, J.; Zhao, Z.; Xie, D.; Zhang, D. H.; and Guo, H. *J. Chem. Phys.* 142, **2015**, 204302.

[27] Welsch, R. and Manthe, U. *J. Chem. Phys.* 138, **2013**, 164118.

[28] Balakrishnan, N.; Kalyanaraman, C.; and Sathyamurthy, N. *Phys. Rep.* 280, **1997**, 79–144.

[29] Tal-Ezer, H. and Kosloff, R. *J. Chem. Phys.* 81, **1984**, 3967–3971.

[30] Feit, M. D. and Fleck, J. A. *J. Chem. Phys.* 80, **1984**, 2578–2584.

[31] Mowrey, R. C. and Kouri, D. J. *J. Chem. Phys.* 84, **1986**, 6466–6473.

[32] Neuhauser, D. and Baer, M. *J. Chem. Phys.* 91, **1989**, 4651–4657.

[33] Neuhauser, D.; Baer, M.; Judson, R. S.; and Kouri, D. J. *Comput. Phys. Commun.* 63, **1991**, 460–481.

[34] Jackson, B. *Annu. Rev. Phys. Chem.* 46, **1995**, 251–274.

[35] Lara, M.; Aguado, A.; Paniagua, M.; and Roncero, O. *J. Chem. Phys.* 113, **2000**, 1781–1794.

[36] Hu, W. and Schatz, G. C. *J. Chem. Phys.* 125, **2006**, 132301.

[37] Vissers, G. W. M. and McCoy, A. B. *J. Phys. Chem. A* 110, **2006**, 5978–5981.

[38] Gómez-Carrasco, S. and Roncero, O. *J. Chem. Phys.* 125, 054102.

[39] Monks, P. D. D.; Connor, J. N. L.; and Althorpe, S. C. *J. Phys. Chem. A* 110, **2006**, 741–748.

[40] Lasorne, B.; Robb, M. A.; and Worth, G. A. *Phys. Chem. Chem. Phys.* 9, **2007**, 3210–3227.

[41] Zanchet, A.; Roncero, O.; González-Lezana, T.; Rodríguez-López, A.; Aguado, A.; Sanz-Sanz, C.; and Gómez-Carrasco, S. *J. Phys. Chem. A* 113, **2009**, 14488–14501.

[42] Frankcombe, T. J.; Collins, M. A.; and Worth, G. A. *Chem. Phys. Lett.* 489, **2010**, 242–247.

[43] Koch, W. and Frankcombe, T. J. *Phys. Rev. Lett.* 110, **2013**, 263202.

[44] Meyer, H.-D.; Manthe, U.; and Cederbaum, L. S. *Chem. Phys. Lett.* 165, **1990**, 73–78.

[45] Beck, M.; Jäckle, A.; Worth, G.; and Meyer, H.-D. *Phys. Rep.* 324, **2000**, 1–105.

[46] Worth, G. A.; Meyer, H.-D.; Köppel, H.; Cederbaum, L. S.; and Burghardt, I. *Int. Rev. Phys. Chem.* 27, **2008**, 569–606.

[47] Meyer, H.-D.; Gatti, F.; and Worth, G., eds. *Multidimensional Quantum Dynamics: MCTDH Theory and Applications*. John Wiley & Sons, Weinheim, **2009**.

[48] Manthe, U. *J. Chem. Phys.* 142, **2015**, 244109.

[49] Jäckle, A.; Heitz, M.-C.; and Meyer, H.-D. *J. Chem. Phys.* 110, **1999**, 241–248.

[50] Huarte-Larrañaga, F. and Manthe, U. *J. Chem. Phys.* 113, **2000**, 5115–5118.

[51] Huarte-Larrañaga, F. and Manthe, U. *J. Phys. Chem. A* 105, **2001**, 2522–2529.

[52] Wu, T.; Werner, H.-J.; and Manthe, U. *Science* 306, **2004**, 2227–2229.

[53] Wu, T.; Werner, H.-J.; and Manthe, U. *J. Chem. Phys.* 124, **2006**, 164307.

[54] Nyman, G.; van Harrevelt, R.; and Manthe, U. *J. Phys. Chem. A* 111, **2007**, 10331–10337.

[55] Schiffel, G. and Manthe, U. *J. Chem. Phys.* 132, **2010**, 084103.

[56] van Harrevelt, R.; Nyman, G.; and Manthe, U. *J. Chem. Phys.* 126, **2007**, 084303.

[57] Welsch, R. and Manthe, U. *J. Chem. Phys.* 141, **2014**, 174313.

[58] Welsch, R. and Manthe, U. *J. Chem. Phys.* 141, **2014**, 051102.

[59] Welsch, R. and Manthe, U. *J. Chem. Phys.* 137, **2012**, 244106.

[60] Welsch, R. and Manthe, U. *J. Chem. Phys.* 142, **2015**, 064309.

[61] Kuppermann, A. *Chem. Phys. Lett.* 32, **1975**, 374–375.

[62] Walker, R. B. and Light, J. C. *Annu. Rev. Phys. Chem.* 31, **1980**, 401–433.

[63] Clary, D. C. *Science* 279, **1998**, 1879–1882.

[64] Brooks, A. N. and Clary, D. C. *J. Chem. Phys.* 92, **1990**, 4178–4190.

[65] Eyring, H. *J. Chem. Phys.* 3, **1935**, 107–115.

[66] Evans, M. G. and Polanyi, M. *Trans. Faraday Soc.* 31, **1935**, 875–894.

[67] Wynne-Jones, W. F. K. and Eyring, H. *J. Chem. Phys.* 3, **1935**, 492–502.

[68] Eyring, H. *Trans. Faraday Soc.* 34, **1938**, 41–48.

[69] Evans, M. G. *Trans. Faraday Soc.* 34, **1938**, 49–57.

[70] Wigner, E. *Trans. Faraday Soc.* 34, **1938**, 29–41.

[71] Miller, W. H. *Faraday Discuss.* 110, **1998**, 1–21.

[72] Garrett, B. C. and Truhlar, D. G. *J. Phys. Chem.* 83, **1979**, 1079–1112.

[73] Truhlar, D. G.; Isaacson, A. D.; Skodje, R. T.; and Garrett, B. C. *J. Phys. Chem.* 86, **1982**, 2252–2261.

[74] Truhlar, D. G.; Isaacson, A. D.; and Garrett, B. C. In Baer, M., ed., *Theory of Chemical Reaction Dynamics*, CRC Press, Boca Raton, **1985**, vol. IV, chap. 2, pp. 65–137.

[75] Garrett, B. C. and Truhlar, D. G. In Dykstra, C. E.; Frenking, G.; Kim, K. S.; and Scuseria, G. E., eds., *Theory and Applications of Computational Chemistry: The First Forty Years*, Elsevier, Amsterdam, **2005**, chap. 5, pp. 67–87.

[76] Fernandez-Ramos, A.; Ellingson, B. A.; Garrett, B. C.; and Truhlar, D. G. In Lipkowitz, K. B. and Cundari, T. R., eds., *Reviews in Computational Chemistry*, John Wiley & Sons, Inc., Hoboken, **2007**, vol. 23, chap. 3, pp. 125–232.

[77] Griffiths, D. J. *Introduction to Quantum Mechanics*. Pearson Education, Inc., Upper Saddle River, **2005**, 2 edn.

[78] Skodje, R. T.; Truhlar, D. G.; and Garrett, B. C. *J. Phys. Chem.* 85, **1981**, 3019–3023.

[79] Bowman, J. L. and Wagner, A. F. In Clary, D. C., ed., *The Theory of Chemical Reaction Dynamics*, Springer, New York, **1986**, vol. 170 of *NATO Advanced Science Institute Series C*, pp. 47–76.

[80] Amaee, B.; Connor, J. N. L.; Whitehead, J. C.; Jakubetz, W.; and Schatz, G. C. *Faraday Discuss. Chem. Soc.* 84, **1987**, 387–403.

[81] Benderskii, V.; Makarov, D.; and Wight, C. *Chemical Dynamics at Low Temperatures*, vol. 88 of *Advances in Chemical Physics*. Wiley, New York, **1994**.

[82] Mezey, P. G. In Heidrich, D., ed., *The Reaction Path in Chemistry: Current Approaches and Perspectives*, Springer Science and Business Media, Dordrecht, **1995**, pp. 11–38.

[83] Fernández-Ramos, A.; Miller, J. A.; ; Klippenstein, S. J.; and Truhlar, D. G. *Chem. Rev.* 106, **2006**, 4518–4584.

[84] Fernández-Ramos, A. and Truhlar, D. G. *J. Chem. Phys.* 114, **2001**, 1491–1496.

[85] Arseneau, D. J.; Fleming, D. G.; Li, Y.; Li, J.; Suleimanov, Y. V.; and Guo, H. *J. Phys. Chem. B* 120, **2016**, 1641–1648.

[86] Suleimanov, Y. V. and Espinosa-Garcia, J. *J. Phys. Chem. B* 120, **2016**, 1418–1428.

[87] Ng, M.; Mok, D. K.; Lee, E. P.; and Dyke, J. M. *Mol. Phys.* 113, **2015**, 1511–1533.

[88] Gong, S.; Luo, Q.; and Wei, G. M. *J. Phys. Chem. A* 119, **2015**, 4746–4754.

[89] Gonzalez-Lavado, E.; Corchado, J. C.; Suleimanov, Y. V.; Green, W. H.; and Espinosa-Garcia, J. *J. Phys. Chem. A* 118, **2014**, 3243–3252.

[90] Meana-Pañeda, R.; Truhlar, D. G.; and Fernández-Ramos, A. *J. Chem. Theory Comput.* 6, **2010**, 3015–3025.

[91] Meana-Pañeda, R.; Truhlar, D. G.; and Fernández-Ramos, A. *J. Chem. Theory Comput.* 6, **2010**, 6–17.

[92] Espinosa-García, J. *Phys. Chem. Chem. Phys.* 10, **2008**, 1277–1284.

[93] Albu, T. V.; Corchado, J. C.; and Truhlar, D. G. *J. Phys. Chem. A* 105, **2001**, 8465–8487.

[94] Allison, T. C. and Truhlar, D. G. In Thompson, D. L., ed., *Modern Methods for Multidimensional Dynamics Computations in Chemistry*, World Scientific, Singapore, **1998**, pp. 618–712.

[95] Bondi, D. K.; Connor, J. N. L.; Garrett, B. C.; and Truhlar, D. G. *J. Chem. Phys.* 78, **1983**, 5981–5989.

[96] Garrett, B. C.; Truhlar, D. G.; Wagner, A. F.; and Dunning, T. H. *J. Chem. Phys.* 78, **1983**, 4400–4413.

[97] Pu, J. and Truhlar, D. G. *J. Chem. Phys.* 116, **2002**, 1468–1478.

[98] Craig, I. R. and Manolopoulos, D. E. *J. Chem. Phys.* 122, **2005**, 084106.

[99] Craig, I. R. and Manolopoulos, D. E. *J. Chem. Phys.* 123, **2005**, 034102.

[100] Meng, Q.; Chen, J.; and Zhang, D. H. *J. Chem. Phys.* 143, **2015**, 101102.

[101] Suleimanov, Y. V.; Collepardo-Guevara, R.; and Manolopoulos, D. E. *J. Chem. Phys.* 134, **2011**, 044131.

[102] Jang, S. and Voth, G. A. *J. Chem. Phys.* 112, **2000**, 8747–8757.

[103] Geva, E.; Shi, Q.; and Voth, G. A. *J. Chem. Phys.* 115, **2001**, 9209–9222.

[104] Navrotskaya, I.; Shi, Q.; and Geva, E. *Isr. J. Chem.* 42, **2002**, 225–236.

[105] Voth, G. A.; Chandler, D.; and Miller, W. H. *J. Chem. Phys.* 91, **1989**, 7749–7760.

[106] Zhang, Y.; Rommel, J. B.; Cvitas, M. T.; and Althorpe, S. C. *Phys. Chem. Chem. Phys.* 16, **2014**, 24292–24300.

[107] Hele, T. J. H. and Althorpe, S. C. *J. Chem. Phys.* 138, **2013**, 084108.

[108] Althorpe, S. C. and Hele, T. J. H. *J. Chem. Phys.* 139, **2013**, 084115.

[109] Smedarchina, Z.; Siebrand, W.; and Fernández-Ramos, A. *J. Chem. Phys.* 127, **2007**, 174513.

[110] Rommel, J. B.; Goumans, T. P. M.; and Kästner, J. *J. Chem. Theory Comput.* 7, **2011**, 690–698.

[111] Althorpe, S. C. *J. Chem. Phys.* 134, **2011**, 114104.

[112] Miller, W. H. *J. Chem. Phys.* 62, **1975**, 1899.

[113] Miller, W. H. *Faraday Discuss. Chem. Soc.* 62, **1977**, 40–46.

[114] Miller, W. H.; Hernandez, R.; Handy, N. C.; Jayatilaka, D.; and Willetts, A. *Chem. Phys. Lett.* 172, **1990**, 62–68.

[115] Mills, I. M. In Mathews, C. W. and Rao, K. N., eds., *Molecular Spectroscopy: Modern Research*, Academic Press, New York, **1972**, chapter 3.2, pp. 115–140.

[116] Barone, V. *J. Chem. Phys.* 122, **2005**, 14108.

[117] Burcl, R.; Handy, N. C.; and Carter, S. *Spectrochim. Acta, Part A* 59, **2003**, 1881–1893.

[118] Neugebauer, J. and Hess, B. A. *J. Chem. Phys.* 118, **2003**, 7215–7225.

[119] Schneider, W. and Thiel, W. *Chem. Phys. Lett.* 157, **1989**, 367–373.

[120] Cohen, M. J.; Handy, N. C.; Hernandez, R.; and Miller, W. H. *Chem. Phys. Lett.* 192, **1992**, 407–416.

[121] Cohen, M. J.; Willetts, A.; and Handy, N. C. *Chem. Phys. Lett.* 223, **1994**, 459–464.

[122] Nguyen, T. L.; Stanton, J. F.; and Barker, J. R. *J. Phys. Chem. A* 115, **2011**, 5118–5126.

[123] Barker, J. R.; Nguyen, T. L.; and Stanton, J. F. *J. Phys. Chem. A* 116, **2012**, 6408–6419.

[124] Weston, R. E., Jr.; Nguyen, T. L.; Stanton, J. F.; and Barker, J. R. *J. Phys. Chem. A* 117, **2013**, 821–835.

[125] Wagner, A. F. *J. Phys. Chem. A* 117, **2013**, 13089–13100.

[126] Nguyen, T. L. and Barker, J. R. *J. Phys. Chem. A* 114, **2010**, 3718–3730.

[127] Bowman, J. M. In Prigogine, I. and Rice, S. A., eds., *Advances in Chemical Physics*, John Wiley & Sons, Inc., Hoboken, **1985**, vol. 61, pp. 115–167.

[128] Clary, D. C. *J. Phys. Chem.* 98, **1994**, 10678–10688.

[129] Bowman, J. M. and Schatz, G. C. *Annu. Rev. Phys. Chem.* 46, **1995**, 169–196.

[130] Aguillon, F. and Sizun, M. *J. Chem. Phys.* 112, **2000**, 10179–10191.

[131] Szichman, H.; Gilibert, M.; González, M.; Giménez, X.; and Navarro, A. A. *J. Chem. Phys.* 113, **2000**, 176–183.

[132] Szichman, H.; Gilibert, M.; González, M.; Giménez, X.; and Aguilar, A. *J. Chem. Phys.* 114, **2001**, 9882–9894.

[133] Nyman, G. and Clary, D. C. *J. Chem. Phys.* 101, **1994**, 5756–5771.

[134] Manthe, U.; Seideman, T.; and Miller, W. H. *J. Chem. Phys.* 101, **1994**, 4759–4768.

[135] Nyman, G.; Clary, D. C.; and Levine, R. D. *Chem. Phys.* 191, **1995**, 223–233.

[136] Nyman, G. *Chem. Phys. Lett.* 240, **1995**, 571–577.

[137] Nyman, G. *J. Chem. Phys.* 104, **1996**, 6154–6167.

[138] Takayanagi, T. *J. Chem. Phys.* 104, **1996**, 2237–2242.

[139] Clary, D. C. and Palma, J. *J. Chem. Phys.* 106, **1997**, 575–583.

[140] Le Garrec, J.-L.; Rowe, B. R.; Queffelec, J. L.; Mitchell, J. B. A.; and Clary, D. C. *J. Chem. Phys.* 107, **1997**, 1021–1024.

[141] Kerkeni, B. and Clary, D. C. *J. Chem. Phys.* 123, **2005**, 64305.

[142] Takayanagi, T. *Chem. Phys.* 312, **2005**, 61–67.

[143] Espinosa-García, J.; Nyman, G.; and Corchado, J. C. *J. Chem. Phys.* 130, 184315.

[144] Kerkeni, B. and Clary, D. C. *Mol. Phys.* 103, **2005**, 1745–1755.

[145] Kerkeni, B. and Clary, D. C. *J. Chem. Phys.* 121, **2004**, 6809–6821.

[146] Kerkeni, B. and Clary, D. C. *J. Chem. Phys.* 120, **2004**, 2308–2318.

[147] Kerkeni, B. and Clary, D. C. *Phys. Chem. Chem. Phys.* 8, **2006**, 917–925.

[148] Kerkeni, B. and Clary, D. C. *Chem. Phys. Lett.* 438, **2007**, 1–7.

[149] Banks, S. T. and Clary, D. C. *Phys. Chem. Chem. Phys.* 9, **2007**, 933–943.

[150] Banks, S. T.; Tautermann, C. S.; Remmert, S. M.; and Clary, D. C. *J. Chem. Phys.* 131, **2009**, 044111.

[151] Banks, S. T. and Clary, D. C. *J. Chem. Phys.* 130, **2009**, 024106.

[152] Remmert, S. M.; Banks, S. T.; and Clary, D. C. *J. Phys. Chem. A* 113, **2009**, 4255–4264.

[153] Remmert, S. M.; Banks, S. T.; Harvey, J. N.; Orr-Ewing, A. J.; and Clary, D. C. *J. Chem. Phys.* 134, **2011**, 204311.

[154] von Horsten, H. F.; Banks, S. T.; and Clary, D. C. *J. Chem. Phys.* 135, **2011**, 094311.

[155] Shan, X. and Clary, D. C. *Phys. Chem. Chem. Phys.* 15, **2013**, 18530–18538.

[156] Shan, X.; Remmert, S. M.; Clary, D. C.; Zhang, B.; and Liu, K. *Chem. Phys. Lett.* 587, **2013**, 88–92.

[157] Shan, X. and Clary, D. C. *Phys. Chem. Chem. Phys.* 15, **2013**, 1222–1231.

[158] Shan, X. and Clary, D. C. *J. Phys. Chem. A* 118, **2014**, 10134–10143.

[159] Walker, R. B. and Hayes, E. F. In Clary, D. C., ed., *The Theory of Chemical Reaction Dynamics*, Springer Netherlands, **1986**, vol. 170 of *NATO ASI Series*, pp. 105–133.

[160] Palma, J.; Echave, J.; and Clary, D. C. *J. Phys. Chem. A* 106, **2002**, 8256–8260.

[161] Wang, D. *J. Chem. Phys.* 117, **2002**, 9806–9810.

[162] Kungwan, N. and Truong, T. N. *J. Phys. Chem. A* 109, **2005**, 7742–7750.

[163] Marshall, R. M.; Purnell, H.; and Sheppard, A. *J. Chem. Soc., Faraday Trans. 2* 82, **1986**, 929–935.

[164] Greene, S. M.; Shan, X.; and Clary, D. C. *J. Phys. Chem. A* 119, **2015**, 12015–12027.

[165] Greene, S. M.; Shan, X.; and Clary, D. C. *J. Chem. Phys.* 144, **2016**, 084113.

[166] Greene, S. M.; Shan, X.; and Clary, D. C. *J. Chem. Phys.* in press.

[167] Miller, W. H. *J. Chem. Phys.* 61, **1974**, 1823–1834.

[168] Miller, W. H. *J. Chem. Phys.* 55, **1971**, 3146–3149.

[169] Bhattacharya, R. and Basu, I. *Comput. Phys. Commun.* 16, **1979**, 167–173.

[170] Hernandez, R. and Miller, W. H. *Chem. Phys. Lett.* 214, **1993**, 129–136.

[171] Frisch, M. J. *et al.*. Gaussian 03 Revision C.02. Gaussian, Inc., Wallingford, **2003**.

[172] Werner, H.-J. *et al.*. MOLPRO, a package of *ab initio* programs, version 2010.2.

[173] Ochterski, J. W. Vibrational analysis in Gaussian, **1999**. `http://www.gaussian.com/g_whitepap/vib.htm`.

[174] McQuarrie, D. A. *Quantum Chemistry*. University Science Books, Sausalito, **2008**.

[175] Gray, D. and Robiette, A. *Mol. Phys.* 37, **1979**, 1901–1920.

[176] Wang, X.-G.; Sibert, E. L.; and Martin, J. M. L. *J. Chem. Phys.* 112, **2000**, 1353–1366.

[177] Matthews, D. A. and Stanton, J. F. *Mol. Phys.* 107, **2009**, 213–222.

[178] Clabo, D. A.; Allen, W. D.; Remington, R. B.; Yamaguchi, Y.; and Schaefer, H. F. *Chem. Phys.* 123, **1988**, 187–239.

[179] Mills, I. and Robiette, A. *Mol. Phys.* 56, **1985**, 743–765.

[180] Amos, R. D.; Handy, N. C.; Green, W. H.; Jayatilaka, D.; Willetts, A.; and Palmieri, P. *J. Chem. Phys.* 95, **1991**, 8323–8336.

[181] Martin, J. M. L.; Lee, T. J.; Taylor, P. R.; and François, J.-P. *J. Chem. Phys.* 103, **1995**, 2589–2602.

[182] Handy, N. C. and Willetts, A. *Spectrochim. Acta, Part A* 53, **1997**, 1169–1177.

[183] Greiner, W. *Classical Mechanics: Systems of Particles and Hamiltonian Dynamics*. Classical Theoretical Physics, Springer, New York, **2003**.

[184] Seideman, T. and Miller, W. H. *J. Chem. Phys.* 96, **1992**, 4412–4422.

[185] Miller, W. H. *Acc. Chem. Res.* 26, **1993**, 174–181.

[186] Ahmed, Z. *Phys. Lett. A* 157, **1991**, 1–5.

[187] Szabo, A. and Ostlund, N. S. *Modern Quantum Chemistry: Introduction to Advanced Electronic Structure Theory*. Dover Publications, Inc., Mineola, **1996**.

[188] Jensen, F. *Introduction to Computational Chemistry*. John Wiley & Sons, Chichester, **1999**.

[189] Raghavachari, K.; Trucks, G. W.; Pople, J. A.; and Head-Gordon, M. *Chem. Phys. Lett.* 157, **1989**, 479–483.

[190] Dunning, T. H. *J. Chem. Phys.* 90, **1989**, 1007–1023.

[191] Adler, T. B.; Knizia, G.; and Werner, H.-J. *J. Chem. Phys.* 127, **2007**, 221106.

[192] Knizia, G.; Adler, T. B.; and Werner, H.-J. *J. Chem. Phys.* 130, **2009**, 054104.

[193] Peterson, K. A.; Adler, T. B.; and Werner, H.-J. *J. Chem. Phys.* 128, **2008**, 084102.

[194] Jackels, C. F.; Gu, Z.; and Truhlar, D. G. *J. Chem. Phys.* 102, **1995**, 3188–3201.

[195] Lu, D.-h. and Truhlar, D. G. *J. Chem. Phys.* 99, **1993**, 2723–2738.

[196] Wolfram Research, Inc., "Mathematica," Version 8.0, Champaign, (2010).

[197] Stechel, E. B.; Walker, R. B.; and Light, J. C. *J. Chem. Phys.* 69, **1978**, 3518.

[198] Bowman, J. M. In Laganà, A. and Riganelli, A., eds., *Reaction and Molecular Dynamics*, Springer, New York, **2000**, vol. 75 of *Lecture Notes in Chemistry*, pp. 101–114.

[199] Álvarez Barcia, S.; Flores, J. R.; and Kästner, J. *J. Phys. Chem. A* 118, **2014**, 78–82.

[200] Sutherland, J. W.; Su, M. C.; and Michael, J. V. *Int. J. Chem. Kinet.* 33, **2001**, 669–684.

[201] Lede, J. and Villermaux, J. *Can. J. Chem.* 56, **1978**, 392–401.

[202] Bryukov, M. G.; Slagle, I. R.; and Knyazev, V. D. *J. Phys. Chem. A* 105, **2001**, 6900–6909.

[203] Marshall, R. M.; Purnell, H.; and Satchell, P. W. *J. Chem. Soc., Faraday Trans. 1* 80, **1984**, 2395–2403.

[204] Kerr, J. and Parsonage, J. *Evaluated kinetic data on gas phase hydrogen transfer reactions of methyl radicals*. Butterworths, London, **1976**.

[205] Arthur, N. L. and Bell, T. N. *Rev. Chem. Intermed.* 2, **1978**, 37–74.

[206] East, A. L. L.; Allen, W. D.; and Klippenstein, S. J. *J. Chem. Phys.* 102, **1995**, 8506–8532.

[207] Shao, Y. *et al.*. *Mol. Phys.* 113, **2015**, 184–215.

[208] Guest, M. F.; Bush, I. J.; Dam, H. J. J. V.; Sherwood, P.; Thomas, J. M. H.; Lenthe, J. H. V.; Havenith, R. W. A.; and Kendrick, J. *Mol. Phys.* 103, **2005**, 719–747.

[209] Stanton, J. F. *et al.*. CFOUR, Coupled-Cluster techniques for Computational Chemistry, a quantum-chemical program package, **2009**.

[210] Rendell, A. P. and Lee, T. J. *J. Chem. Phys.* 94, **1991**, 6219–6228.

[211] Scheiner, A. C.; Scuseria, G. E.; Rice, J. E.; Lee, T. J.; and Schaefer, H. F. *J. Chem. Phys.* 87, **1987**, 5361–5373.

[212] Simandiras, E.; Handy, N.; and Amos, R. *Chem. Phys. Lett.* 133, **1987**, 324–330.

[213] Ridders, C. *Adv. Eng. Software* 4, **1982**, 75–76.

[214] Schlegel, H. B. In Lawley, K., ed., *Ab Initio Methods in Quantum Chemistry I*, John Wiley & Sons, Chichester, **2009**, vol. 67 of *Advances in Chemical Physics*, pp. 249–286.

[215] Pulay, P. *WIREs Comput Mol Sci* 4, **2014**, 169–181.

[216] Barker, J. R. *Int. J. Chem. Kinet.* 33, **2001**, 232–245.

[217] Barker, J. R.; Ortiz, N. F.; Preses, J. M.; Lohr, L. L.; Maranzana, A.; Stimac, P. J.; Nguyen, T. L.; and Kumar, T. J. D. Multiwell-2014.1 software, **2014**. `http://aoss.engin.umich.edu/multiwell/`.

[218] Kendall, R. A.; Dunning, T. H.; and Harrison, R. J. *J. Chem. Phys.* 96, **1992**, 6796–6806.

[219] Richardson, L. F. and Gaunt, J. A. *Phil. Trans. R. Soc. Lond. A* 226, **1927**, 299–361.

[220] Press, W. H.; Teukolsky, S. A.; Vetterling, W. T.; and Flannery, B. P. *Numerical Recipes in C: The Art of Scientific Computing*. Cambridge University Press, Cambridge, **1992**, 2 edn.

[221] Green, W. H.; Jayatilaka, D.; Willetts, A.; Amos, R. D.; and Handy, N. C. *J. Chem. Phys.* 93, **1990**, 4965–4981.

[222] Hoy, A.; Mills, I.; and Strey, G. *Mol. Phys.* 24, **1972**, 1265–1290.

[223] Khairutdinov, R.; Zamaraev, K. I.; and Zhadanov, V. P. In Compton, R. G., ed., *Electron Tunneling in Chemistry*, Elsevier, Amsterdam, **1989**, vol. 30 of *Comprehensive Chemical Kinetics*, pp. 69–110.

[224] Wollrab, J. E. *Rotational Spectra and Molecular Structure*. Physical Chemistry: a Series of Monographs, Academic Press, Inc., New York, **1967**.

[225] Wang, F. and Landau, D. P. *Phys. Rev. Lett.* 86, **2001**, 2050–2053.

[226] Wang, F. and Landau, D. P. *Phys. Rev. E* 64, **2001**, 056101.

[227] Basire, M.; Parneix, P.; and Calvo, F. *J. Chem. Phys.* 129, **2008**, 081101.

[228] Chuang, Y.-Y. and Truhlar, D. G. *J. Chem. Phys.* 112, **2000**, 1221–1228.